EIC **C**omprehensive **C**hromodynamics **E**xperiment
Collaboration Detector Proposal

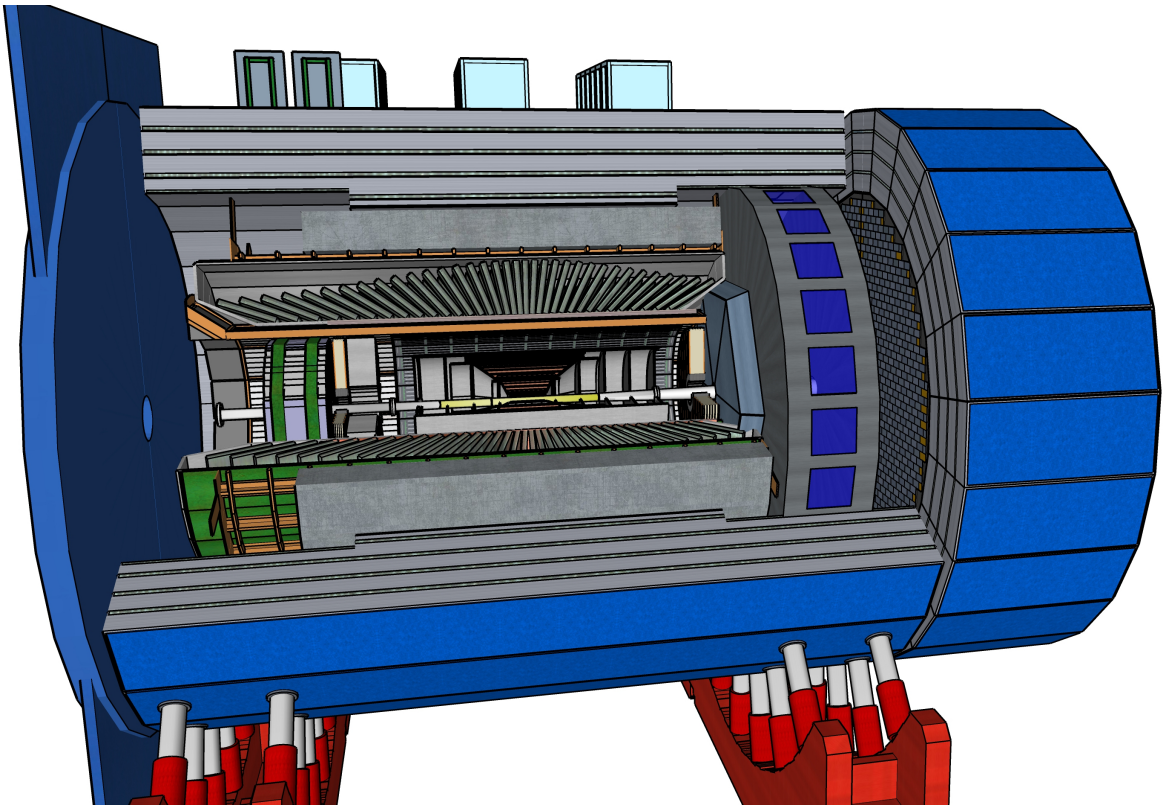

A state of the art detector capable of fully exploiting the science potential of the EIC, realized through the reuse of select instrumentation and infrastructure, to be ready by project CD-4A

December 1, 2021

Executive Summary

THE Electron-Ion Collider (EIC) is an extraordinary new facility enabling frontier research in nuclear physics, with initial operation planned for July 2031. It is the largest single project ever undertaken by the US DOE Office of Nuclear Physics and, as such, represents a landmark allocation of resources. To provide the required machine capabilities within the projected funding, the EIC project has developed a comprehensive plan that strategically repurposes select elements of the existing Relativistic Heavy-Ion Collider (RHIC) complex at Brookhaven National Laboratory (BNL).

Realizing the physics of the EIC also requires an extremely capable detector that is integrated with the machine to a very high degree. The complex set of requirements that an EIC detector needs to meet in order to deliver on the physics promise of the EIC has been extensively detailed in the EIC User Group's Yellow Report [1]. At the same time, how best to design a complete detector fulfilling those requirements has been a question in front of the world-wide nuclear physics community for some years.

The EIC Comprehensive Chromodynamics Experiment (ECCE) detector concept described in this proposal provides a compelling answer to this question. The ECCE proposal is a *Detector 1 Collaboration Proposal*, and the detector capabilities address the full EIC science mission as described in the EIC community White Paper [2] and 2018 National Academies of Science (NAS) Report [3]. The design is simultaneously fully capable, low-risk, and cost-effective by employing state-of-the art technologies and leveraging substantial ($58M) contributions from reuse and non-DOE sources. The estimated direct cost of the proposed detector to DOE is $162M in 2021 USD. If approved for construction in 2023, the detector will be ready for operations in 2031.

The scale of the complex and extensive instrumentation needed to realize a fully capable EIC detector can easily lead to a design that is incompatible with the funding and schedule guidance that has been provided by the EIC project. However, like the EIC itself, ECCE strategically repurposes select components of existing experimental equipment to maximize its capabilities within the envelope of planned resources. Notably, the central barrel of the detector incorporates the storied 1.4 T BaBar superconducting solenoid and the sPHENIX barrel hadronic calorimeter currently under construction. This strategic reuse of equipment enables attention and resources to be focused on other aspects of the detector that optimize its physics yield, while managing cost and risk.

To achieve maximum performance, the BaBar solenoid will be instrumented with an AI-optimized high-precision tracking system that, combined with superb electromagnetic calorimetry, produces high-precision particle momentum measurements. These core detection systems are supplemented with a set of Čerenkov and TOF particle identification systems and a new longitudinally segmented hadronic calorimeter to form the complete ECCE central detector. We further present a set of far-forward spectrometers for low-Q^2 measurements and luminosity monitoring, and an optimized far-forward detection system with a zero-degree calorimeter and a set of spectrometers to enable an extensive set of tagged and diffractive reaction measurements.

The ECCE detector concept is the product of the ECCE consortium, formed in 2020 and comprising 96 institutions from around the world. Since release of the call for proposals, the scientists of the ECCE consortium have worked to develop a cost-effective, low-risk detector that fully addresses the EIC science program and can be built and commissioned by the 2031 EIC project CD-4A milestone.

In Chapter 1 we present a general introduction to EIC science. Chapter 2 presents the components of the ECCE detector including its overall layout, selected technology for each component and its rationale, and characteristic performance evaluated using complete ECCE GEANT4 simulations. It details the proposed detector electronics and readout scheme, the computing plan for data taking and processing, and possible detector upgrade paths. Chapter 3 presents simulation studies of selected physical processes that show

quantitatively how ECCE addresses the EIC scientific program. Chapter 4 presents the ECCE consortium behind the proposal and discusses a plan for a transition into a full collaboration following the completion of proposal review. Chapter 5 discusses the ECCE project including cost estimates, detector R&D needs, in-kind/reuse contributions and project schedule for successful detector commissioning by the EIC CD-4A project milestone.

This proposal cannot detail the full scope of the studies conducted by the consortium. It focuses instead on key information highlighting the important characteristics and advantages of the ECCE detector design and implementation approach, and then it provides references to relevant ECCE technical notes for further details as appropriate. The complete list of these technical notes is given in Table 1.

An important measure of the strength of the ECCE consortium is its ability to produce this proposal that completely documents the case for ECCE in a manner fully compliant with the requirements outlined in the call for proposals. Accordingly, all of the technical notes and supplementary material provided in Table 1 represents the status as of December 1, 2021. The work of the consortium of course continues, and we look forward to providing any relevant updates in our forthcoming presentations.

Table 1: ECCE supplementary notes. All notes are linked from the clickable names in this table and can also be found online at: https://www.ecce-eic.org/ecce-internal-notes (password: ECCEprop).

Detector	**Physics**
BaBar solenoid	Jet reconstruction
Calorimetry	Diffractive & tagged reactions
Tracking	Exclusive reactions
Particle identification	Open heavy flavor nuclear modification
DAQ & electronics	DIS & SIDIS kinematic resolution
Far-forward/backward	Single hadron transverse single spin asymmetry
Schedule, cost, & risk	Unpolarized TMDs
Computing plan	Nuclear matter modification of jet yields
Software tools	Inclusive reactions
Simulation framework	Breit Frame jet reconstruction using Centauro Algorithm
	Longitudinal double-spin asymmetry in SIDIS
	XYZ spectroscopy
	Dihadron azimuthal correlations
	Electroweak & BSM
	Quarkonia

Contents

Chapter 1: Introduction

The physics program at the Electron-Ion Collider (EIC) – planned for construction at Brookhaven National Laboratory (BNL), in close partnership with the Thomas Jefferson National Accelerator Facility (TJNAF) – will be the culmination of decades of research into the quark and gluon substructure of hadrons and nuclei, and provide scientific opportunities well into the next three decades. The EIC will address a broad set of questions, described in a 2018 report by the National Academies of Science (NAS) [3]:

- While the longitudinal momenta of quarks and gluons in nucleons and nuclei have been measured with great precision at previous facilities – most notably CEBAF at JLab and the HERA collider at DESY – the full three-dimensional momentum and spatial structure of even a proton has yet to be fully elucidated, particularly including spin, which requires the separation of the intrinsic spin of the constituent particles from their orbital motion.
- These studies will also provide insight into how the mutual interactions of quarks and gluons generate the nucleon mass and the masses of other hadrons. The nucleon mass is one of the single most important scales in all of physics, as it is the basis for nuclear masses, and thus the mass of essentially all of visible matter.
- The density of quarks and gluons which carry the smallest x, the fraction of the nuclear momentum (or that of its constituent nucleons), can grow so large that their mutual interactions enter a non-linear regime in which elegant, universal features emerge in what may be a new, distinct state of matter characterized by a "saturation momentum scale". Probing this state requires high energy beams and large nuclear size (A), and will answer longstanding questions raised by the heavy ion programs at RHIC and the LHC.

To carry out this ambitious physics program, the EIC requires a comprehensive experimental program carefully designed to extract all of the physics from the scattering of electrons off of hadrons and nuclei. An ideal EIC detector must measure nearly every particle emerging from the interaction point, including its direction, its momentum, as well as its identity. Each of these aspects of the EIC physics program, and how a single comprehensive detector system could address them, was studied by the EIC scientific community and led to the community-authored "Yellow Report" [1]. The report also identified a set of detector performance requirements that flow down from the physics requirements of the EIC science program articulated in the NAS report:

- The outgoing electron must be distinguished from other produced particles in the event, with a pion rejection of 10^3 — 10^4 even at large angles, in order to characterize the kinematic properties of the initial scattering process. These include the momentum fraction of the struck target constituent (x) and the squared momentum transfer (Q^2).
- A large-acceptance magnetic spectrometer is needed to measure the scattered electron momentum, as well as those of the other charged hadrons and leptons. The magnet dimensions and field strength should be matched to the scientific program and the medium-energy scale of the EIC. This requires a nearly 4π angular aperture, and the ability to make precisely measurements of the sagitta of its curved trajectory, to measure its momentum down to low-p_t, and its point of origin, to distinguish particles from charm and bottom hadron decays.
- A high-purity hadron particle identification (PID) system, able to provide continuous (e/π) and (K/π) discrimination out to the highest momentum (60 GeV), is important for identifying particles containing different light quark flavors.
- A hermetic electromagnetic calorimeter system, with matching hadronic sections, is required to measure neutral particles (particularly photons and neutrons) and, in tandem with the spectrometer, to

reconstruct hadronic jets which carry kinematic information about the struck quark or gluon, as well as its radiative properties via its substructure.

- Far-forward detector systems, in the direction of incoming hadron, are needed in order to perform measurements of deeply-virtual Compton scattering and diffractive processes, e.g. by measuring the small deflections of the incoming proton and suppress incoherent interactions with nuclei.
- Far-backward detectors in the direction of the incoming electron are needed to reach the very lowest values of Q^2, and to measure luminosity for both absolute cross-section extractions as well as precision spin dependent asymmetries.

As a response to the joint BNL/JLab call for detector proposals, this document presents the EIC Comprehensive QCD Experiment (ECCE), which has been designed, simulated and extensively studied by the 96 institutes in the newly-formed ECCE proto-collaboration. The ECCE detector has been designed to address the full scope of the EIC physics program as presented in the EIC white paper [2] and the NAS report. The specific requirements that each of the ECCE detector systems has to meet flow down, in turn, from the more general detector requirements described in the Yellow Report. Through judicious use of select articles of existing equipment, ECCE can be built within the budget envelope set out by the EIC project while simultaneously managing cost and schedule risks.

The ECCE concept reuses the BaBar superconducting solenoid as well as the sPHENIX barrel flux return and hadronic calorimeter. These two pieces of equipment are currently being installed in RHIC Interaction Region 8 (IR8) as part of the sPHENIX detector. Engineering studies have confirmed that these two components can be relocated to IR6, the IR where the EIC project currently plans to site the on-project detector. At the same time, should the EIC project change its plans, ECCE can be installed in IR8.

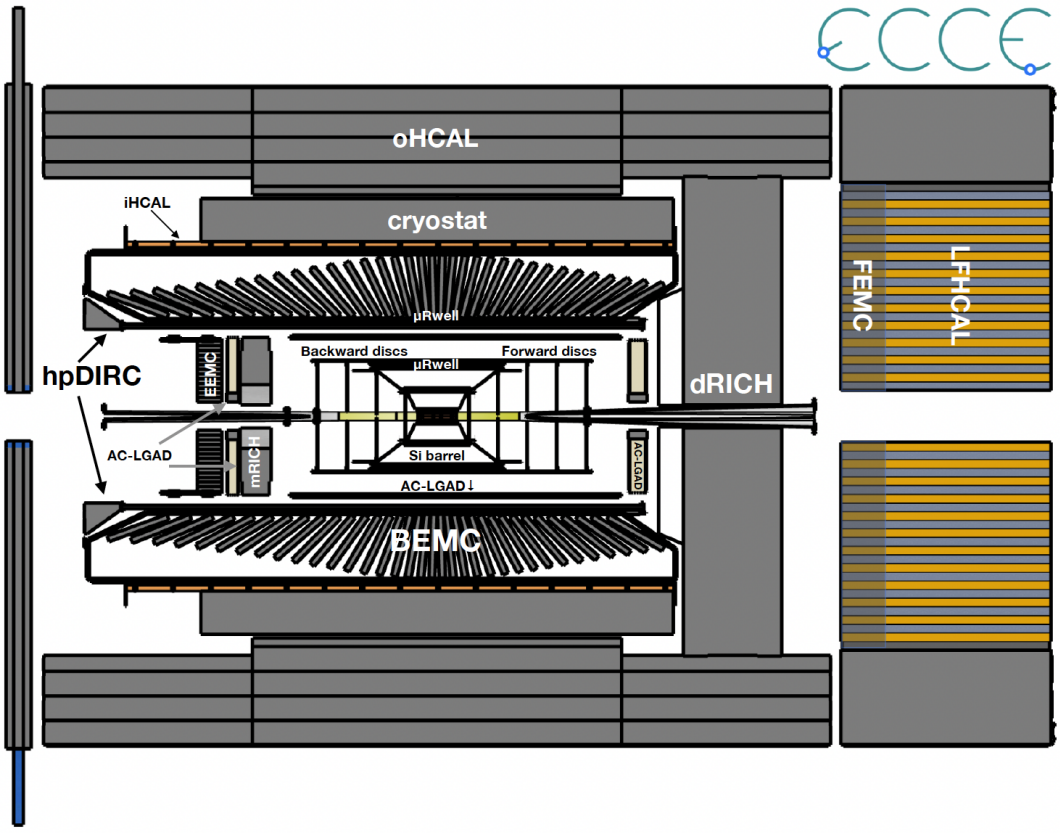

Figure 1.1: Side view of the full ECCE detector system, oriented with the hadron beam arriving from the left and the electron beam arriving from the right.

Chapter 2: The ECCE Detector

This chapter presents a description of the ECCE detector, including the central detector (barrel, forward electron endcap and backward hadron endcap), and the far-forward and far-backward systems. A high-level description is provided in the first section, to highlight the integrated design. Detailed descriptions of each ECCE region are then found in the following sections.

2.1 ECCE detector overview

The ECCE detector consists of three major components: the central detector, the far-forward system, and the far-backward region. The ECCE central detector has a cylindrical geometry based on the BaBar/sPHENIX superconducting solenoid, and has three primary subdivisions: the barrel, the forward endcap, and the backward endcap (Fig. 2.1). Henceforth "forward" is defined as the hadron/nuclear beam direction and backwards the electron beam direction. We will use electron or backward, and hadron or forward interchangeably when describing the endcaps.

Table 2.1 lists the physics requirements in the ECCE central detector, the technical challenges associated with its realization, and the ECCE solutions that achieves the stated goals. Comments about future upgrade paths

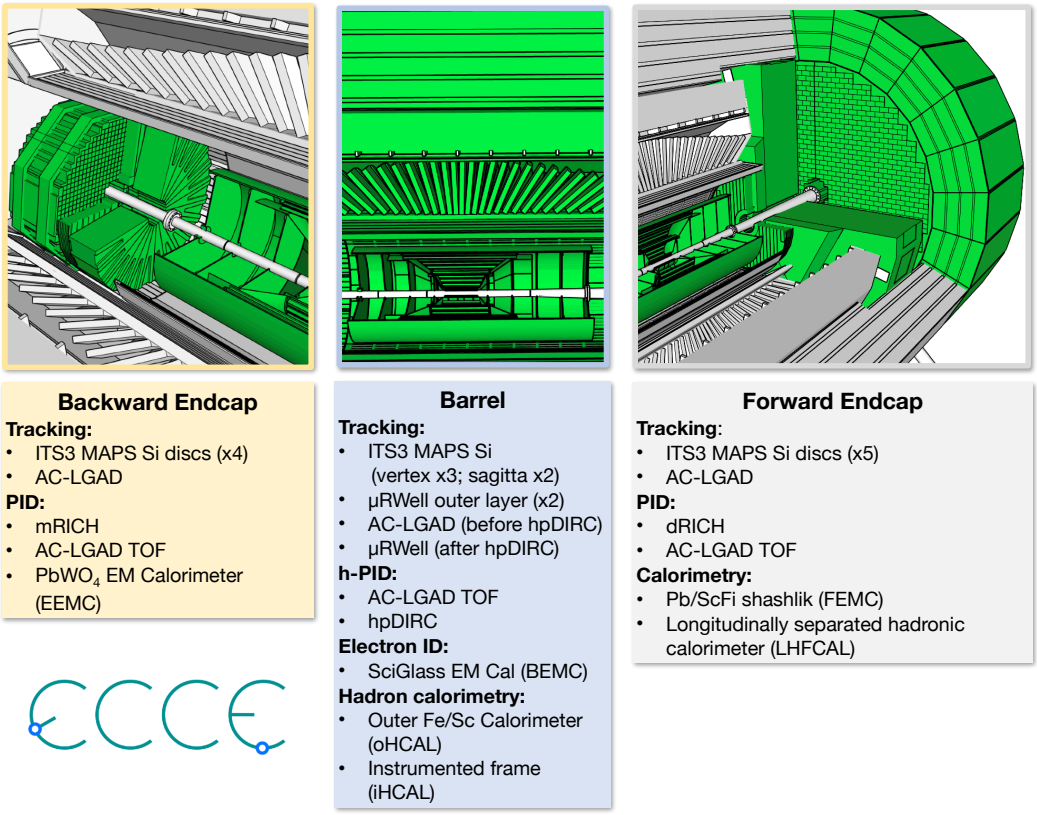

Figure 2.1: Principal components of the ECCE central detector: backward/electron endcap (left), barrel (center), and forward/hadron endcap (right).

Table 2.1: Key detector requirements for ECCE central detector, with associated challenges, and a brief description of the ECCE approach to address each issue.

Topic	Challenge	ECCE solution	Comment
Hermetic e^- coverage	Leave no gaps in e^- EMcal coverage while also folding in PID/hpDIRC readout needs	hpDIRC readout in backward region; Moved EEMC inward as much as possible; Extend BEMC longitudinally	Good coverage for negative rapidity; performance verified with full simulations
Momentum resolution in forward/backward regions at high η	Achieve YR requirements with a realistic tracker including support materials in the BaBar solenoid	Five ITS3 Si disks forward and four disks backward; Additional AC-LGAD tracking before (after) dRICH (mRICH)	Used AI optimization. Upgrade option: AC-LGAD ring in forward region behind dRICH for $\eta = 3$–3.5
Backward Particle Identification	Constrained space to maximize EMCal coverage	AC-LGAD TOF for low-momentum; mRICH for hadron PID	mRICH is a space-efficient solution
Backward e^- PID, π^- suppression up to 10^{-4}	Highest precision EM calorimetry	Use all $PbWO_4$	Can separate out EMCal to reach beyond $\eta = -3.4$
Barrel PID – e/π separation up to 10^{-2}–10^{-4}, down to 0.2 GeV/c	Need good EMcal resolution; need additional e/π below 2 GeV/c	55 cm long SciGlass towers for high precision EMcal; hpDIRC for π veto down to $p = 0.3$ GeV/c; AC-LGAD TOF for $p \leq 0.4$ GeV.	Leave 4 cm for μRWELL between hpDIRC and EMCal to seed PID performance of hpDIRC and improve tacking resolution
Barrel PID – $\pi/K/p$ separation down to 0.2 GeV/c	hpDIRC only covers down to 0.6 GeV/c	AC-LGAD TOF for 0.2 <p <0.6 GeV/c	μRWELL directly after hpDIRC to increase performance.
Barrel Tracking resolution	Achieve YR requirements with a realistic tracker including support materials in the BaBar solenoid	Three ITS3 Si vertex and two Si sagitta layers followed by two μRWELL, AC-LGAD, and far outer μRWELL layer;	Used AI optimization of tracker and support system layout
Forward Hadronic calorimetry	Jet energy resolution $<50\%/\sqrt{E}$	Longitudinally separated calorimeter to meet needs in high-η region.	Upgrade Option: Dual Calorimeter (or only central in region of highest need)
Forward Particle Identification	Constrained space in forward region	AC-LGAD TOF for low- momentum; dRICH for high-momentum (C_4F_{10} based)	Seed dRICH ring finder with AC-LGAD before dRICH; Employ recirculation and gas recovery systems for environmentally unfriendly gas use.

are also provided.

Table 2.2 presents similar information for the far-forward and far-backwards regions. These requirements, which guide our detector design, stem from the needs of the EIC science program presented in the EIC white paper and NAS report, and studied further in the EIC Yellow Report and CDR.

Figure 2.1 shows the ECCE central detector and lists its key components and the technology selected for each sun-system. Here, we provide general technical details on these detector technologies and their implementation:

Magnet ECCE intends to reuse the BaBar superconducting solenoid that is currently planned for use in the sPHENIX experiment and will be available after its conclusion. Its reuse for the EIC was the subject of an engineering study and risk analysis in 2020 [4] whose main conclusion was that the "magnet should be suitable for prolonged use as part of the detector system for the EIC project." Additional performance assessment will be conducted during an sPHENIX long-duration high field test (at 1.4 T) planned in 2022. This test, followed by the first full duration run of sPHENIX in early 2023, will validate the feasibility of its reuse in ECCE. Preparing the solenoid for reuse will involve proactive maintenance and several minor modifications. We also plan to carry through a replacement magnet engineering and design assessment as risk mitigation, as described in Section 2.10.

Electron endcap The ECCE electron endcap region comprises four subsystems:

Tracker The silicon electron endcap detector consists of four disks, which provide precise measure-

Table 2.2: ECCE Detector Far-Forward/Far-Backward requirements

Topic	Challenge	ECCE solution	Comment
Far-Backward – Low-Q^2 Tagger	Measure low-Q^2 photoproduction with as minimal a Q^2-gap as possible.	Spectrometer with AC-LGAD tracking and $PbWO_4$ calorimetry	
Far-Backward – Luminosity Detector	e-ion collision luminosity to better than 1% and relative Luminosity for spin asymmetries to 10^{-4}	Zero Degree Calorimeter with x-ray absorber and e^+/e^- pair spectrometer with AC-LGAD tracking and $PbWO_4$ calorimetry	two complementary detection systems
Far-Forward – B0 Spectrometer	$\eta > 4$ charged particle tracking and γ measurement	Four Si trackers with 10 cm $PbWO_4$ calorimeter	
Far-Forward – Off-momentum Detectors	forward particles (Δ, Λ, Σ, etc) decay product measurement	AC-LGAD detectors	Sensors on one side detect p, on other side p^- from Λ decay; sensors outside beam pipe
Far-Forward – Roman Pots	Detect low-p_T forward-going particles	AC-LGAD detectors	fast timing ($\sim$35 ps) removes vertex smearing effects from crab rotation; 10σ from beam
Far-Forward – Zero-degree Calorimeter	Measure forward-going neutrons γ and heavy-ion fission product	FOCAL-type calorimeter with high-precision EM and Hadron Calorimetry	Upgrade option: AC-LGAD layer to capture very high rapidity charged tracks

ments of charged tracks (especially electron tracks) in the backward pseudorapidity region. The technology for the silicon disk assembly is the ITS-3 silicon sensor with pixel pitch at 10 μm. The detector mechanical structure design will be informed by the EIC eRD111 studies. In addition, the AC-LGAD TOF detectors described below will provide an additional high-precision tracking point after the disks at large distance from the interaction point.

mRICH The design goal of the modular RICH (mRICH) is to achieve 3σ K/p separation in the momentum range from 3 to 10 GeV/c, within the physical constraints of the ECCE detector. It also provides excellent e/p separation for momenta below 2 GeV/c. In addition, the RICH detectors contribute to e/π identification. e.g., when combined with an EM calorimeter, the mRICH and hpDIRC will provide excellent suppression of the low-momentum charged-pion backgrounds, which limits the ability to measure the scattered electron in kinematics where it loses most of its energy.

AC-LGAD TOF TOF measurement using AC-LGAD technology will be used for PID in the momentum range below the Cherenkov detectors thresholds. These detectors also provide a high-precision tracking point.

EEMC The Electron Endcap EM Calorimeter (EEMC) is a high-resolution electromagnetic calorimeter that is capable of providing precision scattered electron and final-state photon detection in the region $-3.7 < \eta < -1.5$, required by the EIC science program. The choice of technology is 2 cm x 2 cm x 20 cm $PbWO_4$ providing 22 radiation lengths and the overall design concept is the same as in the EIC YR.

Fe flux return We will use a passive flux return as we determined there is no substantial benefits to our scientific program by having an active an electron endcap hadron calorimeter. We note that adequate space was left as a possible upgrade path towards high-luminosity running where one might want to measure the jet distribution in the low-x, high-Q^2 region if the physics case would be made.

Central barrel The ECCE central barrel region comprises six subsystems:

Silicon Tracker The silicon barrel detector consists of five layers: three vertex layers close to the beam pipe and two middle layers providing the central track sagitta measurements. All layers use the ITS-3 sensors with pixel pitch at 10 μm with an average material budget of 0.05%X0 per layer.

μRwell Tracker The Si tracker is supplemented by two μRwell layers between the Si sagitta layer and the hpDIRC, and a single outer barrel μRWell layer between the DIRC and BECAL.

AC-LGAD TOF is placed just before the hpDIRC to provide a precise TOF measurement as well as an additional tracking point. See electron endcap discussion for details.

hpDIRC The high-performance DIRC provides particle identification with three standard deviations (s.d.) or more separation for π/K up to 6 GeV/c, e/π up to 1.2 GeV/c, and K/p up to 12 GeV/c.

BECAL The barrel ECAL (BECAL) is a homogeneous projective electromagnetic calorimeter built out of 9088 clear scintillating glass (SciGlass) towers, arranged in 71 rings in the η direction, with 128 towers per ring along ϕ. The SciGlass towers have a front face of 4 cm$\times$4 cm and are 55 cm deep including $\sim$10cm readout, providing 17 radiation lengths and better than $4\%/\sqrt{(E)}$ + (1–2)% resolution. This resolution surpasses the EIC YR requirement to complement the tracking system and ease electron identification and π/e rejection, with an eye to the future high-luminosity EIC science needs. Their shape is slightly tapered to be nearly projective to the interaction point.

IHCAL/OHCAL The ECCE outer barrel hadronic calorimeter (oHCAL) is integrated into the barrel flux return for the ECCE solenoid magnet. and is a reuse from the sPHENIX experiment. Its design consists of 32 sectors of 1020 magnet steel, with an inner and outer radii of 1.9 m and 2.6 m respectively. Each sector is 6.3 m long and weighs 14 tons. The barrel inner HCAL (iHCAL) is a hadronic calorimeter that is integrated into the BECAL support frame. Its design consists of 32 sectors of stainless steel, with an inner radius of 135 cm and an outer radius of 138.5 cm.

Hadron endcap The ECCE hadron endcap region comprises five subsystems:

Tracker The silicon hadron endcap detector consists of five disks, which provide precisely measured space points for charged particle tracking in the forward pseudorapidity region. This detector will enhance the capability to determine the decay vertex of long decayed particles and measure the majority of charged particles in the asymmetric $e + p$ and $e + A$ collisions. The technology for the silicon disk assembly is ITS-3 silicon sensor with pixel pitch of 10 µm. The detector mechanical structure design will be informed by the EIC eRD111 studies. An AC-LGAD TOF detector placed in front of the dRICH will provide an additional high-precision tracking point.

AC-LGAD TOF See electron endcap for details.

dRICH The dual-radiator Ring Imaging Cherenkov (dRICH) detector is designed to provide continuous hadron identification in the (outgoing) ion-side with 3 s.d. or more for π/K from $\sim$0.7 GeV/c to $\sim$50 GeV/c, and for e/π from a few hundred MeV/c up to $\sim$15 GeV/c.

FEMC The forward ECal (FEMC) will be a Pb-Scintillator shashlik calorimeter. Its towers have an active depth of 37.5cm with an additional 5cm readout space. Each tower consists out of 66 layers of alternating 1 cm$\times$1 cm$\times$0.16 cm Pb and 1 cm$\times$1 cm$\times$0.4 cm Scintillator material.

LFHCAL The forward HCal (LFHCAL) is a steel-scintillator calorimeter. Its towers have an active depth of 1.4 m with an additional space for the readout of about 20-30 cm depending on their radial position. Each tower consists out of 140 layers of alternating 5cm x 5cm x 1.6cm steel and 5cm x 5cm x 0.4cm scintillator material. In each scintillator a loop of wavelength shifting fiber is embedded. 10 consecutive fibers in a tower are read out together by 1 Silicon photo multiplier, leading to 7 samples per tower.

Far-forward detectors The auxiliary detectors consist of a set of trackers and calorimeters that are, in general, closely integrated with the beam elements. The systems are designed to measure very forward and backward particles to high precision with a high rejection of beam related background. The far forward and far backward detection system consists of the following components:

B0 spectrometer The B0 spectrometer measures charged particles and photons at forward ($\eta > 3$) angles to facilitate studies if exclusive processes and general process characterization. This subsystem is designed for reconstructing charged particles with angles $5.5 < \theta < 20.0$ mrad, and also large angle protons from nuclear breakup. The B0 detector is embedded in the first dipole

magnet after the interaction point (B0pf). It consists of four layers of AC-LGAD tracking planes followed by an array of $PbWO_4$ crystals for the photon detection. The $PbWO_4$ array consists of 250 crystals, each 10 cm long with a surface area of 2x2 cm^2 to enable measurement of processes such as u-channel DVCS.

Zero-Degree Calorimeter The ZDC consists of four different calorimeters.

- $PbWO_4$ Crystal calorimeter: For good measurement of low energy photons. In front of the crystal layer, a silicon pixel layer is attached.
- W/Si sampling calorimeter: This is an ALICE FoCal-E style calorimeter and consists of alternating tungsten plates and silicon sensor planes. It is meant to measure the residual photon energy escaping the $PbWO_4$ Crystals and the shower development of photons and neutrons.
- Pb/Si sampling calorimeter: This is a calorimeter with 3 cm-thick lead plane absorbers and active silicon pad layers, where the pad-layer design is as in the W/Si calorimeter.
- Pb/Sci. sampling calorimeter: This is to measure hadron shower energy and uses 3 cm thick lead plane absorbers with 2 mm-thick scintillator planes as active materials. The calorimeter is segmented as 10 cm x 10 cm on a plane and 15 layers of scintillator planes will be read together, making a tower.

Far-backward detectors The auxiliary far-backward detectors consist of a set of trackers and calorimeters.

Low-Q^2 tagger Two detection systems located at different distances from the bean, each including two AC-LGAD tracking layers followed by a high-resolution $PbWO_4$ calorimeter.

Luminosity monitor Forward $PbWO_4$ calorimeter with a passive x-ray absorber and a two-arm e^+/e^- pair spectrometer. Each are includes with AC-LGAD tracking layers and a high-resolution $PbWO_4$ calorimeter.

Electronics/DAQ The ECCE DAQ is a fully streaming readout (SRO) design capable of supporting high bandwidth to the Event Buffer and Data Compressor (EBDC) computers as well as high bandwidth to the data storage. A key component of this design is the Data Aggregation Module (DAM), the model for which we take as the current ATLAS FELIX board that will be used by sPHENIX in their hybrid streaming DAQ. We assume the development of a specific iteration of a FELIX-like board [5] as the DAM board for ECCE (also referred to as "EIC-FELIX" in the text that follows) that will serve as a common interface for all the subsystems. The use of a common interface reduces the number of electronics designs that needs to be verified and supported throughout the lifetime of the experiment.

The general design of the ECCE data acquisition builds on the sPHENIX DAQ system, which already incorporates and demonstrates almost all concepts of the envisioned ECCE DAQ system. However, while sPHENIX had to be a hybrid of triggered and streaming readout components, the ECCE DAQ will be built around a trigger-less Streaming Readout (SRO) concept from the start, similar to many of the JLab streaming readout systems currently under test.

Computing ECCE computing will be based on a distributed model with multiple sites for calibration, storage and computing. The model calls for disk space sufficient for holding up to 3 weeks of data so calibrations can be generated and reconstruction done in near-time. Tape storage will be used for backup, but will not be part of the primary pipeline for analysis.

Infrastructure The detector infrastructure consists of the conventional mechanical and electrical facilities necessary to construct and operate the detector. Specific components to ECCE are: specialized carriage and structural components, specialized installation engineering and components.

Figure 2.2 shows the material distribution of the ECCE central detector via a radiation length scan of the detailed ECCE GEANT4 model. The large acceptance and low mass inner tracker (green) is hermetically enclosed by the PID detectors (red and yellow) and EM calorimetry (blue). Hadronic calorimeters further cover $\eta > -1.1$.

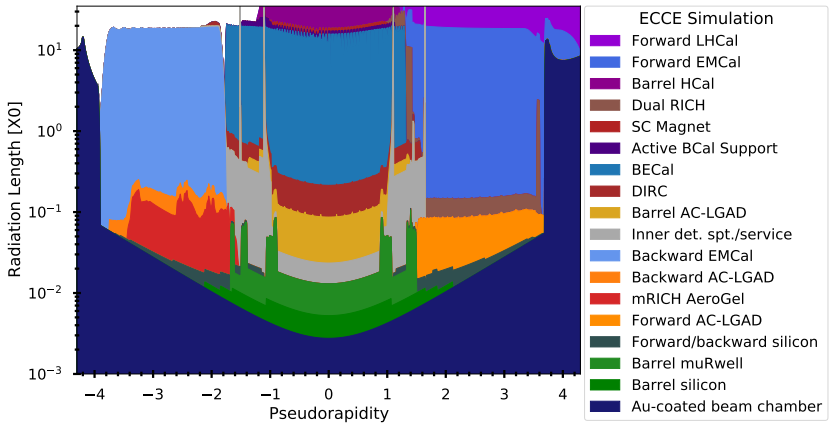

Figure 2.2: The stacked plot of material distribution in the ECCE detector subsystems, which is quantified as the radiation length that photons from the central interaction point observe and is averaged over azimuth.

Figure 2.3: The BaBar solenoid in October 2021, during installation in the sPHENIX experiment. The solenoid is resting in the barrel outer hadronic calorimeter and flux return, which will be completed with additional sectors in the coming months. The barrel flux return (outer hadronic calorimeter) and BaBar solenoid are items planned to be reused by the ECCE experiment. The experimental cradle may also be reused.

2.2 Magnet

The BaBar superconducting solenoid will be repurposed for the ECCE experiment. It was previously moved from SLAC to BNL for use in the sPHENIX experiment at RHIC. ECCE plans to reuse the BaBar/sPHENIX solenoid and the surrounding combined hadronic calorimetry and flux containment system for the magnet.

The magnet for the BaBar experiment at PEP-II at SLAC was manufactured by Ansaldo in 1997 and commissioned in 1998. It was transferred to BNL in 2015 for use in the sPHENIX experiment and passed an initial high-field test (up to 1.3 T) in 2018. Its main design parameters are listed in Table 2.3. For an EIC detector the region covered by the barrel detectors should span a pseudo-rapidity $-1 < \eta < 1$, corresponding

Table 2.3: Design parameters of the BaBar superconducting solenoid.

Central Induction	1.5 T* (1.4 T in ECCE flux return)
Conductor Peak Field	2.3 T
Winding structure	Two layers, graded current density
Uniformity in tracking region	$\pm$3%
Winding Length	3512 mm *at R.T.*
Winding mean radius	1530 mm *at R.T.*
Operating Current	4596 A (4650 A*)
Inductance	2.57 H (2.56 H*)
Stored Energy	27 MJ
Total Turns	1067
Total Length of Conductor	10,300 m

* Design Value

to an angle of $\sim$40 degrees. This corresponds well with the BaBar solenoid, which has a warm bore diameter of 2.84 meters and a coil length of 3.512 meters, corresponding to a 39 degree angle.

The reuse of the BaBar solenoid for the EIC was the subject of an engineering study and risk analysis in 2020 [4]. The main conclusion of the assessment was that the "magnet should be suitable for prolonged use as part of the detector system for the EIC project." The report also suggested the implementation of several maintenance and improvement modifications, including new protection circuits such as voltage taps, inspection and, as needed, reinforcement of the internal mechanical support, including new strain gauges, and replacement of control instrumentation sensors. The implementation of some of these suggestions would involve opening the magnet cryostat, which would create additional risk of magnet failure. In 2021 JLab engineers revisited the risk analysis and, following extensive discussions, decided that any modifications or refurbishment that require opening the BaBar solenoid cryostat would not be worth the additional risk [6]. They further noted that no such actions will be necessary if the magnet continues to operate well throughout a high-field magnet test with the sPHENIX experiment flux return (which will also be re-used for ECCE) in mid-2022 and subsequent initial sPHENIX experimental operations starting in 2023 (until 2025).

Further magnet engineering studies of the ECCE detector magnet indicate that the unbalanced forces on the magnet are small, a net force of 4kN or less than 1000 lbs, because the magnetic field at the locations of the ECCE forward and backward calorimeters are small and most of the magnetic flux is returned through the barrel. These small forces should not present a substantial engineering difficulty in the proposed ECCE configuration.

The scope of the reuse of the BaBar solenoid in ECCE includes a review by a panel of experts (following initial sPHENIX running), the disconnect of the magnet in IP-8 and move to IP-6, a new valve box, and assembly and magnet mapping in IP-6. The risk mitigation strategy associated with the reuse of the BaBar solenoid, including the design of a potential replacement magnet, are discussed in Section 2.10.

2.3 Tracking

ECCE features a hybrid tracking detector design (Figure 2.4) using three state-of-the-art technologies to achieve high precision primary and decay vertex determination, fine tracking momentum and distance of closest approach resolution in the $|\eta| \leq 3.5$ region with full azimuth coverage [7]. The ECCE tracking detector consists of the Monolithic Active Pixel Sensor (MAPS) based silicon vertex/tracking subsystem, the μRWELL tracking subsystem and the AC-LGAD outer tracker, which also serves as the ToF detector. The ECCE tracking design has been optimized assisted by Artificial Intelligence (AI) as further discussed below

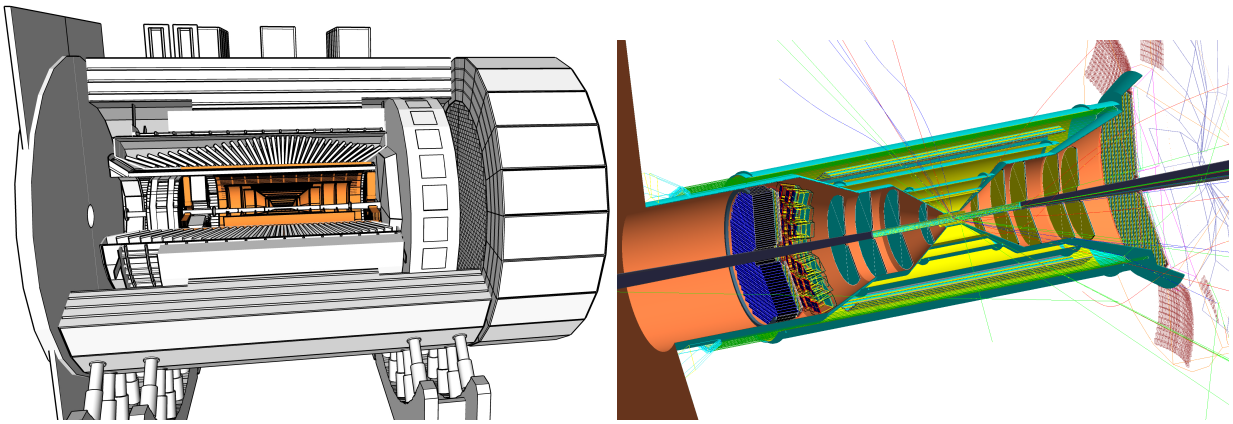

Figure 2.4: Tracking system of ECCE in mechanical model (left) and GEANT4 simulation (right). The tracking system is tightly integrated with the PID detectors which is also shown on the right. Support and cabling for the these detectors was implemented (copper-colored cylinder-cone) to count for its material and acceptance effects.

taking into account BaBar magnet coverage, integration with the other detector subsystems, and cost.

The detector geometry is shown in schematic form in Fig. 2.5 which displays the detector in the $R-z$ plane. The barrel layers centered at $z = 0$ have a cylindrical geometry, while the endcap layers centered at $R = 0$ are disks oriented around the z axis. The MAPS silicon detector contains 3-layer silicon vertex layers, 2-layer silicon sagitta layers, five disks in the hadron endcap and four disks in the electron endcap region. This silicon vertex/tracking detector provides the desired primary vertex and displaced vertex reconstruction also documented in the EIC yellow report [8] and the essential tracking momentum and DCA_{2D} resolutions (see Fig. 2.7 and Fig. 2.8) for heavy flavor measurements. For the barrel at large radii, which have the largest surface area, cylindrical μRWELL gas trackers are used to optimize performance at reduced overall cost. These are introduced both right outside the Si tracker and in front of the barrel EM calorimeter. In addition, an AC-LGAD based ToF layer in each section provides a precision space-time measurement on each track. The tracking system is thus tightly integrated with the PID detectors.

2.3.1 MAPS

The silicon vertex and sagitta layers utilize Monolithic Active Pixel Sensor (MAPS) technology, as implemented in high-precision (10 μm pixel pitch) low-material (0.05%/layer) ALICE-ITS-3-type sensors [9,10], used in both cylindrical and disk configurations.

The MAPS detector systems have been costed using the TowerJazz 65nm production line. This technology is in the prototype sensor design and characterization stage. Recent R&D on the ITS-3 has delivered a 32 by 32

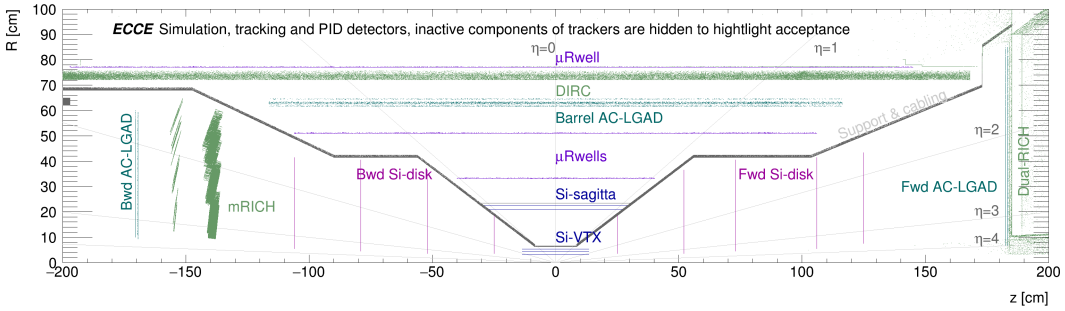

Figure 2.5: Schematic view of the ECCE tracker, including silicon, μRWELL, AC-LGAD, DIRC, mRICH and dRICH detector systems.

pixel matrix prototype sensor using the 65nm production line that is undergoing beam test studies at CERN. Validation of the curved ALPIDE (ITS-3) sensor performance has obtained by early beam test results. The mechanical design for the silicon tracking detector, especially for the stave and disk layout and assembly, is led by the ongoing EIC R&D project eRD111. Reduction of the material budgets for the EIC silicon tracking detector service parts is also being studied as part of the EIC eRD104 project. Alternative silicon technologies have been explored such as the Depleted MAPS (DMAPS), and progress in the MALTA DMAPS technology has been reported in [11]. All these R&D activities align with other major project upgrades or construction projects such as the ALICE ITS-3 upgrade. The required sensor R&D is included in the ECCE detector R&D plan.

2.3.2 μRWELL

The μRWELL technology is a single-stage amplification Micro Pattern Gaseous Detector (MPGD) that is a derivative of the Gas Electron Multiplier (GEM) technology. It features a single kapton foil with GEM-like conical holes that are closed off at the bottom by gluing the kapton foil to a readout structure to form a microscopic *well* structure. The technology shares similar performances with a GEM detector in term of rate capability, while providing a better spatial resolution than GEM. Furthermore, compared to GEMs, μRWELL presents the advantages of flexibility, more convenient fabrication and lower production cost that makes it the ideal candidate for large detectors. Large area μRWELL foils have already been developed and manufactured at CERN. In ECCE μRWELL layers will form three barrel tracking layers further out from the beam-pipe than the silicon layers. The barrel gas tracker layers include two inner barrel μRWELL layers, as well as a single outer barrel μRWELL. All μRWELL detectors will have 2D strip based readout. The strip pitch for all three layers will be 400 μm. Figure 2.6 shows the resolution results from a μRWELL prototype detector in test beam at Fermilab (June-July 2018) as part of the EIC eRD-6 activities. The measurements were done using a beam hitting the detector perpendicularly, and using detailed MC simulations we estimate a 55μm resolution for a curved geometry where the particle hits the detector at an angle. Funding was recently secured, and work is underway by ECCE collaborators to build and test large area cylindrical μRWELL detectors.

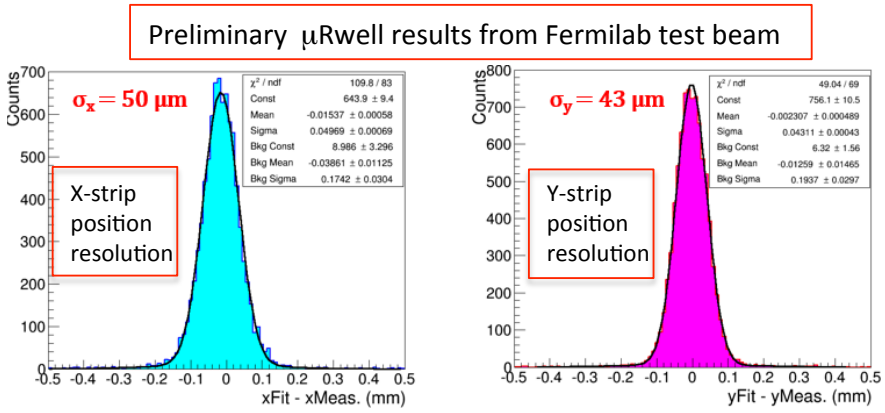

Figure 2.6: Preliminary results of spatial resolution performances of the μRWELL prototype with 2D X-Y strip readout layer.

The Korean institutions in the ECCE collaboration will manufacture the μRWELL foils for the ECCE μRWELL detectors. Specifically, a Korean manufacturer (Mecaro) has demonstrated that they can produce high quality large MPGD foils for the CMS detector at the LHC, working in conjunction with member institutions of the Korean ECCE collaboration. In addition, Chinese institutions in the ECCE collaboration have experience with the DLC resistive coating required for μRWELL detectors. We are confident that the foreseen arrangement will be successful.

2.3.3 AI optimization

A detailed study of the detector design with AI has been accomplished during the ECCE detector proposal development and a framework for Multi-Objective Optimization (MOO) has been incorporated in the ECCE detector design simulation. AI has played a crucial role in choosing the combination of technologies for the inner tracker. The choice of having ITS-3 and the μRWELL gas tracking layers, as well as the disk minimum radii were supported by AI. This has been an iterative process that evolved over time and required interplay between the ECCE teams working on Physics, Detector and Computing.

Our approach deals with a complex optimization in a multidimensional design space driven by multiple objectives that encode the detector performance, while satisfying several mechanical constraints. This framework has been developed for the optimization of the inner tracker of ECCE and can in principle be extended to another sub-detector or to a system of sub-detectors, provided a viable parametrization of the detector simulation can be produced. Different parametrizations of the inner tracker design have been explored and most of our studies have been characterized by at least 11 parameters in the design space characterizing the location of the tracking layers in the central region and the disks in the two endcaps. The parametrization has been extended to include the support structure in the design optimization process and more recently to the outer tracking layers. The different designs have been optimized with particle gun samples of pions and then studied and validated with independent data samples and physics analyses. At least three objective functions have been optimized simultaneously. In particular, for a 3-objective problem we utilized the momentum resolution, the polar angular resolution along with the Kalman filter efficiency of π tracks. This problem has been tackled with evolutionary algorithms to assist the design during the detector proposal. A recently developed framework for MOO, PYMOO [12], has been implemented which supports algorithms like NSGA-II and NSGA-III [13] and distributed evaluation with task scheduler like DASK [14].

This approach accommodated both mechanical and geometrical constraints during the optimization process. In our studies we included at least 5 constraints (*e.g.*, the outermost location as well as the difference between the outer and inner radius of a disk, or the radius of the outermost layer in the inner tracker). Overlaps in the design are excluded by a combination of constraints, ranges for the exploration of the parameters and internal checks done before and during the entire optimization process. Further details can be found in [15].

The AI-assisted design has been used as input to multiple iterations of the ECCE tracker design, which led to the current tracker layout [7] (Fig. 2.4 and 2.5), and is also contributing to the ongoing project R&D to reduce the impact of readout and services on the tracking resolution as discussed in Section 2.3.6.

2.3.4 Expected backgrounds

Vacuum and background estimates were done in joint working group meetings across proto-collaborations. A detailed simulation study was carried out to assess the collision signal and background from beam gaps and Synchrotron radiation on tracking detectors in BaBar magnetic field [16]. Although the beam gas background was found to be small, the Synchrotron radiation on the MAPS-based silicon trackers can be very significant and its uncertainty is large at this stage of the EIC design. A high-Z coating in the Be-section of the beam pipe (e.g. 2 μm Au coating) was shown to reduce the Synchrotron hit rate in the silicon vertex tracker by four orders of magnitude resulting in a manageable hit rate [16, 17]. Therefore, all ECCE studies adopted such Synchrotron shielding coating which introduces 0.06% X_0 (at $\eta = 0$) of additional material to the beam pipe ($\sim$ 30% relative increase).

2.3.5 Tracking performance

The performance of the ECCE reference tracker design has been studied using single pions propagated through the ECCE GEANT4 simulation framework. The momentum resolution is presented in Fig. 2.7 with the YR requirement indicated as the dash lines. In the region ($-1 < \eta < 3.0$) the ECCE momentum resolution is consistent with YR physics requirements for all bins. We note that between $1 < \eta < 1.5$ we do see a substantial deviation that is not obvious in Figure 2.7. This difference is expected, as ECCE simulations take into account material for readout and services (copper-colored structure in right of Figure 2.4), whose

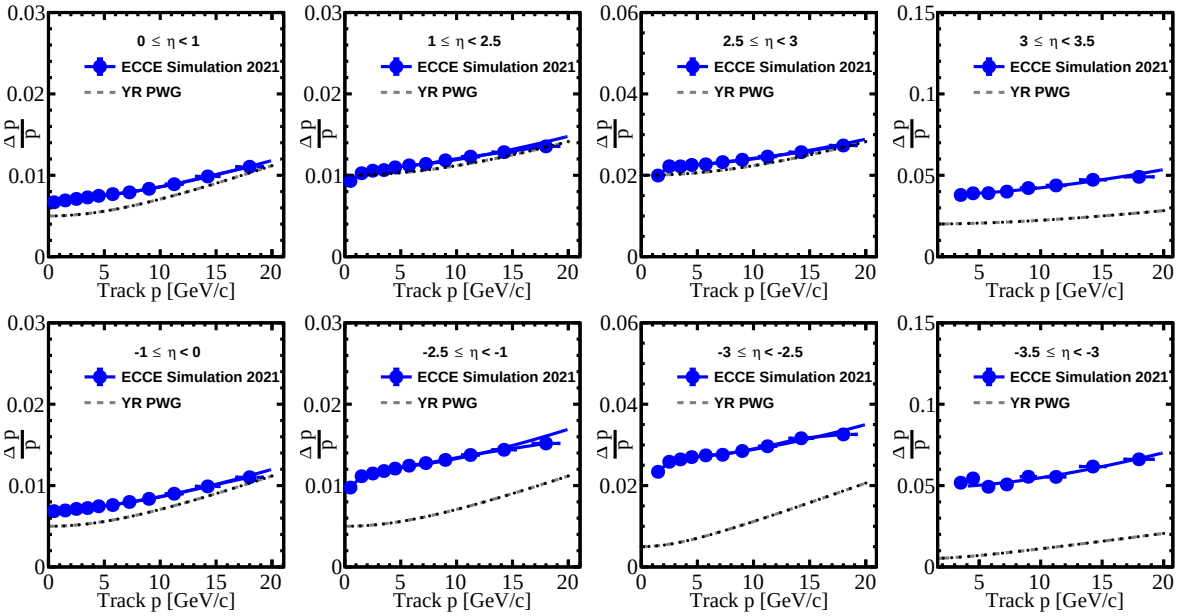

Figure 2.7: ECCE pion track momentum resolution (data points) with the EIC YR PWG requirements for the tracker indicated by the dashed lines. Note that the ECCE performance simulations take into account materials for readout and services. The impact of these can be observed most clearly in the bins covering the barrel/barrel endcap transition regions. As an integrated EIC detector with all subsystems operating in a complementary way, ECCE achieves the EIC physics goals as described in Chapter 3.

impact is largest in this region. Further AI-assisted optimization in this region is on-going as discussed in Section 2.3.6. In the backward region $\eta < -1.0$ and in the most forward bin the ECCE momentum resolution provided by tracking is larger than what is required by the YR requirements. However, ECCE is an integrated detector and in this region the physics performance, and in particular for $\eta < -2.5$, is achieved through excellent EM calorimetry as discussed in Section 3. Due to the limited time since the call for proposals to produce and analyze complete GEANT4 simulations for physics performance, many of the physics studies in Section 3 use the tracking alone without the improvements that calorimetry can provide. Nevertheless, these studies all show excellent performance for EIC physics. The addition of the calorimetry information will only improve these results, as shown for key physics topics. We further note the dominant YR requirement for the momentum resolution in the backward region is driven by coherent J/ψ production on the nuclei, and in particular the t-reconstruction from the forward particles. Nonetheless, the ECCE physics studies have shown that for both 1.4 T and 3,0 T field strengths the t-reconstruction resolution is dominated by the calorimeter (see section 3.6 for details).

The resolution of measurements of distance-of-closest-approach (DCA_{2D}), which is critical for heavy flavor measurements, is provided in Fig. 2.8 and also compared with YR requirement. The ECCE DCA resolution is consistent with YR requirements, and delivers robust physics programs in heavy flavor measurements and beyond standard model search as detailed in Chapter 3.

2.3.6 Ongoing R&D for support structure optimization

Given the importance of the service structure in the tracking detector, the reduction of the impact of readout and services on tracking resolution is subject of ongoing R&D and ECCE has made tremendous progress on this front using AI. The AI investigation in the ECCE framework focused on optimizing the tracker design with a projective support cone structure that reduces the amount of material a particle traverses. The design concept is illustrated in the Tracking Tech Note [7] and more details on the AI based studies can be found in [15]. The momentum resolutions resulting from this investigation are shown in Fig. 2.9. The largest impact is in the region between central barrel and endcaps ($1 < \eta < 1.5$ and $-1.5 < \eta < -1$) while the

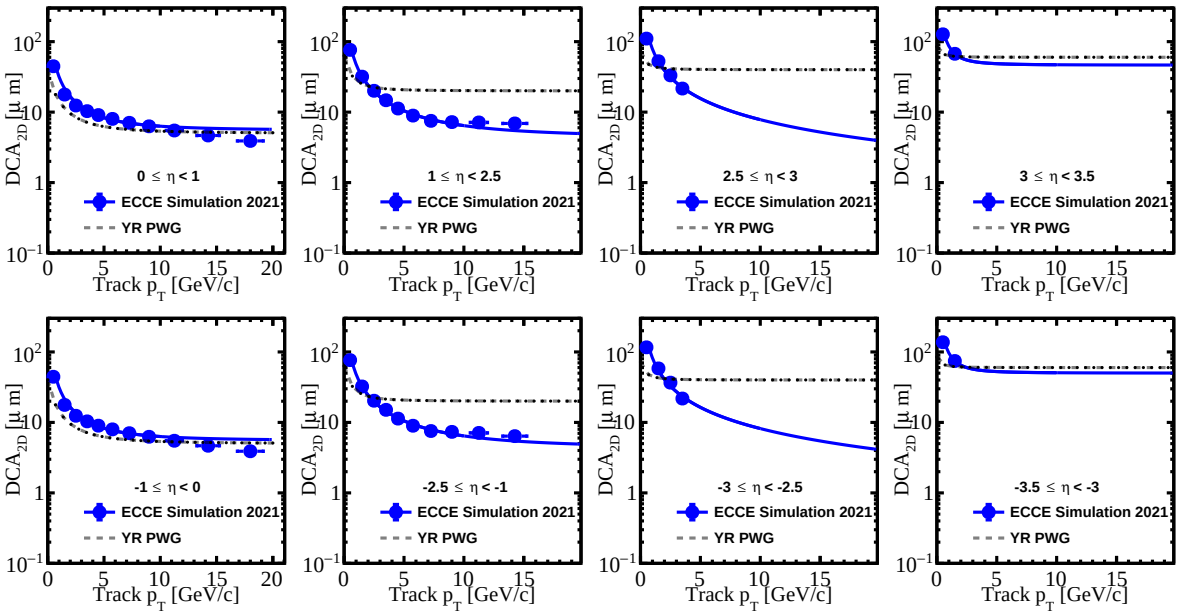

Figure 2.8: Pion DCA_{2D} resolutions (data points), which is compared to the EIC YR PWG requirement (dashed lines). The ECCE DCA resolution is consistent with YR requirements.

tracking momentum resolution in the central barrel as well as at large pseudo-rapidities ($|\eta| > 1.5$) is largely unaffected.

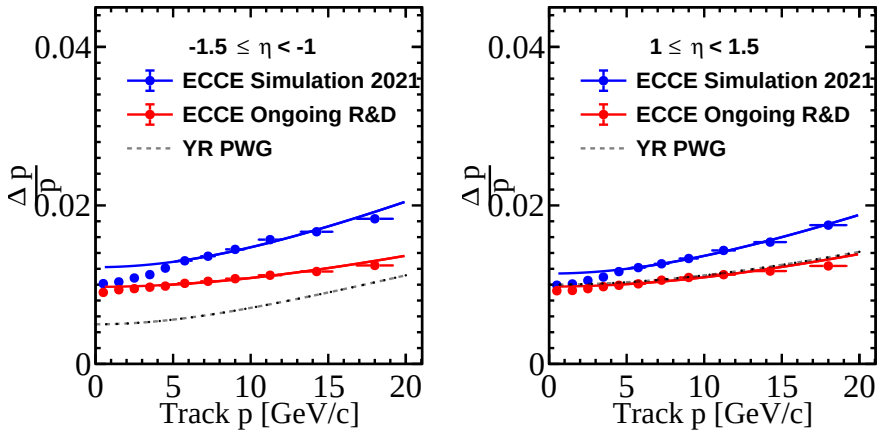

Figure 2.9: The momentum dependence of the tracker momentum resolution for the ECCE reference tracker design (ECCE Simulation, blue solid circles) and for the projective mechanical support design of the ECCE ongoing project R&D that will continue after the proposal (red solid circles). The latter shows a reduction of the impact of readout and services on the tracking resolution. Note that the backward region (left panel) relies on the EM calorimeter, and thus a resolution larger than the EIC YR PWG requirement is acceptable.

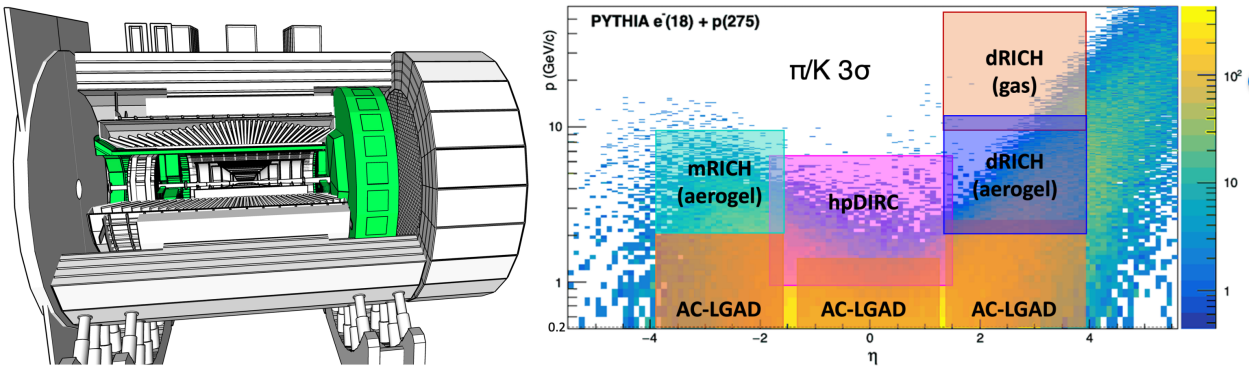

Figure 2.10: Left: 3D model of the ECCE detector with the PID systems highlighted. Right: Expected 3 s.d. π/K separation coverage for the ECCE PID systems as a function of the particle momentum and pseudo-rapidity. Full coverage is achieved by making use of the veto mode of the Cherenkov detectors, complementing the TOF PID in the low momentum region.

2.4 Particle Identification

The ability to identify hadrons in the final state is a key requirement for the physics program of the EIC. Being able to tag the flavor of the struck quark in semi-inclusive DIS can, for instance, provides valuable information about the transverse momentum distributions (and potentially orbital angular momentum) of the strange sea, while open charm (with subsequent decays into kaons) is important for probing the distribution of gluons in protons and nuclei.

The choice of ECCE PID detector technologies was based on the outcome of the EIC generic R&D program (eRD14 EIC PID Consortium and eRD29 on TOF with the LGADs technology), started in 2015, and in line with the baseline EIC detector concept in the Yellow Report (YR) [8]. The longitudinally compact, modular RICH (mRICH), the radially thin high-performance DIRC (hpDIRC), the dual-radiator RICH (dRICH), and AC-LGADs based TOF, provide excellent PID over a wide momentum range for the full final state phase space [18]. The geometries of all PID detectors were optimized to fit the ECCE baseline design while maintaining the required performance. Figure 2.10 (left) shows the four PID systems in a 3D model of the ECCE detector and (right) their π/K separation coverage as a function of momentum and pseudo-rapidity for a sample of physics events. Compared to the YR reference detector, a number of key design features of the PID systems were optimized for ECCE.

The expected PID performance of the three ECCE Cherenkov detectors was obtained from standalone GEANT4 simulation and analytical calculations, parametrized and used as input into the ECCE physics

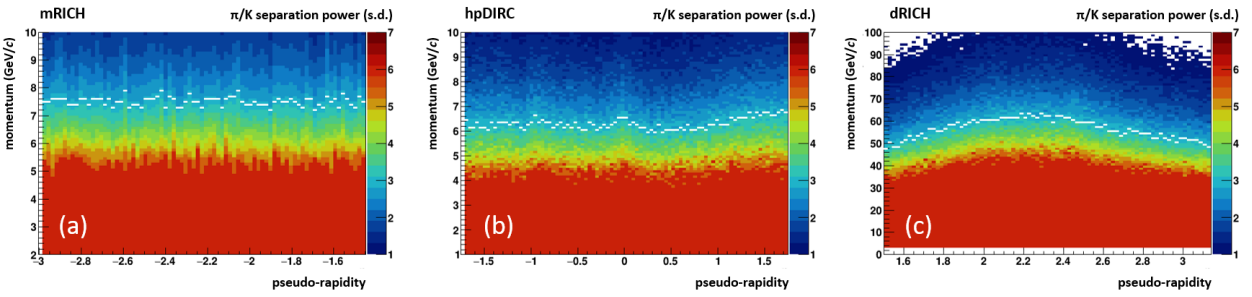

Figure 2.11: Parametrized π/K separation power in ECCE as a function of particle momentum and pseudo-rapidity for mRICH (a), hpDIRC (b), and dRICH (c) based on standalone full GEANT4 simulation and analytical calculation. The white symbol marks the maximum momentum for 3 s.d. π/K separation in each pseudo-rapidity bin.

studies. Figure 2.11 shows the parametrized π/K separation power in units of the number of standard deviations as a function of pseudo-rapidity and momentum for conservative assumptions for the tracking angular resolution.

Note that subsequent tuning of the PID detector geometries and reconstruction algorithms resulted in further improvement of the PID performance, which are not reflected in the shown parametrization. The resulting momentum coverage for the separation of e/π, π/K, and K/p with three standard deviations or more is summarized in Table 2.4 for the three ECCE Cherenkov systems. The Cherenkov system performance is further separated into the nominal "Ring Imaging" mode of operation, which provides positive ID of the particle type, and the so-called "threshold mode" or "veto mode", which uses the number of Cherenkov photons in excess of the expected background to differentiate between particle types above or below the threshold for Cherenkov light emission. The combined performance of the ECCE Cherenkov detectors meets or exceeds the ECCE PID requirements.

Table 2.4: Summary of the PID performance of the ECCE Cherenkov systems (momentum coverage in GeV/c).

PID	Mode	mRICH	hpDIRC	dRICH	
				aerogel	gas
π/K	Ring Imaging	$2-9$	$1-7$	$2-13$	$12-50$
	Threshold	$0.6-2$	$0.3-1$	$0.7-2$	$3.5-12$
e/π	Ring Imaging	$0.6-2.5$	<1.2	$0.6-13$	$3.5-15$
	Threshold	<0.6	–	<0.6	<3.5

The Cherenkov systems provide, in addition to hadron PID, a significant contribution to the e/π identification. When combined with the EM calorimeter, the mRICH and hpDIRC will provide excellent suppression of the low-momentum charged-pion backgrounds, which otherwise limit the ability of the EMCal to measure the scattered electron in kinematics where it loses most of its energy. The time-of-flight (TOF) system, using the AC-LGAD technology, will provide hadronic PID and electron identification in the momentum range below the thresholds of the Cherenkov detectors and provide a time resolution of 25 ps and a position resolution of about 30 μm over a 4π coverage.

Figure 2.12 shows the realistic ECCE magnetic field with highlighted PID detectors envelopes. In the region of the hpDIRC detector plane, where the MCP-PMTs will be located, the magnetic field is at a level of 0.3–0.4 T, which provides a large safety margin in terms of the MCP-PMT field tolerance. Both RICH detectors in ECCE assume SiPM, which are insensitive to magnetic fields of this strength, as their baseline photosensor. Bending of the charged particle tracks in RICH detectors can have an impact on the performance, but no significant sensitivity was observed in the ECCE simulation studies so far.

2.4.1 mRICH

The novel design of the mRICH modules consists of four components. A block of aerogel serves as the Cherenkov radiator, immediately followed by an acrylic Fresnel lens, which focuses the ring image and acts as a UV filter. A pixelated optical sensor is located in the image plane, and flat mirrors form the sides of each mRICH module.

Several optimizations of the ECCE mRICH design were made compared to the YR reference detector: (1) the projective array design was optimized maximizing the acceptance, removing the polar-angle dependence, and reducing the material budget; (2) the dead region between the mRICH modules is minimized using optimized thin module walls and mirrors (shorter as well) (3) an integrated mRICH array mechanical design was designed, consistent with the simulated array configuration in GEANT4.

To study the performance of mRICH setup in ECCE, a set of tracks from the most demanding parts of the phase space were used, where the performance is expected to deteriorate, setting a lower limit on the performance and comparing it to what we see from the parametrizations. The study specifically focuses on the cases where the particles are incident at the surface of the aerogel closer to the outer edges with an outward angles and tracking angular resolution of 2.5 mrad. Fig. 2.13 shows the results for the e/π and

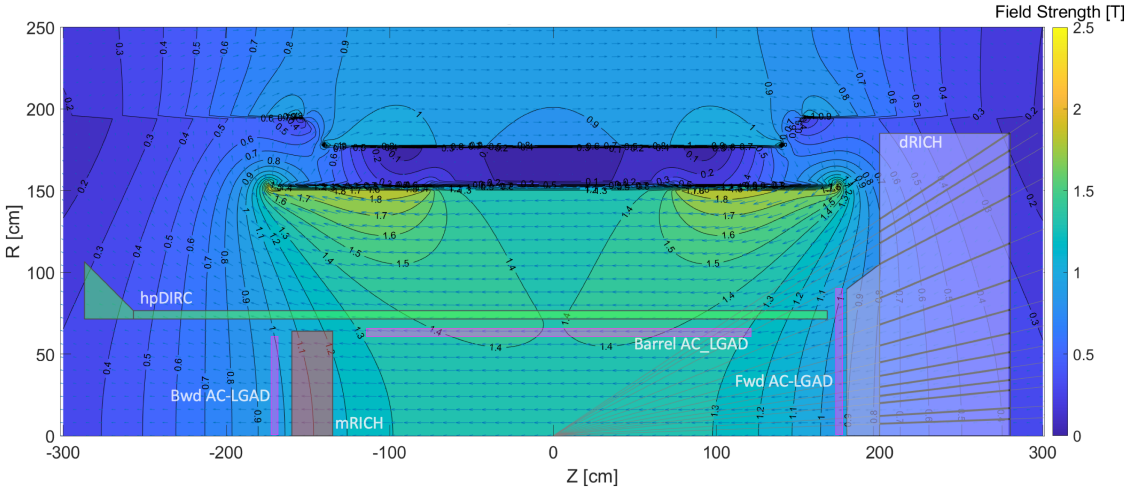

Figure 2.12: ECCE magnetic field map with the PID detector envelopes overlaid.

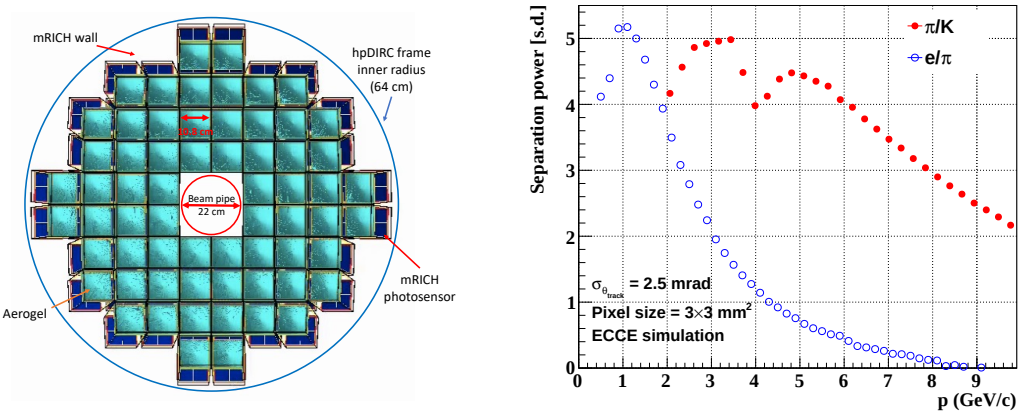

Figure 2.13: Left: Front view of mRICH module array in the allocated space projected towards the IP. Right: The separation power of the mRICH in units of number of standard deviations (s.d.) as function of particle momentum from ECCE simulation.

π/K separation. The dips in the π/K separation at 2 and 3.8 GeV/c are due to the Cherenkov thresholds for kaons and protons in the aerogel. The obtained results show better performance than that used in the parametrization, shown in Fig. 2.11a, which indicates a better momentum reach once the mRICH reconstruction is further optimized.

2.4.2 hpDIRC

The radially-compact hpDIRC is based on a fast focusing DIRC design. Thin rectangular bars, made of synthetic fused silica, serve as Cherenkov radiators and guide the photons to the readout section where they are focused by a lens and recorded by an array of pixelated photon sensors, placed on the back surface of a fused silica prism expansion volume. Key features of the hpDIRC include three-layer spherical lenses, photosensors with small (3 mm$\times$3 mm) pixels, and fast readout electronics.

Compared to the YR reference detector, several hpDIRC design aspects were optimized for ECCE. The expansion volume and readout were moved from the hadron side to the electron side for better detector integration and to minimize gaps in the EM calorimeter coverage. The bar box radius was decreased to match the EM calorimeter barrel size and the number of bar boxes, as well as the number of bars per bar box,

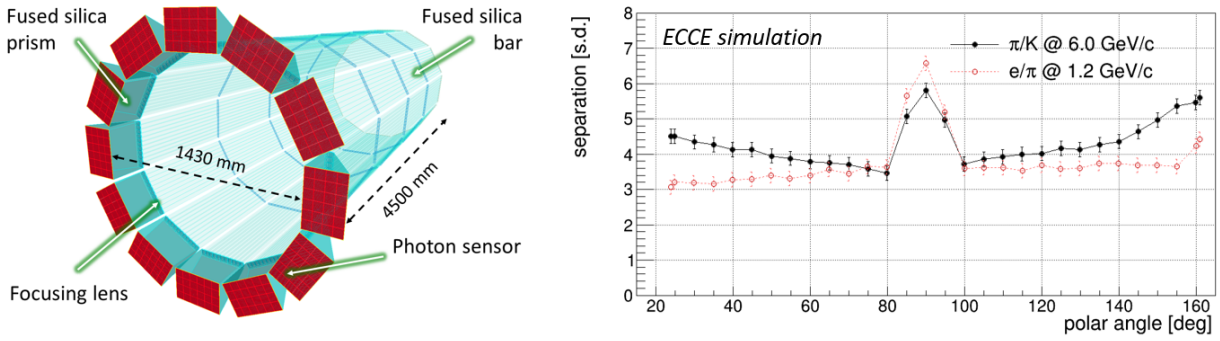

Figure 2.14: hpDIRC geometry (left) and expected PID performance (right) from the GEANT4 standalone simulation. The e/π and π/K separation power is shown in units of number of standard deviations (s.d.) as a function of the particle polar angle for e/π at 1.2 GeV/c and π/K up to 6 GeV/c.

were tuned to optimize the azimuthal coverage of the hpDIRC and to be consistent with the reuse of the BaBar DIRC bars. None of these changes had a significant impact on the performance of the hpDIRC.

Figure 2.14 shows the hpDIRC geometry as well as and the expected performance of the hpDIRC from the standalone GEANT4 simulation studies for two particular cases. The black points show the separation power for charged pions and kaons as a function of the polar angle at a momentum of 6 GeV/c while the red points show the same quantity for charged pions and electrons at 1.2 GeV/c. The expected particle identification performance of the hpDIRC exceeds the ECCE PID goal of three standard deviation (s.d.) separation power for e/π up to 1.2 GeV/c and π/K up to 6 GeV/c for the entire polar angle range.

2.4.3 dRICH

The dual-radiator Ring Imaging Cherenkov (dRICH) detector configuration for ECCE consists of 6 identical, transversely open sectors. Each contains two radiators (aerogel and C_2F_6 gas), sharing the same outward focusing mirror and readout planes, which are instrumented with highly segmented photosensors (3 mm$\times$3 mm pixels), located outside of charged particle acceptance. The photosensor tiles are arranged on a curved surface to compensate for aberrations. Photons from a Cherenkov cone may split over two or more sectors thanks to the open geometry of the dRICH sectors.

In comparison to the YR reference detector the ECCE dRICH radial size was scaled down by 25% to fit into the envelope limited by the HCAL and moved about 40 cm closer towards the IP to maintain the original acceptance.

Figure 2.15 shows the preliminary results of the dRICH K/π separation power for three incidence angles and selected momenta. The results are obtained from the full ECCE simulation framework with the realistic magnetic field map and the conservative tracking resolution. Note that the simulated design uses a simplified flat detector plane and that the mirror curvature is not fully optimized yet. The results are in good agreement with expectations and already reach the desired 3 s.d. or more over almost the full required momentum range. Further improvement of the dRICH performance is expected once the planned AI-based geometry optimization is completed.

2.4.4 AC-LGAD-based TOF

The AC-LGAD TOF system is based on a simple p–n diode concept, where the diode is fabricated on a thin high-resistivity p-type silicon substrate. A highly-doped p–layer (the "gain" layer) is implanted under the n-type cathode. Application of a reverse bias voltage creates an intense electric field in this superficial region of the sensor to start an avalanche multiplication for the electrons. The drift of the multiplied carriers through the thin substrate generates a fast signal with a time resolution of $\sim$20–30 ps.

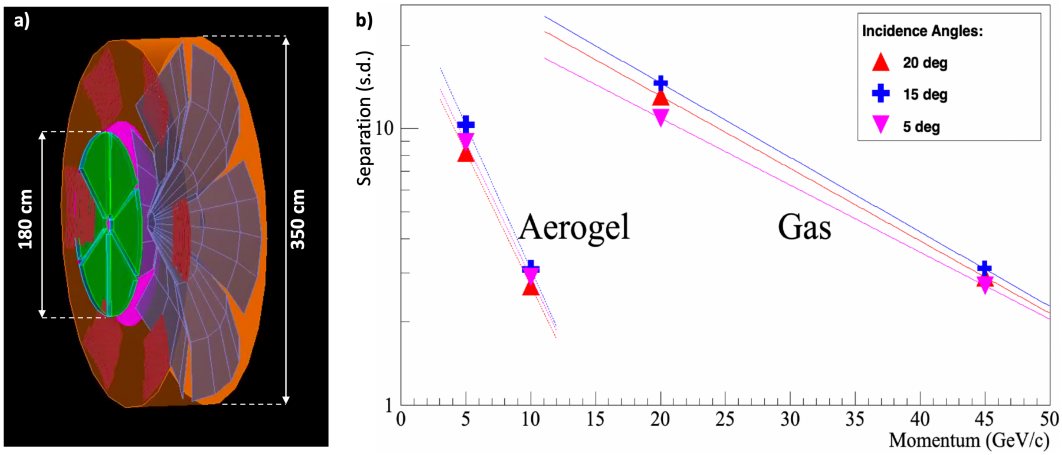

Figure 2.15: dRICH geometry (a) and expected performance (b) from the ECCE GEANT4 simulation. The K/π separation power is shown as a function of momentum for a simplified dRICH geometry (flat detector plane).

The TOF layers were placed in each section of ECCE detector and their positions were optimized to best compliment the Cherenkov detectors to cover the lowest possible particle momenta with a nearly 4π coverage, and maximize the time (25 ps) and position (pixel granularity of 0.5×2.6 mm^2) resolution. We further plan to use the DIRC timing measurement to supplement the AC-LGAD TOF measurement. This is especially useful for the $\eta \approx -1.5$ region where a gap exists in the AC-LGAD coverage and the DIRC offers excellent TOF resolution. Figure 2.16 (left) shows a visualization of the AC-LGAD geometry from the full GEANT4 simulation. Figure 2.16 (right) summarizes the performance of the TOF layers in each sector of the ECCE detector for π/K, e/π, and K/p separation.

The PID performance in terms of $1/\beta$ vs. p for the central barrel, as a benchmark, is shown in Fig. 2.17 (left) for an expected timing precision of 25 ps. The long dashed lines indicate the $\pm3\sigma$ range around mean $1/\beta$ values for each particle species. As shown, the $\pm3\sigma$ bands for pions and kaons are well separated over a momentum range of $0.1 < p < 1.3$ GeV/c, while proton identification is further extended to around 2.2 GeV/c. For electrons, clean separation from pions is achieved for $p < 0.45$ GeV/c by at least 3σ. Similar performance studies are also carried out for endcap TOFs.

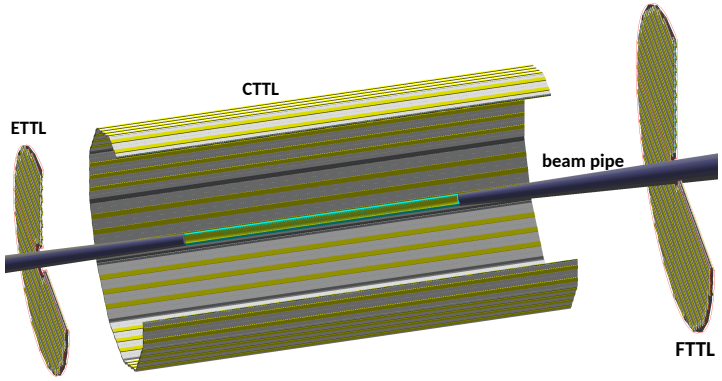

PID	ETTL	CTTL	FTTL
e/π	< 0.5	< 0.45	< 0.6
π/K	< 2.1	< 1.3	< 2.2
K/p	< 3.3	< 2.2	< 3.7

Figure 2.16: (left) A schematic view of the timing and tracking layers (TTLs) in ECCE as simulated with GEANT4. The different subdetectors are called ETTL (electron endcap), CTTL (barrel) and FTTL (hadron endcap). (right) Right: Momentum coverage in GeV/c of the ECCE Time-of-Flight detector in corresponding regions

The resolution of the start time, t_0, self-determined by the scattered electron and final-state hadrons via an iterative fitting procedure, was included in all performance studies and is shown in Fig. 2.17 (right). In addition to providing hadronic PID, the excellent position resolution of AC-LGADs TOF significantly improves the momentum resolution of high momentum particles in the very forward region.

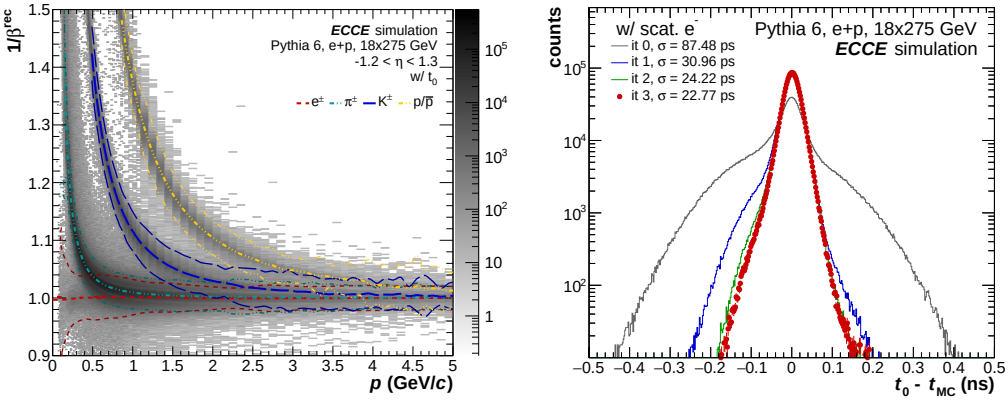

Figure 2.17: (left) Expected $1/\beta$ performance of the AC-LGADs TOF in the barrel as a function of particle momentum, assuming 25 ps time resolutions from full simulations including the start time estimates. (right) Expected start time (t_0) resolution as a function of iteration, for events where the scattered electron could be identified.

2.5 Electromagnetic and Hadronic Calorimetry

The ECCE electromagnetic calorimeter system consists of three components which allow high precision electron detection and hadron suppression in the backward, barrel, and forward directions. Hadronic calorimetry is essential for the barrel and forward endcap regions for hadron and jet reconstruction performance. Jet yields in the backward region were found to be sufficiently infrequent that hadronic calorimetry would provide little to no scientific benefit. The details for all six calorimeters envisioned for ECCE can be found in Tab. 2.5.

2.5.1 Electron Endcap EM Calorimeter (EEMC)

The EEMC is a high-resolution electromagnetic calorimeter designed for precision measurements of the energy of scattered electrons and final-state photons in the electron-going region. Its required energy resolution is driven by the need for a precise measurement of the scattered electron's energy and direction to determine the event kinematics in inclusive DIS events.

The design of the EEMC is based on an array of approximately 3000 lead tungsten crystals ($PbWO_4$) of size $2 \times 2 \times 20$ cm^3 ($\sim 22X_0$) and transverse size equal to its Moliere radius [23,24] readout by SiPMs yielding an expected energy resolution of $2\%/\sqrt{E} + 1\%$, based on prototype beam test measurements by the EEEMCAL consortium and documented in the Yellow Report [8]. Fig. 2.19 shows the EEMC performance in the full ECCE detector simulations, consistent with the measurements. The corresponding particle identification power is shown in Fig. 2.20 for distinguishing electrons and pions (left) as well separating the two photons from a neutral pion decay.

The choice of technology and overall design concept is common for all three proto-collaborations, with additional details of the development of this detector by the EEEMCal consortium summarized in the expression of interest [25]. The ECCE design only includes the $PbWO_4$ crystals due to the overall small detector radius. The EEEMCAL Consortium is planning to support one or more EIC detectors as needed and is therefore part of multiple detector proposals.

The EEMC is located inside the inner universal frame and allows to reconstruct particles with $-3.4 < \eta < -1.8$. This goes back to the difference between mechanical space and detector performance that is also documented in the Yellow Report. The material budget almost reaches η=-4, but slopes rapidly down at η=-3.7. This is because of the beam crossing and asymmetric beam pipe (see the EEEMCAL Consortium report [26]). Then the performance is only good to one crystal away which is η=-3.4 unless one squeezes to the beam pipe with a small inner calorimeter. To extend the reach of the backward EEMC to a pseudorapidity of -3.7 one can thus envision a small inner calorimeter of 208 crystals and an outer calorimeter just behind

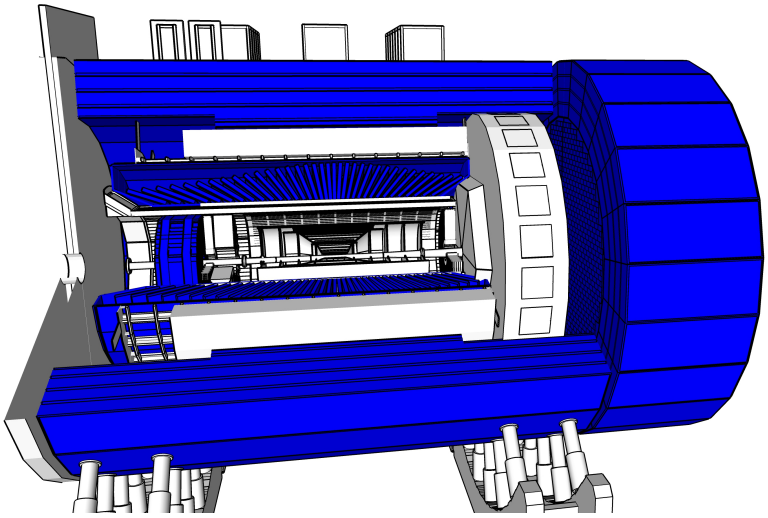

Figure 2.18: The electromagnetic and hadronic calorimeters in ECCE

Table 2.5: Specifications and properties for the electromagnetic and hadronic calorimeters from the Geant simulation. Note that d_{act} does not include readout. The acceptance of the EEMC can be achieved with a small inner calorimeter as discussed in the text. The energy resolutions for EEMC, BEMC and OHCAL are those expected from prototype tests or experiments [8, 19–21]. Further details can be found in the ECCE Tech Note [22].

	EEMC	BEMC	FEMC	IHCAL	OHCAL	LFHCAL
tower size	$2x2x20$ cm^3	$4x4x45.5$ cm^3 projective	in: $1x1x37.5$ cm^3 out: $1.6x1.6x37.5$ cm^3	$\Delta\eta \sim 0.1$ $\Delta\varphi \sim 0.1$	$\Delta\eta \sim 0.1$ $\Delta\varphi \sim 0.1$	$5x5x140$ cm^3
		projective	out: $1.6x1.6x37.5$ cm^3	$l \sim 4.5$ cm	$l \sim 88$ cm	
material	$PbWO_4$	SciGlass	Pb/Scintillator	Steel/ Scintillator	Steel/ Scintillator	Steel/W/ Scintillator
d_{abs}	-	-	1.6 mm	13 mm	in: 10.2 mm out: 14.7 mm	16 mm
d_{act}	20 cm	45.5 cm	4 mm	7 mm	7 mm	4 mm
N_{layers}	1	1	66	4	5	70
$N_{\text{towers(channel)}}$	2876	8960	19200/34416	1728	1536	9040(63280)
X/X_O	~ 22	~ 17	~ 19	~ 2	$36-48$	$65-72$
R_M	2.73 cm	3.58 cm	5.18 cm	2.48 cm	14.40 cm	21.11cm
f_{sampl}	0.914	0.970	0.220	0.059	0.035	0.040
λ/λ_0	~ 0.9	~ 1.6	~ 0.9	~ 0.2	$\sim 4-5$	$7.6-8.2$
η acceptance	$-3.7 < \eta < -1.8$	$-1.7 < \eta < 1.3$	$1.3 < \eta < 4$	$1.1 < \eta < 1.1$	$1.1 < \eta < 1.1$	$1.1 < \eta < 4$
resolution						
- energy	$2/\sqrt{E} \oplus 1$	$2.5/\sqrt{E} \oplus 1.6$	$7.1/\sqrt{E} \oplus 0.3$		$75/\sqrt{E} \oplus 14.5$	$33.2/\sqrt{E} \oplus 1.4$
- φ	~ 0.03	~ 0.05	~ 0.04		~ 0.1	~ 0.25
- η	~ 0.015	~ 0.018	~ 0.02		~ 0.06	~ 0.08

it. There is sufficient longitudinal space accommodate this, but moving the outer calorimeter back could impact the acceptance in the transition region between the EEMC and the central barrel. If possible, this arrangement would allow the outer calorimeter to be removed over the beam pipe flange for maintenance, and separate removal of the small inner calorimeter in two halves. We intend to pursue this improvement to the baseline design as a part of a detailed, integrated mechanical engineering design of the ECCE detector.

The EEEMCAL team has begun to organize activities into mechanical design, scintillator, readout, and software/simulation among the collaborating institutions. Design activities of the mechanical support structure commenced in 2021. The design is based on models of existing detectors that the team has recently constructed, in particular the Neutral Particle Spectrometer at Jefferson Lab [23]. As such, it is maturing rapidly and a document on mechanical design and integration has been completed [26].

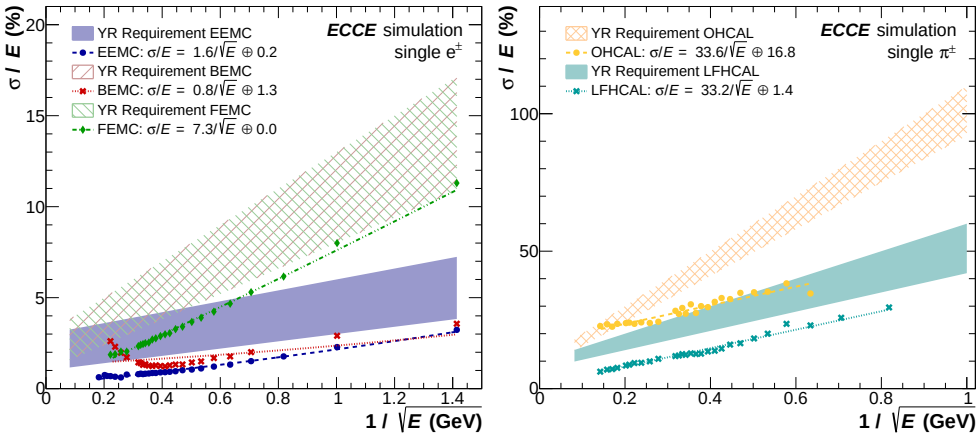

Figure 2.19: The electron (left) and pion (right) energy resolution of the electromagnetic and hadronic calorimeters, respectively, compared to the Yellow Report requirement (shaded/hashed area).

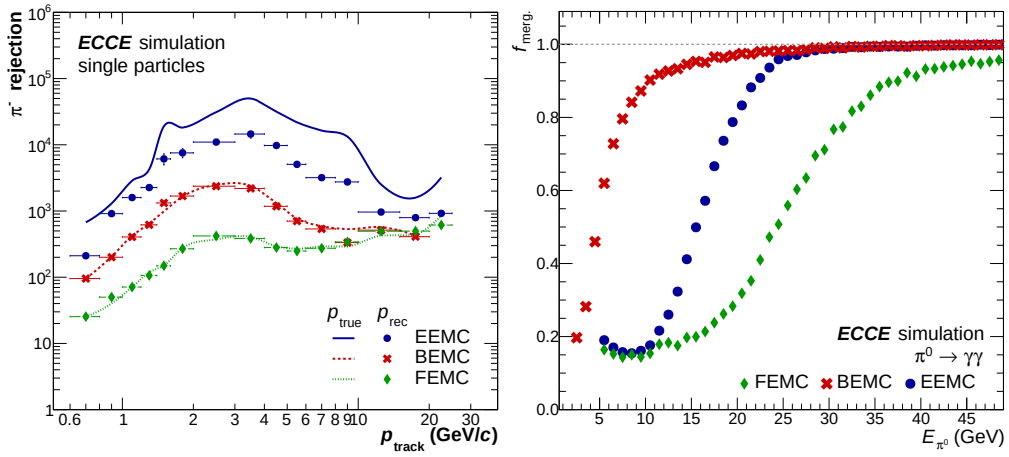

Figure 2.20: (left) Pion rejection factor for the different ECals with $E/p > 1 - 1.6\,\sigma_E/E$ and shower shape cuts applied as a function of true and reconstructed momentum. (right) Fraction of neutral pions for which the showers from their decay photons are merged into a single cluster and can not be reconstructed using an invariant-mass-based approach for the different electromagnetic calorimeters.

2.5.2 Barrel EM Calorimeter (BEMC)

The barrel electromagnetic calorimeter (BEMC) is a projective homogeneous calorimeter based on an inorganic scintillator material that produces the shower due to high Z components. This allows for a cost-effective solution that provides excellent energy resolution and sufficient e/π rejection to achieve the EIC physics, which can be seen in Fig. 2.20. Further improvements are expected by determining exactly the Birk's constant and using shower shape criteria to distinguish elongated hadronic and rounder electromagnetic showers. The reference design of the BEMC is based on an array of approximately 9000 Scintillating Glass (SciGlass) blocks of size 4 x 4 x 45.5 cm^3, plus an additional 10cm of radial readout space. SciGlass has an expected energy resolution of $2.5\%/\sqrt{E} + 1.6\%$ based on earlier measurements [19,20], comparable to $PbWO_4$ for a significantly lower cost. The energy resolution of the BEMC is shown in red in Fig. 2.19 (left) in its optimal acceptance (-1.4 $< \eta <<$ 1.1).

The development of SciGlass started with the generic detector R&D [27]. During this phase the team worked in close contact with producers of SciGlass to establish robust QA protocols at all stages of production to ensure the quality needed for the EIC. The validation of large-scale SciGlass production is now continued in the ongoing project R&D (eRD105). An initial 40 cm SciGlass bar of high quality has been produced this Fall

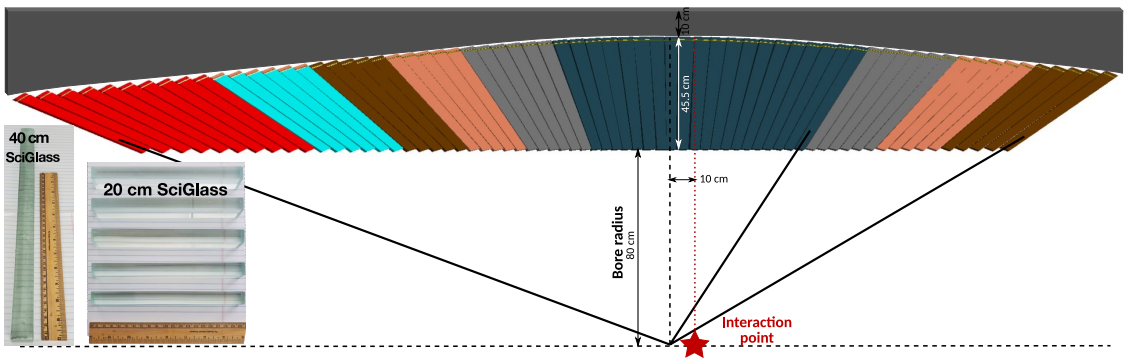

Figure 2.21: Side cut view of the barrel assembly from Geant4 illustrating the six different families of glass block sizes needed to achieve the needed projectivity. Also shown is a schematic of the support box (grey) based on the PANDA design that holds readout, cooling, and other services and mounts to the outer universal frame.

(see Fig. 2.21 bottom right), and a prototype with nine 20-cm long SciGlass bars recently saw a successful beam test at Jefferson Lab, confirming the expected energy resolution. It is expected that multiple 45-cm long SciGlass bars will be produced in the next few months.

Just as for the EEMC, the BEMC attaches to the outer universal frame. Adapting the geometry of the homogeneous barrel EM calorimeter at PANDA [28], the BEMC towers are organized in 128 blocks by ϕ slice and 70 blocks in η, which will be assembled in super modules stretching the full length in η and 8 towers in φ for installation in the universal frame. Figure 2.21 (top) shows a sketch of the BEMC illustrating the at least six different families of glass blocks needed to achieve the required projectivity in η. For comparison, PANDA uses 11 different crystal types for their barrel. The optimal number of families still has to be determined, optimizing for efficient production as well as minimal leakage between towers. Also indicated is a schematic of the support box (modeled after the PANDA barrel calorimeter) for readout and other services that mounts to the outer universal frame.

The BEMC has been designed with projectivity in η and ϕ. This requires that the tower angular deflection depends on its location in the calorimeter. Additionally, the towers have a stronger inclination at higher absolute pseudorapidities, leading to an asymmetric tapered shape of the glass blocks, which increases with $|\eta|$. Their front face is tilted such that it is facing the interaction point shifted by $z = -10$ cm and tilted 10° in the azimuthal direction, to avoid channeling between the towers. Such a projective design delivers a more uniform performance, mainly aimed at the transition regions between the barrel and forward and backward regions, as defined by the length to bore ratio of the magnet. All the towers have the same length, 45.5 cm (not including $\sim$ 10cm readout), and inner size 4 x 4 cm in the present simulation. However, the upper area sections vary from 5 to 6.6 cm in each side depending on their location.

2.5.3 Barrel Hadron Calorimeters: oHCAL and iHCAL

The energy resolution of reconstructed jets in the central barrel will be dominated by the track momentum resolution, as the jets in this region are relatively low momentum and the measurement of the energy in the hadronic calorimeter does not improve knowledge of the track momentum. For jet reconstruction, the primary use for a hadronic calorimeter in the central barrel will be to collect neutral hadronic energy and thus improve the overall knowledge of the Jet Energy Scale (JES). For this purpose, the Yellow Report indicates that a resolution of $(80-100)\%/\sqrt{E} \oplus (7-10)\%$ will be adequate. Therefore, we decided to reuse the sPHENIX Outer Hadronic Calorimeter (oHCAL), which instruments the barrel flux return steel of the BaBar solenoid to provide hadronic calorimetery with an energy resolution of $75\%/\sqrt{E} \oplus 14.5\%$, as measured in test beam. We also plan to instrument the support for the barrel electromagnetic calorimeter to provide an additional longitudinal segment of hadronic calorimetry. This will provide an Inner Hadronic Calorimeter (IHCAL) very similar in design to the sPHENIX inner HCAL. The inner HCAL is useful to monitor shower leakage from the barrel electromagnetic calorimeter as well as improve the calibration of the combined calorimeter system.

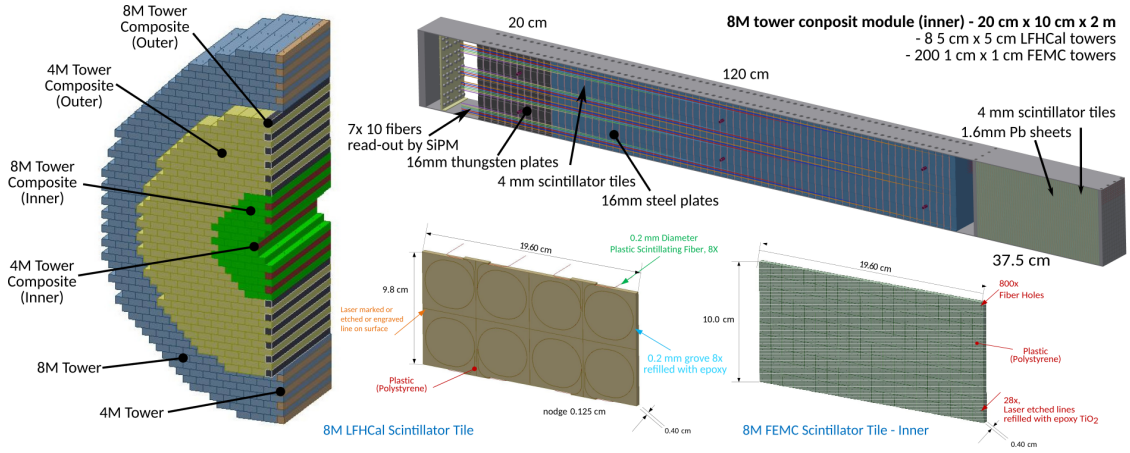

Figure 2.22: Details of the combined FEMC and LFHCal design, indicating a fully assembled half disk, the 8-tower module design and the individual scintillator tile designs for the an LFHCAL-FEMC 8M tower inner module.

The basic calorimeter concept for the iHCAL/oHCAL is a sampling calorimeter with absorber plates tilted from the radial direction. This design provides more uniform sampling in azimuth and gives some information about the longitudinal shower development. The outer HCAL uses tapered 1020 magnet steel plates which maintain a uniform gap size for the scintillating tiles. The inner HCAL will be made from stainless steel, as it sits inside the magnetic field. The Inner HCAL will not require tapered plates as studies have that tapering the shorter inner HCAL plates is not necessary, and tapering them substantially increases the machining cost. Extruded tiles of plastic scintillator with an embedded wavelength shifting fiber are interspersed between the absorber plates and read out at the outer radius with silicon photomultipliers (SiPMs). A 12 degree tilt angle relative to the radius is chosen in the outer HCAL so that a radial track from the center of the interaction region traverses at least four scintillator tiles. The inner HCAL is tilted at 36 degrees, in the opposite direction compared to the outer HCAL. Each tile has a single SiPM, and the analog signal from each tile in a tower (five for the Outer HCAL, four for the Inner HCAL) are ganged to a single preamplifier channel to form a calorimeter tower. Tiles are divided in slices of pseudorapidity so that the overall segmentation is $\Delta\eta \times \Delta\phi \sim 0.1 \times 0.1$. The Outer HCal is longitudinally symmetric around the interaction point and requires 24 tiles along the η direction. The design thus requires 12 different shapes for tiles for each longitudinal segment. The inner HCAL is extended along the backwards direction, and is comprised of 12 tiles in η in the forward direction and 15 tiles in η in the backwards direction. There are 1536 readout channels (towers) in the oHCAL and 1728 channels for the inner HCAL.

2.5.4 Hadron Endcap Electromagnetic (FEMC) and Hadronic Calorimeter (LFHCAL)

The desired performance in the forward region is governed by the jet energy resolution requirements, as well as very good energy resolution ($35\%/\sqrt{E}$ to reach the desired resolution in δx) for the physics processes connected to the origin of mass. Additionally, an excellent position resolution in particular within the ECal is required for PID within the jet. Within this region a higher particle density is expected than in the central barrel, supporting the need for excellent position an energy resolution in both calorimeters. Both detector systems need to be able to handle the expected energies of incoming particles up to 150 GeV. Due to the asymmetric collision system, these calorimeters are therefore focused strongly on high energetic particle shower containment while still providing good energy resolution at low energies.

We envision the forward calorimeter system as an integrated ECal and HCal, where the installation units, where appropriate, are constructed in a common casing. These so-called modules will consist of an electromagnetic calorimeter segment in the front which is part of the forward EMCal (FEMC) followed by a hadronic calorimeter segment which is part of the longitudinally separated HCal (LFHCal). In between these segments a read-out section is foreseen for the ECal. The modules of up to four different sizes will be

installed in half shells surrounding the beam pipe, which are movable on steel trolleys to give access to the inner detectors in the barrel in the hadron going direction. This integrated E- and HCal design reduces the dead material in the detector acceptance and allows for an easier installation in the experimental hall.

The forward ECal (FEMC) will be a Pb-Scintillator shashlik calorimeter. It is placed after the tracking and particle identification detectors and made up of two half disks with a radius of about 1.83m. The calorimeter is based on the lead-scintillator "shashlik" calorimeter designs already utilized for ALICE, STAR and PHENIX. However, it employs more modern techniques for the readout as well as scintillation tile separation. The towers were designed to be smaller than the Moliere-radius in order to allow for a further shower separation at high rapidity.

The towers have an active depth of 37.5 cm with and consist out of 66 layer of 0.16 cm Pb sheets and 0.4 cm scintillator material, as can be seen in Tab. 2.5. Due to the high occupancy of the detector at large pseudorapities and the collimation of the particles in this area in physical space, the tower size will vary depending on its radial position with respect to the beam axis. Towers which are close to the beam pipe ($R < 0.8$ m) will have a active tower size of 1 cm$\times$1 cm$\times$37.5 cm. For the outer radii this granularity is not necessary and thus the size is increased to 1.65 cm$\times$1.65 cm$\times$37.5 cm. In order to collect the light produced in the scintillator tiles, each scintillator and Pb-plate is pierced by four 0.2 mm-wavelength shifting fibers. These fibers are used to collect the light generated in the scintillators across all 66 layers. All four fibers are read out together by one silicon photomultiplier (SiPM). The FEMC is constructed with modules size of at least 5 cm$\times$5 cm$\times$37.5 cm (1M module) up to 10 cm$\times$20 cm$\times$37.5 cm (8M modules) aligning with the module sizes of the hadronic calorimeter. In order to separate the light produced in different segments of the 8M-tile a gap between the 1 cm$\times$1 cm tower tiles is created by edging into the scintillator using a laser. These 0.37 mm deep gaps are then refilled with a mixture of epoxy and titanium-oxide in order to reduce the light cross talk among different towers. Depending on their radial position this leads to either 72 or 200 read-out towers in one 8M modules.

The longitudinally segmented forward HCal (LFHCAL) is a Steel-Tungsten-Scintillator calorimeter adapted from the PSD calorimeter for the NA61/SHINE experiment [29], but it has been severely modified to meet the desired physics performance laid out in the Yellow Report. It is made up of two half disks with a radius of about 2.6 m.

The LFHCAL towers have an active depth of 1.4 m with an additional space for the readout of about 20–30 cm depending on their radial position, as seen in Table 2.5. Each tower consists out of 70 layers of 1.6 cm absorber and 0.4 cm scintillator material. For the first 60 layers the absorber material is steel, while the last 10 layers serve as tail catcher and are thus made out of tungsten to maximize the interaction length within the available space. The front face of the tower is 5 cm$\times$5 cm.

In each scintillator a loop of wavelength shifting fiber is embedded, as can be seen in Fig. 2.22 (middle). Ten consecutive fibers in a tower are read out together by one Silicon photo multiplier, leading to seven samples per tower. The towers are constructed in units of 8-,4-, 2- and 1-tower modules to ease the construction and reduce the dead space between the towers and the active detection area. Similar as for the FEMC the scintillator tiles in the larger modules are made out of one piece and then separated by a gaps refilled with epoxy and titanium oxide to reduce light cross-talk among the different readout towers. For the same purpose the wavelength shifting fibers running on the sides of the towers are grouped early on according to their readout unit and separated by thin plastic pieces over the full length. They terminate in one common light collector which is directly attached to a SiPM. The entire detector will consist of 63280 readout channels grouped in 9040 read-out towers.

The majority of the calorimeter will be built out of 8-tower modules ($\sim$1091) which are stacked in the support frame using a lego-like system for alignment and internal stability, as can be seen in Fig. 2.22 (left). The remaining module sizes are necessary to fill the gaps at the edges and around the beam pipe to allow for maximum coverage. The absorber plates in the modules are held to their frame by four screws each. To leave space for the read-out fibers, the steel and scintillator plates are not entirely square but equipped with 1.25 mm grooves, creating the fiber channels on the sides. These fiber channels are covered by 0.5 mm thin steel plates for protection after module installation and testing, in order to protect the fragile fibers. For internal alignment we rely on the usage of 1–2 cm steel pins in the LFHCal part which are directly anchored

to the steel or tungsten absorber plates. Afterwards the modules will be self-supporting within the outer support frame. The steel in the LFHCAL serves as flux return for the BaBar magnet, thus a significant force is exerted on the calorimeter, which needs to be compensated for by the frame and internal support structure. The achieved energy resolution accoding to the simulations for both calorimeters can be found in Fig. 2.19. The required resolutions can be met in both cases and further improvements can be expected using machine learning for the clusterization which proves challenging in this direction. The excellent position resolution in the FEMC should in addition allow the effective separation of electrons and pions as well neutral pion decays, as seen in Fig. 2.20. The projected performance meets the physics requirements by the eA diffractive J/ψ production and the u-Channel DVCS, as well as meson (pion/kaon) structure function measurements through the Sullivan process.

2.6 Far-Forward/Far-Backward Detectors

A schematic of the far-forward detectors is shown in Figure 2.23 and include the B0 spectrometer, off-momentum trackers, Roman Pots and ZDC (see Table 2.6 for position and dimensions). The far-backward region consists of two detector systems (low-Q^2 tagger and luminosity monitor). All far-forward/far-backward detectors are required for the EIC physics as described in the Yellow Report. The following describes their setup and performance. For further details, see Ref. [30].

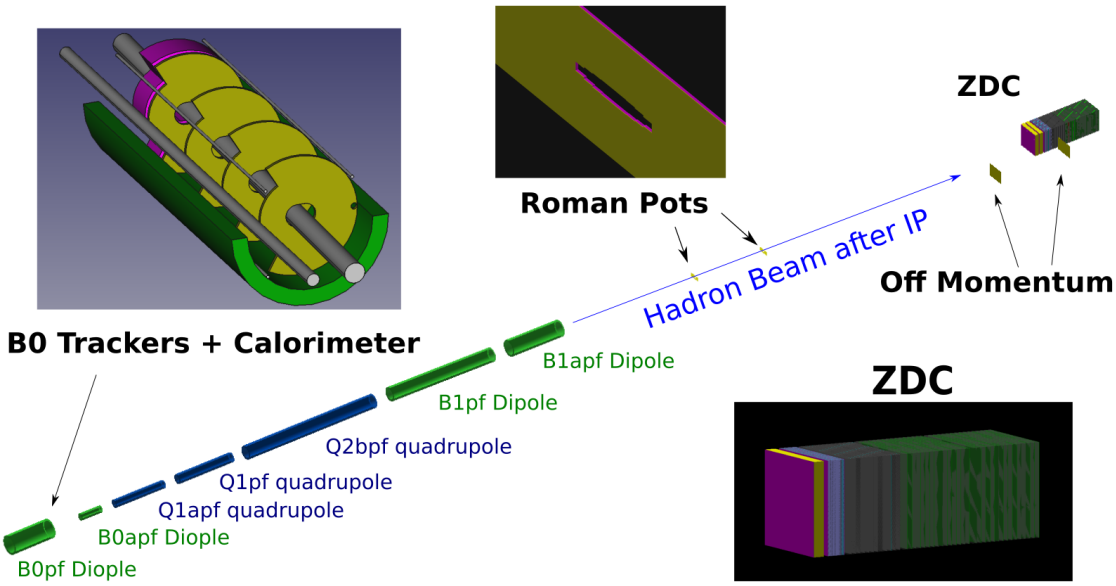

Figure 2.23: The layout of the EIC Far-Forward region.

2.6.1 B0 Detector

The B0 spectrometer is located inside B0pf dipole magnet. Its main use is to measure forward going hadrons and photons for exclusive reactions. The B0 acceptance is defined by the B0pf magnet. Its design is challenging due to the two beam pipes (electron and hadron) that it needs to accommodate and the fact that they are not parallel to each other due to the 0.025 mrad IP6 crossing angle. Moreover, the service access to the detectors inside of the dipole is only possible from the IP side, where the distance between the beam pipes is narrowest. Following these limitations the B0 detector require using compact and efficient detection technologies.

Our design uses four AC-LGAD tracker layers with 30 cm spacing between each layer. They will provide charged particle detection for $6 < \theta < 22.5$ mrad. The use of AC-LGAD sensors will allow good position

Table 2.6: Summary of far-forward detector locations and angular acceptances for charged hadrons, neutrons, photons, and light nuclei or nuclear fragments. In some cases, the angular acceptance is not uniform in ϕ, as noted in the table. For the three silicon detectors (Roman Pots, Off-Momentum Detectors, and B0 spectrometer) a depth is not given, just the 2D size of the silicon plane. For the Roman Pots and Off-Momentum Detectors, the simulations have two silicon planes spaced 2m apart, while the B0 detectors have four silicon planes evenly spaced along the first 1.0 m length of the B0pf dipole magnet bore. The planes have a "hole" for the passage of the hadron beam pipe that has a radius of 3.2 cm.

Detector	(x,z) Position [m]	Dimensions	θ [mrad]	Notes
ZDC	(-0.96, 37.5)	(60cm, 60cm, 1.62m)	$\theta < 5.5$	$\sim$4.0 mrad at $\phi = \pi$
Roman Pots (2 stations)	(-0.83, 26.0) (-0.92, 28.0)	(30cm, 10cm)	$0.0 < \theta < 5.5$	$10\,\sigma$ cut.
Off-Momentum Detector	(-1.62, 34.5), (-1.71, 36.5)	(50cm, 35cm)	$0.0 < \theta < 5.0$	$0.4 < x_L < 0.6$
B0 Trackers and Calorimeter	(x = -0.15, $5.8 <$ z < 7.0)	(32cm, 38m)	$6.0 < \theta < 22.5$	$\sim$20 mrad at ϕ=0

and timing resolutions. The AC-LGAD sensor will have a 3.2x3.2 cm^2 area, with four dedicated ASIC units on each sensor. In addition, a $PbWO_4$ calorimeter will be positioned behind the fourth tracking layer at 683 cm from the IP. Using the $PbWO_4$ in the B0 calorimeter will increase the detection fraction of the two decayed γs from the u-Channel π_0 production from 40% to 100%, and enable measurements of u-Channel DVCS events which without it will be swamped by the π^0 events with single γ detected. The calorimeter is constructed from 10 cm long 2x2 cm^2 $PbWO_4$ crystals and positioned to leave 7 cm for the readout system. Both trackers and Calorimeter has oval holes in the center to accommodate the hadron beam pipe, and a cutaway in the side to accommodate the electron beam and allow installation and service of the detector system (see Fig. 2.23).

Figure 2.24 (left) shows the simulated momentum and its resolution $\sigma[\Delta p/p]$ as a function of truth momentum. It is below 5% for the studied kinematic region. The effect of the presence of dead material (2mm of Cu after each Si plane) layers on the momentum resolution is also shown and estimated to degrade the resolution by 2% uniformly as a function of p. The photon energy reconstructed in the B0 calorimeter and its resolution are shown in Fig 2.24 (right) for photons originating in the interaction vertex with pseudorapidity $4 < \eta < 6$ and energy $0 < E_\gamma < 60$ GeV. It is found to be below 7% for the studied kinematic region. In general about 60% of the energy is reconstructed within a 2x2 crystal grid with some dips in efficiency at low E_γ and high η.

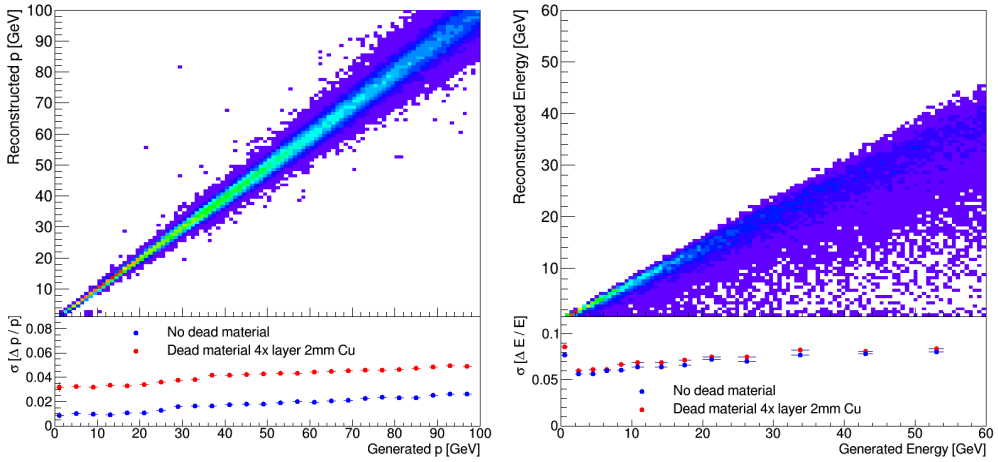

Figure 2.24: (left) Reconstructed momentum and its resolution for μ^- tracks found in the B0 tracker; (right) reconstructed energy of photons and its resolution in the B0 calorimeter.

2.6.2 Roman Pots

Diffractive processes such as deeply virtual Compton scattering will produce protons with high energy and small p_T with only a small separation from the hadron beam. The Roman Pots are designed to detect such particles. They will consist of two double-layer 25x12 cm^2 AC-LGAD stations, located inside the beam line 26 and 28 m downstream the interaction point and 10σ from the main beam. This technology will provide the necessary position and timing resolution for a precise measurement with minimized background.

The vacuum environment will require special cooling. We will use heat sinks made of metal foam through which compressed air will flow. Such cooling systems are already in use at the LHC.

2.6.3 Off-momentum Detectors

Off-momentum detectors complement the Roman Pots by measuring charged particles that have a smaller magnetic rigidity than the main hadron beam. Such particles will be bent outside the beam pipe. The detectors consist of tracking planes based on AC-LGAD sensors.

Good timing resolution on the order of 10s facilitates the rejection of pileup and beam related background, since particles that do not come directly from the interaction point will have a different flight path than the particles of interest. Such techniques have been used extensively by the CMS Precision Proton Spectrometer and the ATLAS Forward Proton Group at the LHC.

2.6.4 Zero Degree Calorimeter (ZDC)

The size of the ECCE ZDC is 60 cm$\times$60 cm$\times$162 cm, and the weight is greater than 6t. As shown in Fig. 2.23, the ZDC consists of $PbWO_4$ crystal layer, W/Si layer, Pb/Si layer and Pb/Scintillator layer.

The estimated energy resolution for high energy photons is well below the required value. For the low energy photons, estimated resolution for 100 MeV photons using 5% smearing reaches 20%, which is is still acceptable. The neutron energy resolution is consistent with and even smaller than the Yellow Report required value of $50\%/\sqrt{E} + 5\%$. For 40 GeV and 20 GeV photons, the position resolution is estimated as 1.1 mm and 1.5 mm respectively. On the crystal layer, the cluster finding efficiency is $> 95\%$ for both 20 GeV photons and 100 MeV photons with the seed energy requirement of 15 MeV for the clustering.

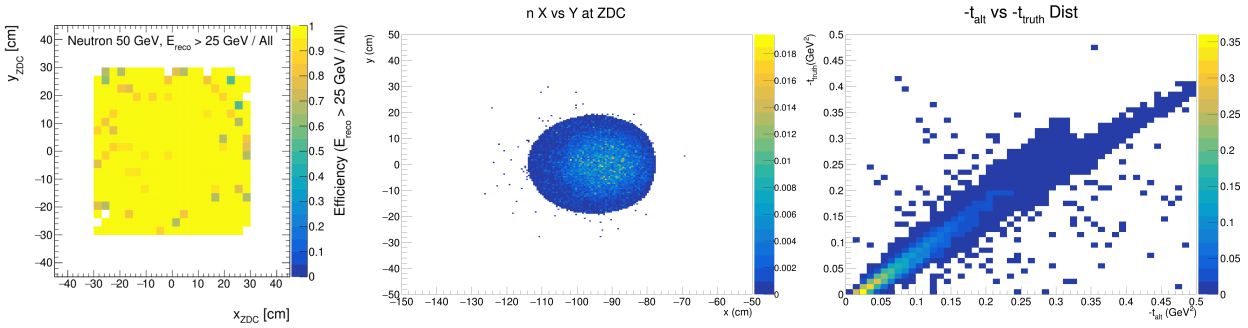

Figure 2.25: (left) ZDC detection efficiency for neutrons in its local coordinate system. (middle) Detection distribution of neutron hits in the ZDC for meson structure function processes without the beam pipe blocking contribution. z-axis reflects the normalized yield. (right) Reconstructed t versus true t, where t is reconstructed as from the baryon information, $t_{alt} = (p_p - p_n)^2$, which is reliable with a resolution of < 0.025 GeV^2.

While the ZDC is used for a variety of measurements in ECCE, we evaluate its performance here using simulations of meson structure function measurements that represent a key performance driver for this detector. In these reactions, neutrons from the Sullivan process carry 80-98% of the proton beam momentum and are detected at far-forward angles in the ZDC. The detection fraction for neutrons (t resolution) is 59% (0.019 GeV^2) at the lowest, 5 on 41, and 100% (0.005-0.007 GeV^2) at the higher energy combinations. Due to the large size and high inherent ZDC detection efficiency (Fig. 2.25 (left)), the ECCE detection efficiency

for these events is quite high, $\sim 80\%$, and nearly independent of Q^2. A density plot of event distribution is shown in the left panel of Fig. 2.25. The detection efficiency is highest for events with small $-t < 0.15$ GeV^2, which are needed for measurements such as the pion form factor, and decreases rapidly with $-t$. The t-range of optimal acceptance is dictated by the size of the ZDC, as the energetic neutrons from higher $-t$ events are emitted at an angle larger than the ZDC acceptance.

We further find the ZDC to offer excellent reconstruction of t. Compared with the t reconstruction from the measurement of the π^+ and e' tracks, the ZDC's baryon measurement is significantly more reliable, in agreement with EIC YR studies. Due to the excellent position resolution of the ZDC, the neutron track momentum is reconstructed to within 1% of the "true" momentum.With this information, t is reconstructed from the neutron track in a manner that reproduces the true value very closely, see Fig. 2.25 (right). Such a reliable reconstruction of t is essential for many processes such as the pion form factor measurement, where the rapid fall off of the cross section needs to be measured to confirm the dominance of the Sullivan mechanism. The high quality ZDC proposed by ECCE is clearly of paramount importance to the feasibility of such measurements.

2.6.5 Low-Q^2 Tagger

The low Q^2-tagger will facilitate measurement of reactions with small cross sections, e.g. timelike Compton scattering. Measuring the scatted electron will allow the s dependence to be measured as well as giving some measure of the production four momentum transfer, or t. When coupled with proton detection in the far forward region there will be the possibility of applying exclusivity cuts.

The low-Q^2 Tagger consists of two stations, located 24 m and 37 m from the interaction point. Each station includes a double layered AC-LGAD tracker, followed by a $PbWO_4$ electromagnetic calorimeter. The detectors surface areas are 40.5 cm$\times$40.5 cm at 24 m and 30 cm$\times$21 cm at 37 m and their calorimeters both use 20 cm long 2 cm$\times$2 cm $PbWO_4$ crystals.

The tracking planes enable the determination of the electron scattering angle, that in turn facilitate a precise determination of Q^2. The calorimeter provides an energy measurement to complement the tracking and provide additional shower shape information to confirm that the particle really is an electron.

2.6.6 Luminosity Monitors

For the luminosity measurements, an accuracy of the order of 1% is required, or relative luminosity determination exceeding 10^{-4} precision. The latter is driven by the size of the asymmetries we want to measure. This requirement drives the utilization of several complementary approaches for both relative and absolute measurements of the luminosity, allowing us to understand and constraint the beam-size effects, synchrotron radiation, as well as systematic uncertainties. The approach we will follow is based on existing experience from HERA. The absolute luminosity is determined by correlating the total energy in the calorimeter with the number of photons. The low-Q^2 tagger can also provide key information on the relative luminosities and thus impose further constraints on the luminosity determination.

The luminosity monitor will be located along the photon zero-degree line in the far backward region and will measure bremsstrahlung photons. It uses both a dedicated calorimeter to measure direct photons, and two spectrometer arms to measure e^+e^- pairs from conversions. The direct photon calorimeter will have a size of 16 cm$\times$16 cm and will use 20cm long 2x2 cm^2 $PbWO_4$ crystals. The e^+ and e^- from photon conversions will be deflected above and below the main photon beam by a small dipole magnet before entering the spectrometer arms. Each arm includes two 8×16 cm^2 AC-LGAD tracking layers followed by a $PbWO_4$ calorimeter with a matching surface area (also made of 20cm long 2x2 cm^2 crystals). The tracking planes in the e^+/e^- arms will allow reconstructing the gamma spot to help understand and constraint beam-size effects.

2.7 Electronics and Data Acquisition

The general design of the ECCE data acquisition builds on the sPHENIX DAQ system and many of the JLAB streaming readout systems under test [30]. These systems already incorporate and demonstrate almost all concepts of the envisioned ECCE DAQ system. The ECCE DAQ system will be built around a trigger-less Streaming Readout (SRO) concept from the start.

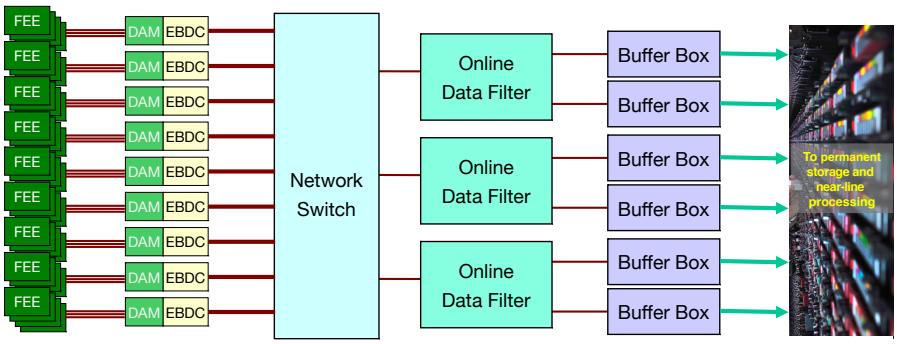

Figure 2.26: The schematic view of the ECCE Data Acquisition system. With the detector systems connecting to FEE cards from the left, the digitized data are sent to "Data Aggregation Modules" (DAM) that filter and package the data. The "Event Buffer and Data Compressor" (EBDC) nodes perform another filter, noise suppression, and clustering step on the scope of the connected detector channels, and align the hits by timing value. The data are then sent to processing nodes that perform a filtering/triggering step on the entire detector view. Data from selected crossings then get stored temporarily on large file servers ("Buffer Boxes") before being sent to long-term storage at the computing center.

As detailed in the Yellow Report [1], the Streaming Readout concept has proven superior to a classic triggered scheme in several ways. Modern readout technologies often do not follow a strict "event" paradigm in the sense that data from collider crossing n are already arriving from one front-end, while other parts can still be transmitting data from trigger n-1, n-2, or earlier crossings. In streaming mode, there is no need to wait for the completion of the data transmission from a given crossing, as the data parts are later re-assembled by their embedded clock information. This usually leads to a higher data throughput in streaming mode.

The other advantage is that classic trigger setups are always limited in their selection power because the amount of data they can sample to arrive at a trigger decision is generally much more restricted than in streaming mode, where the software- or firmware-based selection algorithms have, at least in principle, access to the data from all detector components. The processing power to increase the quality of the event selection has become cheaper every year, and this trend is expected to continue.

In a trigger-less data acquisition scheme, each channel with a signal exceeding a threshold is transferred after being labeled with a time-stamp, irregardless of the status of the other channels. The resulting data is often a waveform, or a list of fired pixel-type detector elements, or some combination of both. Subsequent processing layers reduce the amount of information by categorizing the information by time, so that eventually the detector information of one bunch crossing is together in one place. While traversing the various processing layers, data get filtered and packaged, and waveform processing and clustering algorithms are applied that further reduce the amount of data to a few key properties.

The progression of processing layers is schematically shown in Fig. 2.26. With the connections from the detector, typically fibers, coming from the left, detector-specific Front-End Electronics (FEE) cards digitize the signals, and send digital data on to the "Data Aggregation Module" (DAM). An current example of such a DAM is the ATLAS FELIX card [5].

The DAM plays a central role as it provides a common detector interface for the expected large variety of detector readout technologies that are found upstream of the DAM. While the DAM still needs to run

detector-specific firmware to receive and package the data, it provides common hardware and common APIs for the subsequent data handling, and greatly reduces the software development efforts.

The "Event Buffer and Data Compressor" (EBDC) nodes, the offline data filter, and the file servers ("Buffer Boxes") shown in Fig 2.26 are Linux PCs that form the next layers of the processing chain.

The Front End Electronics including ASICs will need to be compatible with the streaming readout DAQ system plan. FEE will need to support continuous sampling modes and not require an external trigger to convert detector signals because this will introduce large unwanted DAQ deadtime. Full waveform sampling for high occupancy detectors with zero suppression and feature extraction (time & charge) will be needed for a flexible streaming readout system.

Table 2.7: PID Detector ASICs and channel counts.

PID WBS Name	Detector	ASIC	Channels
Barrel PID	hpDIRC	High Density SoC	69,632
	TOF	eRD112 development	8,600,000
Electron Endcap	mRICH	High Density SoC	65,536
	TOF	eRD112 development	920,000
Hadron Endcap	dRICH	MAROC3	5,376
	TOF	eRD112 development	1,840,000
Far-Forward Detectors	Roman Pots	eRD112 development	524,288
	B0 Detector	eRD112 development	2.6M
	Off-Momentum Detectors	eRD112 development	1.8M
Far-Backward Detectors	Low-Q^2 Tagger	eRD112 development	4.6M
	Luminosity Monitor	eRD112 development	268,441

ASIC devices have been carefully evaluated for each of the ECCE experiment detector systems and are listed for the PID detectors in Table 2.7. High channel counts for the hpDIRC and mRICH detectors have based their readout on the High Density System-on-a-Chip (HDSoC) ASIC that is commercially produced by Nalu Scientific. The HDSoC has 64 channels and a very high bandwidth sampling ADC for waveform capture and feature extraction modes. This ASIC will support the streaming readout model. The dRICH detector is planning to use the MAROC3 ASIC which is a 64-channel device that interfaces directly to a 64 pixel maPMT device. Supporting electronics to configure the MAROC3 and provide streaming data has been in use at Jefferson Lab for the CLAS12 RICH detector for several years and is a mature technology and the MAROC3 device is now commercially available. The 64-channel SAMPA amplifier and digitizer ASIC is strongly considered for the μRWELL tracking detectors and is a very good example of an ASIC that will operate within the requirements of a streaming readout front end.

AC-Low Gain Avalanche Diodes (AC-LGAD) sensors planned for the Time-Of-Flight PID detector system, where the channel counts are very dense, as well as the far-forward detectors. Development of front-end electronics, particularly ASIC chips, for AC-LGAD readout is part of the eRD112 project for targeted EIC detector R&D. The strategy is to base designs on the ATLAS ALTIROC (130 nm) and CMS ETROC (65 nm) designs as a starting point, and reduce the pixel granularity and timing jitter to meet the EIC requirements. Specifically, the IJCLab (Orsay)/ OMEGA (IN2P3-École Polytechnique) group on the eRD112 team is a main developer of the ATLAS ALTIROC, and will play the lead role at the initial stage of ASIC development. A preliminary 130 nm ASIC design with a pitch size of 0.5 mm$\times$0.5 mm has been achieved as a stepping stone, that meets the requirements set by the EIC Roman Pot, B0 detector, and Off-Momentum detector. Future

development will focus on further improving the timing jitter and scaling up to meet the requirements of the large-scale TOF system.

The calorimeter readout in ECCE will make use of a common digitizer design for all calorimeter systems. The development will start with the existing 64-channel, 14-bit ADCs running at six times the RHIC bunch crossing frequency of just below 10 MHz, at about 60 MHz designed for the sPHENIX calorimeters. ECCE will have a common digitizer design for all calorimeters, although the form factors may differ depending on the detector implementation. It is likely that the sampling frequency will be higher based on the detector requirements. The ECCE calorimeter subsystem includes a very high channel count, however no custom ASIC development is considered because the existing sPHENIX 64-channel 14-bit ADC design is proven and reduces the number of separate electronics designs that need to be developed, verified, and maintained throughout the lifetime of the experiment.

2.8 Computing plan

The ECCE consortium plans to deploy a federated computing model for the EIC, where multiple facilities are used. A similar strategy has been successfully deployed by the LHC in the form of the Worldwide LHC Computing Grid (WLCG) [31]. ECCE has developed a tiered "Butterfly" model for EIC computing as shown in Figure 2.27 [32]. In this model, both compute and storage resources are distributed with data storage focused at the Echelon 1 sites. This means access to data by users will be performed by connecting Echelon 3 sites directly to Echelon 1 sites. The Echelon 1 sites will themselves provide significant compute capability, but will also farm out large campaigns to Echelon 2 sites, taking advantage of the diverse computing resources available at collaborating institutions.

We have adopted a fixed-latency offline computing model where both the final calibration and reconstruction of raw data occur within 2-3 weeks of acquisition [32] with resource requirements shown in Table 2.8. During this period, raw data will be buffered on disk at all of the Echelon 1 sites, along with permanent archival copies on tapes. Final calibration will be performed semi-automatically including accumulating sufficient data for tracker alignment and energy scale calibration of the calorimeters. The ECCE computing team is also pioneering the application of state-of-the-art AI/ML algorithms in detector optimization [15, 33], simulation, and PID [34], as well as real-time reconstruction in streaming readout [35,36], data reduction [37], and signal processing [38]. AI/ML will continue to play an integral and essential role in the ECCE online and offline computing. After calibration, data processing will be released to multiple sites including HTC facilities at both Echelon 1 and 2 sites as in Fig. 2.27. We expect that the produced simulation sample will focus on 10% of the EIC collision cross-section that is directly relevant for the signal and background of the core ECCE physics program. These events will be simulated to $O(10)$ times the statistics in real data to constrain systematic uncertainty from the simulated sample to be much smaller than the data statistical uncertainty. The projected simulation resources are equivalent to the needs shown in the data reconstruction as in Table 2.8.

During the development of this proposal, a detailed detector model was simulated and reconstructed taking advantage of years of ongoing development and validation with the Fun4All-EIC/sPHENIX software [16,39]. Fun4All was determined to be the best software stack for the ECCE proposal studies, for expediency, reliability and its familiarity within the software team. Software is constantly evolving and choices will be re-evaluated in the coming months to ensure that over the next decade the ECCE software will incorporate the most advanced framework and packages with the aim of delivering a high performance, user-friendly, and reliable software stack. For example, the inclusion of AI as a tool to optimize detector design [33] has been utilized within the ECCE software stack as described in Ref. [15]. Another example includes the integration of A Common Tracking Software (ACTS) package [40] as highlighted in Ref. [41], and used in preliminary ECCE tracking pattern recognition and efficiency studies.

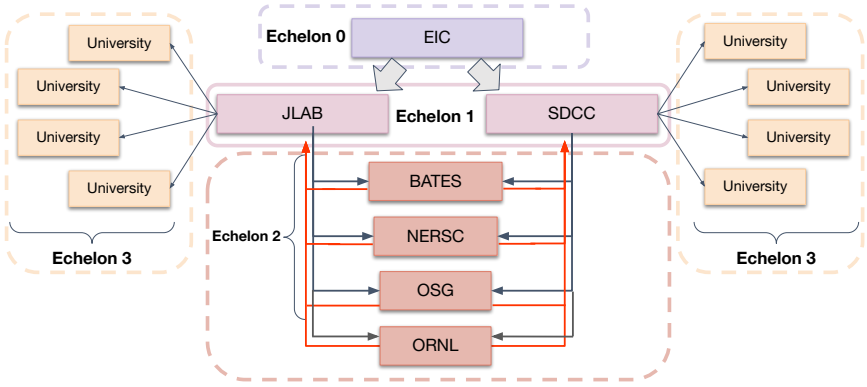

Figure 2.27: EIC Butterfly model of federated offsite computing [32]. In this model, nearly all storage is contained in echelon 1 while large portions of the raw data processing is delegated to multiple HTC/HPC facilities.

Table 2.8: Estimate of raw data storage and compute needs for first three years of ECCE, assuming ramp up to full luminosity by year 3 [32]

	ECCE Runs		
	year-1	year-2	year-3
Luminosity	10^{33}cm^{-2}s^{-1}	2×10^{33}cm^{-2}s^{-1}	10^{34}cm^{-2}s^{-1}
Weeks of Running	10	20	30
Operational efficiency	40%	50%	60%
Disk (temporary)	1.2 PB	3.0 PB	18.1 PB
Disk (permanent)	0.4 PB	2.4 PB	20.6 PB
Data Rate to Storage	6.7 Gbps	16.7 Gbps	100 Gbps
Raw Data Storage (no duplicates)	4 PB	20 PB	181 PB
Recon process time/core	5.4 s/ev	5.4 s/ev	5.4 s/ev
Streaming-unpacked event size	33kB	33kB	33kB
Number of events produced	121 billion	605 billion	5,443 billion
Recon Storage	0.4 PB	2 PB	18 PB
CPU-core hours (recon+calib)	191M core-hours	953M core-hours	8,573M core-hours
2020-cores needed to process in 30 weeks	38k	189k	1,701k

2.9 Infrastructure/Integration

The interaction region has an overall length of 9.5m. The ECCE detector extends from -4.5m to 5.0m around the origin. A total of half a meter of space between the end caps and the first interaction region magnets is reserved for vacuum pumps, valves, etc. The ECCE detector has an outer radius of 2.67 meters, which fits into the constraint given by the Rapid Cycling Synchrotron (RCS) located at 3.35m. To achieve the necessary alignment of the magnet with the electron direction the detector is rotated by 8 mrad in the horizontal plane.

The central detector features service gaps for routing out cables and services. For example, service gaps between the central barrel and the forward calorimeter assembly and the backward flux return are envisioned,

as indicated in the Sketchup mechanical model on the cover page. Additional space between the inner detectors and hpDIRC, and barrel EMCal and cryostat allow for routing cables out towards the service gaps. The beam pipe diameter increases in radius from the interaction point to the end caps[1], and thus includes several sections divided by flanges. This has to be taken into account for detector installation and servicing. For example, the diameter of the beam pipe flange at the location of the EEMC determines the configuration of the first layer of $PbWO_4$. The beam pipe would need to be disassembled for the EEMC to be inserted/extracted from its nominal position. To maximize the EEMC acceptance and allowing for easy access the ECCE detector includes an option to separate out the inner EEMC. Taking into account the beam pipe diameter, the outer endcap detectors like the forward calorimeter assembly are foreseen to follow a clam shell design.

2.10 Technology Selection, Risk and R&D

While the ECCE detector design seeks to minimize risk through strategic re-use and the selection of mature, yet state-of-the-art detector technologies, there are nevertheless risks associated with some ECCE detector technology choices. Our strategy has been to clearly identify these risks and develop an appropriate mitigation strategy, either through developing alternatives should the risks be realized or eliminating risk through an aggressive R&D program. We have developed an extensive risk registry for the ECCE proposal that includes risk impact, likelihood and mitigation strategy for a wide array of technical and cost & schedule risks. This risk registry is available as part of the ECCE supplemental materials [42].

A list of specific risks related to the ECCE technology selection includes:

- **BaBar Solenoid:** As a mitigation against the schedule risk posed by a potential problem with the BaBar solenoid developing during sPHENIX running, we plan to proceed with the initial engineering and design for a replacement magnet. A final decision to proceed with the BaBar solenoid or produce a new magnet will be taken in mid-2023 after the performance of the BaBar solenoid during the first year of sPHENIX running is reviewed by a panel of experts. The risk-mitigation decision tree is shown in Figure 2.28. Assuming a five-year construction for a new magnet, consistent with the duration of new SC magnets recently built as part of the Jefferson Lab 12-GeV Upgrade project, the ECCE schedule for detector construction and assembly would remain consistent with an early CD-4A date if procurement of a replacement magnet is determined to be necessary.

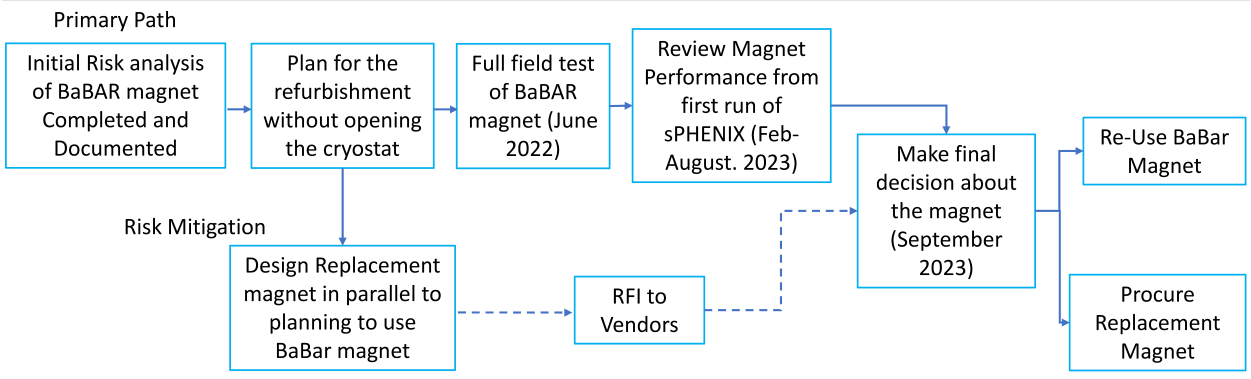

Figure 2.28: Decision tree for the risk mitigation strategy associated with the reuse of the BaBar solenoid.

- **SciGlass Calorimetry:** The use of SciGlass for electromagnetic calorimetry in the ECCE barrel offers a low-cost solution to large area electromagnetic calorimetry with excellent energy resolution. The

[1] this is necessary to allow the cone of proton/neutron and nuclear breakup particles to pass through

performance of SciGlass has been demonstrated in short (20 cm) bars. The performance validation of longer blocks is part of the ongoing EIC project R&D (eRD105) and the demonstration of large scale commercial production with high quality and uniformity is part of an ongoing Phase2 SBIR/STTR. The ECCE strategy to address the risk associated with SciGlass, if it is realized, is two-fold: if SciGlass cannot be produced on-schedule in sufficient quantities for ECCE needs, one option would be to refurbish half of the existing sPHENIX W/SciFi calorimeter to cover half of the ECCE acceptance, reducing the overall need for SciGlass. The refurbished sPHENIX calorimeter could meet required energy resolution in the forward ($\eta > 0$) acceptance, albeit with lower performance compared with SciGlass. SciGlass would still be used at the backwards direction ($\eta < 0$) where optimal energy resolution is required. If SciGlass were unavailable in sufficient quantity for the backwards region as well, the remaining half of the ECCE acceptance could be covered with PbGl towers at additional expense.

- **Cylindrical μRWell Tracking:** The ECCE experiment utilizes μRWell tracking layers in the central barrel as a low-mass, cost-effective means to provide the additional tracking points required to achieve the required momentum resolution. While cylindrical μRWell detector should be technically possible, it remains to be demonstrated that they can provide stable operation at the required 55μm resolution in a magnetic field. ECCE plans an aggressive R&D program, working with our international partners, to demonstrate the performance of cylindrical μRWell detectors and address any technical challenges that may arise.
- **AC-LGADs:** ECCE plans AC-LGAD sensors for TOF not only in the forward and backwards region but in the central barrel as well. Cylindrical detectors based on LGAD sensors have not been previously demonstrated, and AC-LGAD sensors require additional R&D to demonstrate and characterize their performance and suitability for use in both the TOF and Roman Pot detectors in ECCE. To mitigate this risk, ECCE plans a comprehensive R&D for AC-LGAD sensor and readout development, characterization and readout.
- **B0 Detector:** The current design of the B0 detector calls for a crystal calorimeter to be installed after the tracking stations in the B0 warm bore to enable studies of physics processes that require γ energy measurement such as u-channel DVCS. The installation, integration and maintenance of this detector present severe mechanical challenges due to the tight constraints in the magnet bore that will require detailed mechanical designs. If it is determined that installation of a crystal calorimeter is not feasible we will be forced to accept the loss of scope and install only the tracking planes.

In addition to detailing risks in the ECCE risk registry, we also document potential risk opportunities. We list a few representative examples here, additional information is available in the ECCE risk registry and opportunity log, both of which are available in the ECCE supplemental material.

- **Reduction of the number of hpDIRC sensors:** R&D performed for the PANDA DIRC suggests that the sensor coverage can be reduced by up to 30% without significant impact on the PID performance. A positive outcome of the simulation study and validation in test beam would allow ECCE to take advantage of this opportunity.
- **Improved ITS3 sensor yields:** Si tracker costs could be reduced if ITS3 sensor yield is higher than anticipated. We intend to take advantage of knowledge gained from ALICE ITS3 production, as well as with the foundry to optimize sensor yields.
- **hpDIRC lightguide shape:** Currently three options are being considered for the lighguide section of the bar box, which couples the narrow radiator bars to the lenses and prism. Use of one wide plate per bar box would be the most cost efficient. We intend to perform a simulation study and a test experiment with particle beams to validate this potentially cost-saving and performance-enhancing hpDIRC option for ECCE.

2.11 Detector vs. Machine Project Scope

Prior to the start of the detector proposal process, several decision were made by the project to distinguish the scope of the detector project from that of the EIC machine project:

- The accelerator/cryogenics scope will provide a cryogenic distribution can in the experimental Hall at IP6. The remaining scope in the Hall is included in the detector magnet.
- The IR and vacuum (IR magnets, beam pipes, pumps, valves, windows, etc.) are part of the accelerator/IR scope.
- The luminosity detector is included in this detector proposal and includes anything that comes behind the conversion/exit window. Up to that is assumed as accelerator scope.
- The polarimetry scope is not included in this detector proposal as it is handled external to the proposals through the across proto-collaborations polarimetry working group.
- Any required IP-6 de-installation costs are assumed to be covered as regular laboratory operations costs.
- The infrastructure scope includes items that are directly related to the ECCE specific detector proposal (support structures, cradle, specific gas handling systems, etc.).

2.12 Upgrades

The ECCE baseline detector can be augmented with additional upgrades that either enhance or expand the existing physics reach:

- **Dual-Readout Calorimetry:** The addition of a dual-readout calorimeter, replacing the FEMC and LFHCAL in the forward region would provide a significant improvement in energy resolution for hadrons in the forward region. Because the tracking momentum resolution worsens with increasing momentum while the calorimeter energy resolution improves with increasing energy, the association of tracks with high-resolution clusters in the forward calorimeters can be used to improve the knowledge of high momentum tracks (the so-called "particle-flow" approach). With a dual-readout calorimeter, the cross-over point between the tracking and calorimeter resolution would be pushed lower, enabling this improvement for a larger fraction of the tracks detected in the forward arm. Adding such improved capabilities to ECCE would improve measurements of SIDIS hadrons, TMD measurements with jets, and the ability to reconstruct event kinematics using the hadronic remnants. The Korean HEP community is very interested in deploying dual-readout calorimetry in ECCE as they develop the technology for future high-energy facilities.
- **Muon Chambers:** The addition of muon chambers to the ECCE baseline would enable the improved detection and tagging of semi-leptonic decays of heavy flavor. ECCE collaborators in Israel have expressed an interest in providing this upgrade as an in-kind contribution to ECCE. The ability to use muons for such processes as DVCS and DVMP removes an ambiguity between the produced leptons in the electron channel and the scattered electron. Such an upgrade can enhance the ability of ECCE to produce the science in the EIC white paper and NAS report.
- **Hadron Arm High-Rapidity Tracking Layer:** The addition of a small, high rapidity AC-LGAD layer ($3.0 < \eta < 3.5$) in front of the forward electromagnetic calorimeter could improve track momentum resolution for very high momentum ($p_T > 20$ GeV/c) charged tracks. It would also allow the detection of hadrons that enter the forward calorimeters from outside the acceptance of the inner tracker. This would be very beneficial for the deconvolution of overlapping clusters in the forward calorimeters as a necessary component to implementing a particle flow algorithm for the reconstruction of forward jets.
- **Backwards Hadronic Calorimeter:** While the ECCE baseline does not include a backwards hadronic calorimeter in the electron-going region, the addition of such a calorimeter could contribute to the reconstruction of event kinematics by the double-angle of Jacquet-Blondel methods at high-y, and

contribute to electron identification in the backwards region. Such a calorimeter could be based on the STAR FCS Fe/Sc hadronic calorimeter, with partial re-use of the existing STAR additional modules and new modules constructed to complete the acceptance. We have studied this extensively within ECCE, and a hadronic calorimeter in the backwards region is not required to pursue the science program in the EIC white paper or NAS report and therefore does not justify the substantial expense required at this time. However, it is possible as the EIC program matures and the EIC luminosity increases we may revisit this with a simple upgrade.

Chapter 3: ECCE Physics Performance

The precision to which physical observables can be measured depends on the combined performance of the entire ECCE detector system, in which different detector components complement, and sometimes compensate for, each other. In this section we supplement the technical performance studies of individual detector elements presented in Section 2.1 with complete simulation studies of selected physical processes utilizing the full ECCE detector.

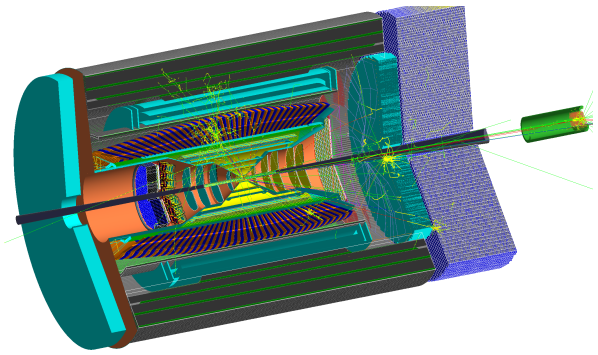

Figure 3.1: The ECCE detector implemented in GEANT4 simulations [16], visualizing an 18×275 GeV SIDIS event at $x \sim 0.07$, $Q^2 \sim 300$ $(\mathrm{GeV}/c)^2$.

These GEANT4 simulations of the full ECCE detector (which have been used to generate the event display in Fig. 3.1) include both realistic beam effects (beam crossing, divergence and 4-D vertex smearing effects), as well as the impact of realistic material effects. This is a substantial advance compared to similar studies in the Yellow Report. To study the full range of reactions in the EIC science program, ECCE has produced 740M events using 15 different event generators and 21 combinations of beam energies and species (including proton and nuclear beams). Several studies have also been performed comparing the impact of using a larger solenoid magnetic field in ECCE.

These studies are presented in detail in a set of ECCE physics notes linked from Table 1. This chapter presents a high-level summary of selected results that are significant for addressing the EIC science program, and which also test different aspects of the ECCE detector performance. Together, these studies demonstrate that ECCE is fully capable of addressing the complete EIC science program. We typically focus on presenting the simulated uncertainty (statistical plus systematic) for measuring observables such as cross-sections and asymmetries. Where possible, we also show the impact of incorporating ECCE pseudo-data into global analyses, to assess its broader impact. In other cases, by showing we achieve comparable accuracy to that assumed by previous work, we can utilize their conclusions to quantify ECCE's scientific impact. Overall we find ECCE's ability to address the EIC science program to be consistent with the Yellow Report requirements. We thus conclude that ECCE is fully able to carry out the science program outlined in the EIC White Paper and NAS report.

3.1 Origin of nucleon spin

Understanding the partonic origin of nucleon spin is one of the primary physics drivers of the EIC. Using measurements of spin-dependent inclusive deep inelastic scattering (DIS) and semi-inclusive DIS (SIDIS) reactions, in conjunction with a well developed QCD-based theoretical framework, ECCE will enable unprecedented progress toward obtaining a complete understanding of the origin of nucleon spin. Specifically, we will be using spin sum rules to decompose the total nucleon spin in terms of contributions from the spins of quarks and gluons, as well as orbital angular momenta, where each term can be related to a different measurable in ECCE.

At present, most analyses suggest that about 30% of the nucleon spin is carried by quark spins and 40% by gluon spins, with the remaining 30% originating from the orbital angular motion. However, existing data only extend down to $x \sim 0.01$, so model-dependent low-x extrapolations are needed whose uncertainties can be larger than the total spin itself. The low-x reach of the EIC will significantly improve on this situation.

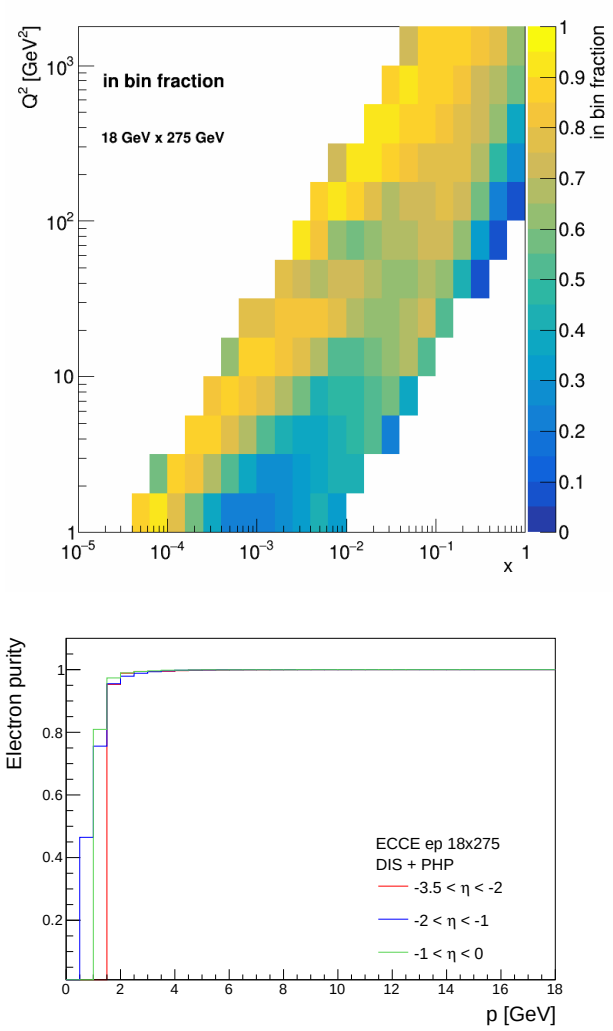

Figure 3.2: (Top) in-bin fraction for DIS kinematic Reconstruction. The reconstruction at high (low) y is done using the scattered electron tracking (double angle method). (Bottom) Estimated electron purity for inclusive DIS events ($Q^2 > 2$ GeV^2, $W^2 > 10$ GeV^2, and $0.01 < y < 0.95$) as a function of lepton momentum and different η bins. Results obtained using DJANGOH generator for DIS events and Pythia6 for photoproduction reactions and the rejection used the ECCE PID and electromagnetic calorimetry systems. Except for at very low momenta the pion contamination is below 1% which, after corrections, lead to a negligible systematic uncertainty to our measurements.

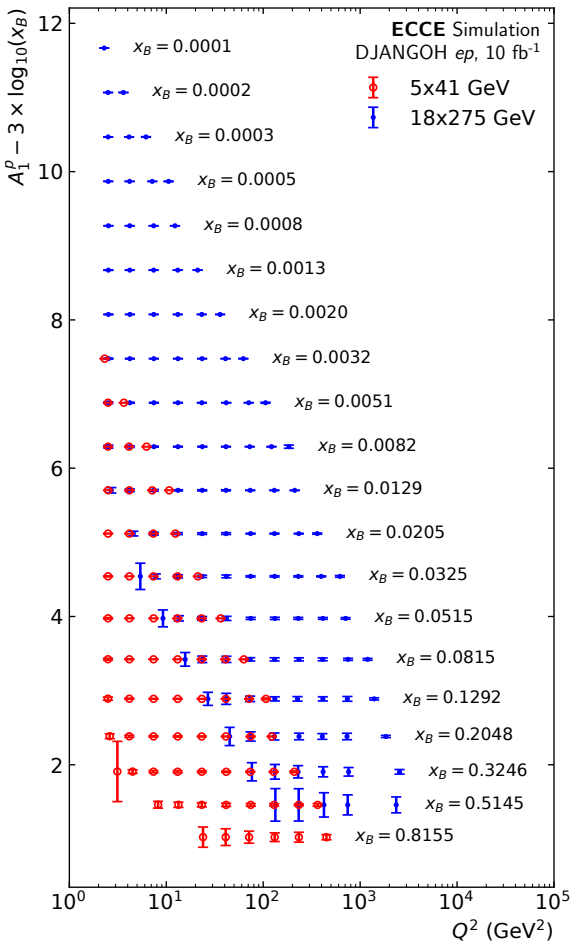

Figure 3.3: Kinematic coverage and expected precision for inclusive A_1 asymmetries from ECCE based on ep collisions at two example beam energies.

Here we present ECCE simulation studies of key measurements required to understand the origin of nucleon spin.

3.1.1 Detector requirements for Spin measurements

Spin measurements require precision polarimetry, excellent control over the relative luminosity normalization of different polarization states, precise reconstruction of the scattered lepton momentum vector (to determine DIS kinematic variables) and excellent lepton and hadron PID. These measurements thus require the ECCE tracker and electromagnetic calorimeters for DIS kinematics reconstruction and our full PID systems for obtaining a high lepton purity. In addition, SIDIS reactions require flavor tagging via hadron measurements. Spin measurements thus provide several excellent physics channels for testing the performance of the entire ECCE central detector system.

DIS is the fundamental physics process for most of the EIC physics program, requiring a precise reconstruction of its key kinematic quantities (e.g. x and Q^2). Fig. 3.2 (top) shows the fraction of DIS events reconstructed at the same $x - Q^2$ intervals in which they were generated. At high y, the best reconstruction is obtained by measuring the scattered electron track. At lower y and higher Q^2, the reconstruction of these quantities is improved by using hadronic final state measurements, via the double-angle method. Overall good reconstruction is achieved over an extended DIS phase-space (see Ref. [43] for additional details). Please note that the studies presented here utilize only the reconstructed lepton track; thus, substantial improvements can be expected, especially at high-η when including information from the excellent ECCE EM calorimetry.

Pion contamination of the scattered electron sample is another crucial issue for DIS measurements. This is especially important for measurements of parity-violating DIS reactions (see section 3.5.1 below). Excellent pion rejection can be achieved using a combination of the ECCE TOF, Cerenkov and EM calorimetry. Figure 3.2 (bottom) shows the estimated pion contamination for inclusive DIS events as a function of x for different Q^2 bins. As can be seen, the pion contamination is generally small, reaching a maximal value of $\sim 2\%$. This value is both consistent with the Yellow Report estimation and, as it can be corrected for with reasonable certainly, has minimal impact on the ECCE measurement precision.

3.1.2 Quark and Gluon Spin

The nucleon spin structure function $g_1(x)$ is defined as the charge-squared weighted sum of quark helicities. It thus provides information on the quark spin contribution to the total nucleon spin ($\Delta\Sigma = \int_x \sum_q (\Delta q(x) + \Delta\bar{q}(x))$). While the gluon spin contribution does not enter $g_1(x)$ at leading order, it is embedded in its Q^2 dependence. Therefore, an extended coverage in both x and Q^2 is needed to allow the EIC to provide information on the quark and gluon spin contribution to the total nucleon spin.

Experimentally, the quantity $g_1(x)$ is extracted from the double helicity asymmetry observable $A_1(x)$ measured in inclusive DIS. As such, the reconstruction of the DIS kinematics discussed above is expected to dominate the uncertainties on these measurements, provided the relative luminosity normalization for the different spin states is well known. Figure 3.3 shows the extracted A_1^p coverage in bins of x and Q^2 for two example beam energies. The data accuracy was estimated by accounting for both statistical uncertainties as well as lepton reconstruction unfolding effects as detailed in Ref. [44]. As the combination of the ECCE AI-optimized tracking and precision EMcal system produce a precise electron measurement, its simulated smearing effect is small and we obtain similar accuracy to that expected by the yellow-report. Therefore, we expect for the ECCE data to have similar impact on the total spin sum-rule and the required orbital angular momentum contribution as observed by early studies performed in Ref. [45] for an idealized detector.

We note for completeness that while showing proton $A_1(x)$ predictions, our studies of double-spectator proton far-forward tagging in e^3He [44, 46] show that equivalent accuracy can be obtained for the neutron; albeit with a slightly limited low-x coverage due to lower maximal center-of-mass energy achievable for e^3He collisions. These neutron data will allow us to minimize the impact of external inputs, such as the nucleon axial charge and hyperon decay constant, when extracting the diagonal combination of all quark flavors.

3.1.3 Sea quark spins

Using SIDIS measurements, where a hadron is measured in addition to the scattered electron, we can measure the A_{LL} double spin asymmetry and use fragmentation functions to obtain flavor information to further disentangle the sea quark helicity contributions.

Figure 3.4 shows the precision to which ECCE will be able to measure A_{LL} for one Q^2 bin and several x and z bins, for SIDIS measurements detecting $\pi^{\pm}$ or $K^{\pm}$ mesons and assuming 10 fb^{-1} of data. The high accuracy of the ECCE pseudodata leads to significantly improved constraints on sea quark densities, especially at low-x. This is particularly important for testing the accuracy of SU(3)$_F$ symmetry assumptions made when using hyperon decay data in global fits. These directly impact our understanding of strange quark contributions to the nucleon spin and enable obtaining a consistent analysis framework and a universal understanding of hadronic spin.

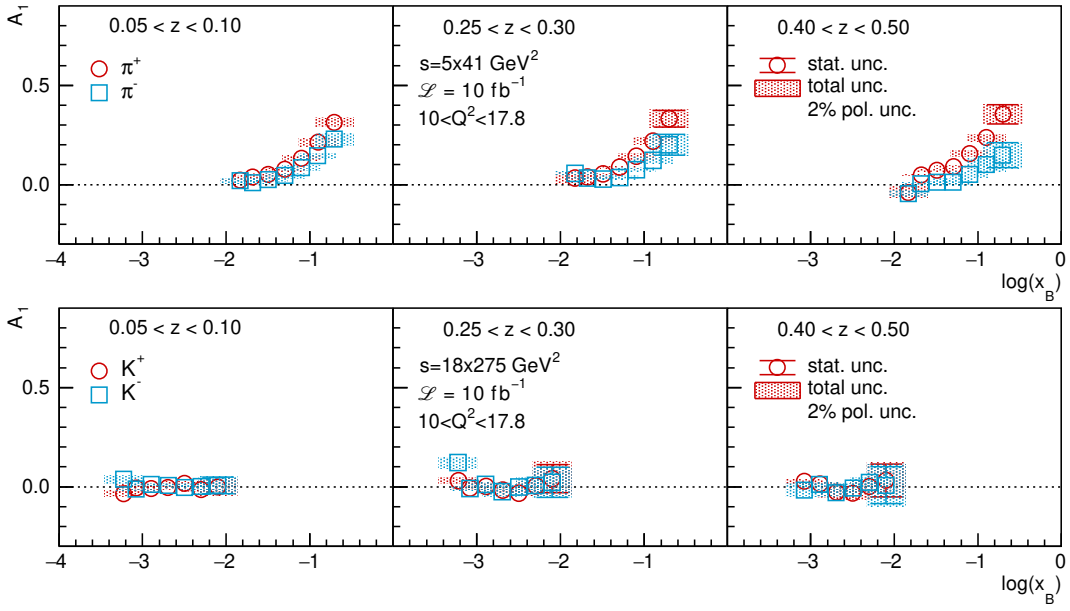

Figure 3.4: Example bins in Q^2 and z of the expected precision to be reached by ECCE for semi-inclusive A_{LL} measurements of pions and kaons at collision energies of 5 GeV on 41 Gev and 18 GeV on 275 GeV.

3.1.4 Orbital angular momentum

The total orbital angular momentum of quarks and gluons can be obtained directly from integrals over the Generalized Parton Distributions (GPDs) H and E and using the Ji sum rule [47]. These GPDs can be extracted from measurements of exclusive Deeply Virtual Compton Scattering (DVCS) processes where, apart from the scattered electron, an intact proton and a single photon are measured in the final state.

In these reactions the proton goes into the far-forward detector region, and its detection is largely determined by the acceptances of the roman pots and B0 spectrometer. The photon is detected primarily in the endcap electromagnetic calorimeter. ECCE simulations show that the ECCE far-forward design has a large proton acceptance, providing provides a large coverage in t for a wide range of x and Q^2 (i.e. comparable performance as assumed by the Yellow-Report). Similarly, the DVCS photon is well measured due to the high granularity and high resolution of the electromagnetic calorimeters. For a more detailed discussion of DVCS measurements see section 3.2.3 below.

3.1.5 Transverse spin and momentum structure

Transverse spin dependent distributions are traditionally studied by extracting Sivers [48] and Collins [49] asymmetries from SIDIS data. The Sivers functions describe a transverse momentum imbalance

of unpolarized partons within a transversely polarized nucleon. It thus provides a three-dimensional momentum image of the partons in such a nucleon. The Collins asymmetries are used to extract the quark transversity distribution, describing the distributions of transversely polarized quarks in a transversely polarized nucleon. The quark transversity distribution is one of the three leading twist distribution functions of the nucleon.

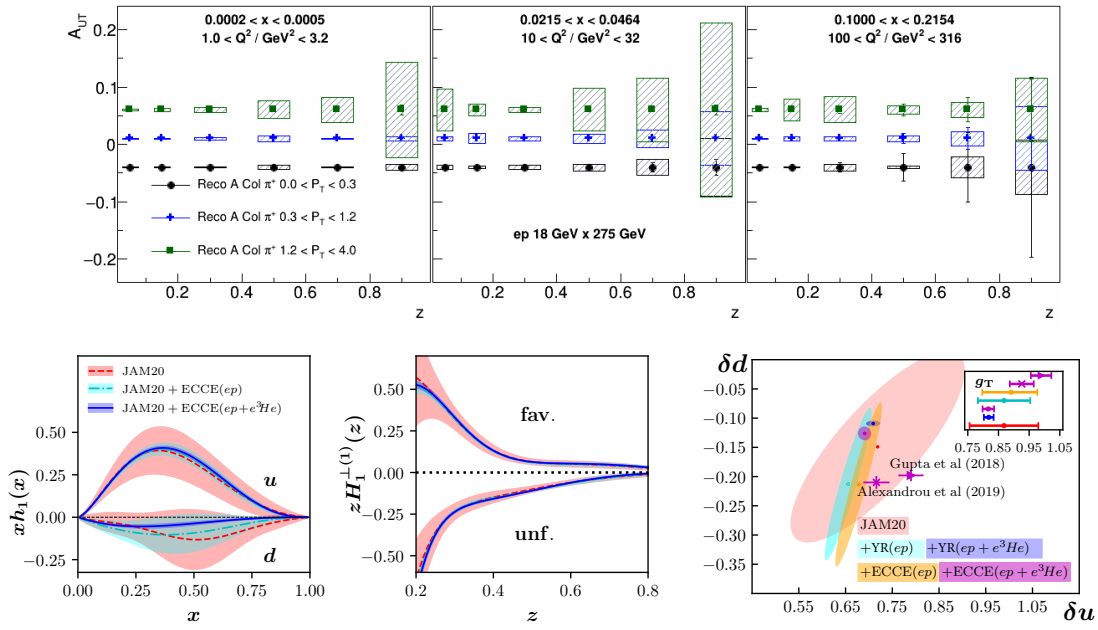

Figure 3.5: Top: Example of the expected uncertainties of the Collins asymmetries in a few selected kinematic bins as a function of z. Bottom left:Up and down quark transversity distributions as obtained at present [50], as well as when including the ECCE pseudo data. Bottom middle: Uncertainties on the favored and disfavored Collins fragmentation functions when including the ECCE pseudo-data. Bottom right: Expected uncertainties on the tensor charges in comparison of ECCE pseudo data to Yellow-Report expectations as well as existing knowledge and Lattice QCD calculations [51, 52].

ECCE's ability to study both Collins and Sivers asymmetries via measurements of single transverse spin asymmetries has been studied in SIDIS reactions [53]. Specifically, the single hadron asymmetries were obtained in azimuthal moments in combinations of the azimuthal angles of the hadron transverse momentum and transverse spin of the nucleon relative to the lepton scattering plane. As azimuthal angles are well measured by the ECCE detector, most of the smearing of these asymmetry extractions comes from the smearing in the DIS kinematic variables (x, Q^2) and the detected hadrons fractional energy (z) and transverse momentum (p_T).

The expected uncertainties of the Collins asymmetries are shown in Fig. 3.5 (top) for one beam energy, selected bins in x and Q^2 and 10 fb^{-1} of data. Fig. 3.5 (bottom) shows the expected reduction of the uncertainties of the up and down quark transversity distributions and the favored and disfavored Collins fragmentation functions. As can be seen, the impact of the ECCE pseudo data is comparable to the generic, parametrized, detector capabilities that were used in the equivalent Yellow Report studies. We note that while concentrating on Collins asymmetries, our conclusions also hold for Sivers asymmetries discussed in the 3D structure section 3.2 below.

3.2 Three-Dimensional structure of nucleons and nuclei

The EIC will enable the extraction of full tomographic images of the nucleons and nuclei and their internal constituents in the low$-x$ kinematic region. In doing so it will dramatically enhance our knowledge and

understanding of the structure of nucleons and nuclei that is, in turn, key to advancing our understanding of QCD.

3.2.1 Detector requirements for 3D structure measurements

The physics of 3D structure measurements shares many of the same requirements as the spin program described above, with the added need to reconstruct heavier mesons such as J/ψ for gluon tomography. Simulation studies demonstrate that the combined tracking and calorimetry systems of ECCE provide excellent performance for the relevant observables, with the Cerenkov and TOF systems supplying the needed electron and hadron PID [43]. However, unlike the spin program, 3D structure measurements also require measurements of protons and light nuclei in the far-forward region. Thus, this section utilizes the far-forward B0 (higher-t) and Roman Pot (lower-t) detectors, which are studied to assess the total uncertainties that can be achieved in these measurements.

3.2.2 Quark and Gluon Tomography in momentum space

Measurements of SIDIS reactions allow the nucleon's Transverse-Momentum-Dependent parton distributions (TMDs) to be probed. These functions provide a three-dimensional view of the nucleon structure in momentum space.

Figure 3.6 (top) shows the expected uncertainties of the Sivers asymmetries A_{UT} for selected bins of x and Q^2, one beam energy setting, and 10 fb^{-1} of data. Figure 3.6 (bottom) shows the expected impact of the ECCE pseudo-data on the reduction of the uncertainties of the up quark Sivers function as a function of the intrinsic transverse momentum. As can be seen, the impact is comparable to the generic, parameterized detector capabilities that were used in equivalent Yellow Report studies [1].

Extracting the gluon Sivers function is more complex, as the selection of dominating photon-gluon fusion process requires the detection of dijets or open heavy flavor pair production. Specifically, the gluon Sivers function is obtained by measuring the deviation from back-to-back topology of di-jet/heavy flavor pairs. Such deviations arise due to intrinsic transverse momentum and are strongly smeared by the fragmentation processes involved. As a result, rather small asymmetries need to be resolved. Our studies suggest that the jet [54] and heavy flavor [55] reconstruction capabilities of ECCE should provide the required high sensitivity.

3.2.3 Quark and Gluon Tomography in impact-parameter space

Complementary to TMDs, GPDs describe the position of partons in impact-parameter space as a function of their longitudinal momenta. GPDs can be accessed through high-Q^2 measurements of exclusive reactions such as DVCS and DVMP (Deep Vector Meson Production), where a meson is produced instead of a photon. A large number of exclusive processes have been studied with the ECCE detector at various beam energy configurations and their results are documented in detail in the ECCE note [56].

As mentioned, the key feature of DVCS and DVMP reactions is the detection of protons / light-nuclei in the far-forward detectors. Fig. 3.7 shows the recoil proton acceptance of the B0 spectrometer and Roman Pots for different energy configurations as function of the momentum transfer to the proton $t = (p - p')^2$. The resulting t acceptance is shown to be very wide, continuous, and extends to low-t. Such a wide coverage is essential for a precision extraction of transverse-position distributions of quarks and gluons.

The full exploration of nucleon / nuclei GPDs will require multi-dimensional measurements of the DVCS cross section in Q^2, x, t and the azimuthal angle ϕ between the lepton and hadron planes in the initial hadron rest frame. Figure 3.8 (left) shows the projected precision and coverage of DVCS cross section measurements for several beam energy configurations and in multi-dimensional bins in Q^2, x and t. Figure 3.8 (right) demonstrate the essentially hermetic reconstruction of the DVCS photon in a very wide pseudo-rapidity range.

While DVCS is sensitive to both quarks and gluons, J/ψ production in exclusive DVMP reactions is a golden channel for gluon GPDs. Figure 3.9 shows the projected cross-section measurements as a function of t for

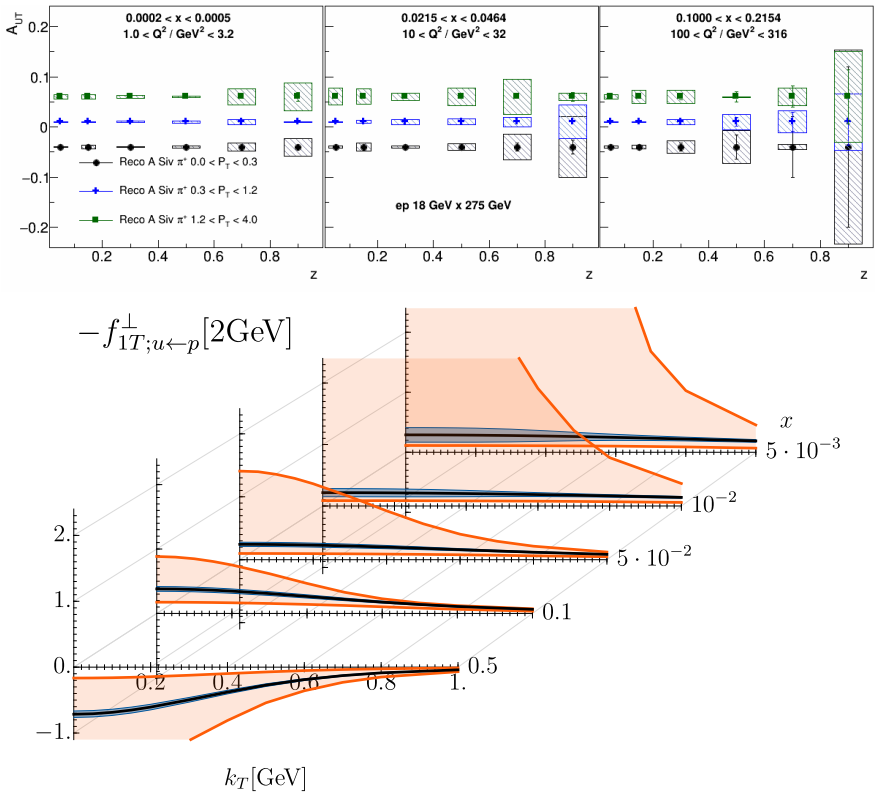

Figure 3.6: Top: Example of the expected uncertainties of the Sivers asymmetries in a few selected kinematic bins as a function of z. Bottom: Up quark Sivers function in bins of x as a function of intrinsic momentum k_t. The orange-shaded areas represent the current uncertainty, while the blue-shaded areas are the uncertainties when including the ECCE pseudo-data.

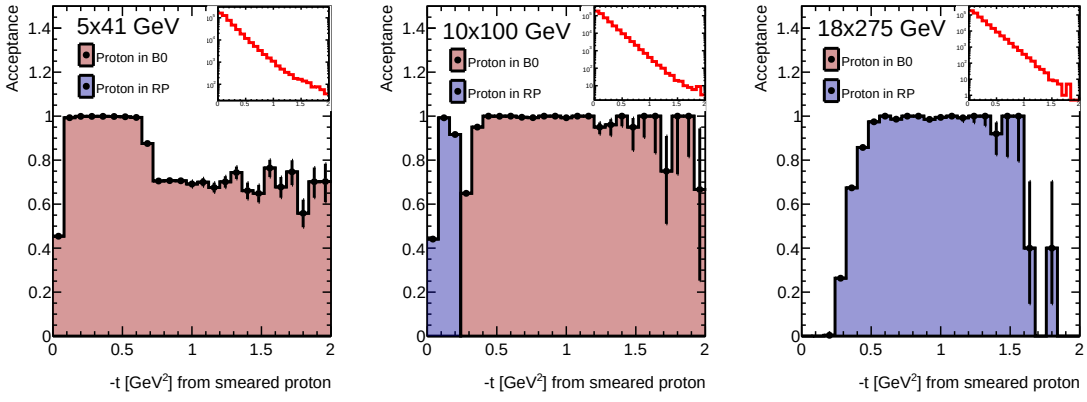

Figure 3.7: Acceptance for DVCS protons as a function of t in the far-forward detectors for different beam energy configurations. The inserts show the $t-$distributions of generated events.

different bins in $x_V = (Q^2 + M_V^2)/(2\,p\cdot q)$, the x-Bjorken equivalent scale variable for heavy mesons.

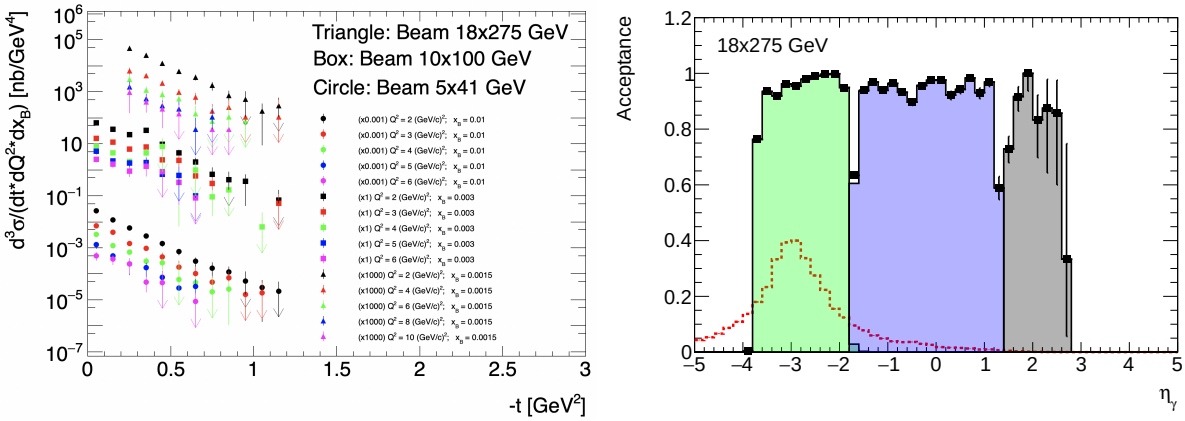

Figure 3.8: Left: Projected DVCS cross-section measurements as a function of the momentum transfer t for different bins in Q^2 and x. The assumed integrated luminosity is 10 fb^{-1} for each beam energy configuration. Right: DVCS photon acceptance in the backwards (green), barrel (blue) and forward (grey) ECALs, as a function of its pseudorapidity. The red dotted line shows the distribution of (generated) DVCS photons.

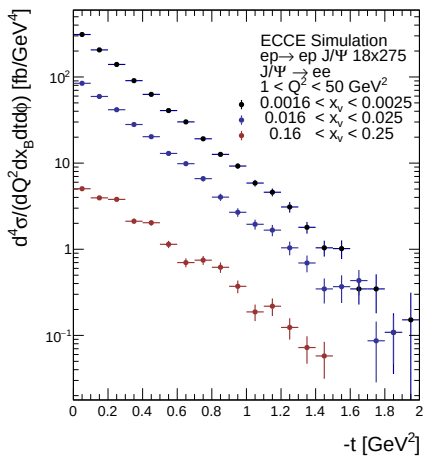

Figure 3.9: J/ψ exclusive electroproduction cross section as a function of the momentum transfer t for different bins in x_V. Integrated luminosity assumed is 10 fb^{-1}.

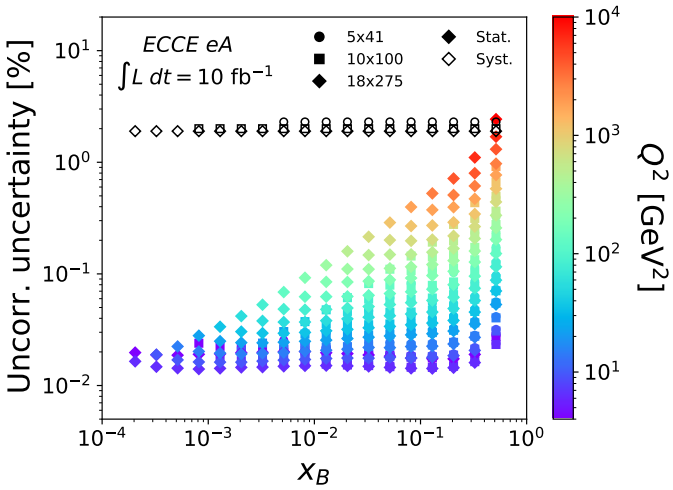

Figure 3.10: Simulated statistical and systematic accuracy for neutral current DIS off nuclei with $Q^2 > 2$ GeV^2.

3.3 Gluon structure of nuclei

Models of the partonic structure of heavy nuclei predict that due to the increased density of gluons at low-x (as compared to their density in the proton), at a high-enough interaction energy the gluons will start to recombine and lead to the phenomenon of *parton saturation* [57]. Such novel non-linear QCD dynamics fundamentally modify the standard collinear approach to QCD and the related DGLAP evolution equations [58–67]. In doing so it also predicts the existence of a new dynamically generated saturation scale $Q_s(x, A)$ in QCD that divides the dilute and dense regions of nuclei [68–70].

ECCE will provide first measurements of heavy nuclei in kinematics that is relevant for parton saturation studies. Below we describe selected processes which will provide valuable insight into the fundamental role of gluons in the structure of nuclei. The processes presented all measure heavy nuclei and include inclusive DIS, diffractive meson production, di-hadron correlations measurements and heavy flavor production.

3.3.1 Detector requirements for gluon structure of nuclei measurements

Measurements of inclusive DIS off nuclei share similar requirements to inclusive spin asymmetry measurements, but with a need to measure absolute luminosity for cross-section extraction. Similarly, di-hadron correlation measurements are very sensitive to nuclear effects in parton distributions without introducing significant requirements to the detector. The main additional detector requirements introduced by this physics thus come from measurements of heavy flavor production and (in)coherent diffractive meson production off heavy nuclei.

Measurements of heavy flavor production, e.g. via D^0 ($\bar{D^0}$) reconstruction, is sensitive to the vertex detector and the tracking system as a whole. The diffractive processes are similar to exclusive DVCS/DVMP, with the added complexity of needing to measure the cross section down to very low t, where even the Roman Pots cannot detect the recoiling nucleus. In this case t is reconstructed from the scattered electron and produced meson, requiring excellent tracking and electromagnetic calorimetry. Furthermore, to separate cases where the nucleus stayed intact (coherent) and/or breakup (incoherent), we employ the entire far-forward detection system needs as a 'veto' for particles that are produced in incoherent events. Our studies below show that ECCE can achieve excellent identification of coherent processes with suitable resolutions to perform these challenging measurements.

3.3.2 Nuclear parton densities

EIC will greatly expand on the kinematic range in x and Q^2 covered by the existing fixed target data. The inclusive DIS measurements will probe nuclei down to $x < 10^{-3}$ with a significant Q^2 coverage, see Fig. 3.10. Even with relatively low integrated luminosity, the measurement will be systematically limited with an expected precision of $\sim 2\%$ at each x, Q^2 point. This uncertainty is estimated by accounting for both unfolding and pion rejection effects and comparable to those expected by the Yellow Report. We thus expect to obtain similar improvements in the extraction of nuclear PDFs.

Using these data we will be looking for non-linear corrections in the comparison of the DGLAP evolution predictions for nuclei and free nucleons, that are a direct indicative of gluon saturation effects. By measuring a wide range of nuclei we will be able to further test the predicted growth of gluon saturation effects with decreasing x and increasing A.

The high statistics and small uncertainties will allow for additional measurements of interest. For example since charm quarks are produced in the boson-gluon fusion process, measurements of the charm structure function in nuclei will provide additional constraints to the nuclear gluon density. In addition, by running at different center-of-mass energies we expect to be able to extract the longitudinal structure function F_L that is directly sensitive to the gluon content of the target and has significant contributions from higher twist effects that go beyond the linear DGLAP evolution.

For more details on the ECCE inclusive structure functions measurement, see ECCE note [44].

3.3.3 Exclusive diffractive vector meson production on nuclei

Measuring the t dependence of exclusive diffractive vector mesons production processes provides a unique way to map the density distribution of gluon in nuclei [71,72].

As mentioned, such productions can be done both coherently and incoherently, where in the former the nucleus stays intact and the measurement is sensitive to its gluon density, while in the latter the nucleus breaks up and the measurement is sensitive to the spatial fluctuations of the gluon density [73,74]. Thus, these measurements require good t resolution and adequate separation of the coherent and incoherent signals.

We study these processes using a combination of the Sartre generator for the elementary cross section and BeAGLE for the transport calculation and nuclear break-up processes. Figure 3.11 shows the t distribution of coherent (signal) and incoherent (background) J/ψ production processes, for ePb in 18×108.4 GeV beam scenario, for $2 < Q^2 < 10\,\mathrm{GeV}^2$ and $x < 0.01$, and in the $\mu\mu$ decay mode. Since, at the low-t region of interest

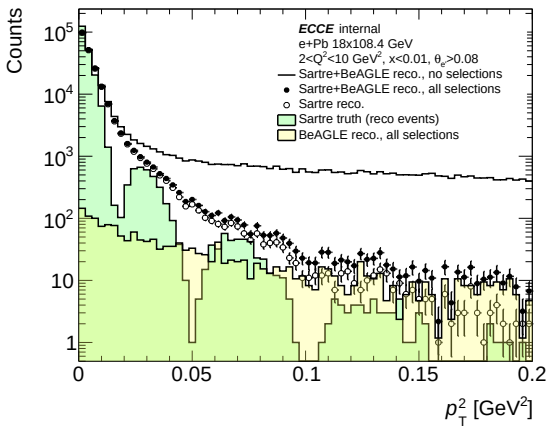

Figure 3.11: Simulation of the t dependence of the elastic diffractive J/ψ production in eA [75]. Solid: Sartre+BeAGLE simulation before selections; closed markers: reconstructed events after selection vetos; open markers: reconstruction of the coherent signal; green histogram: signal; yellow histogram: residual background.

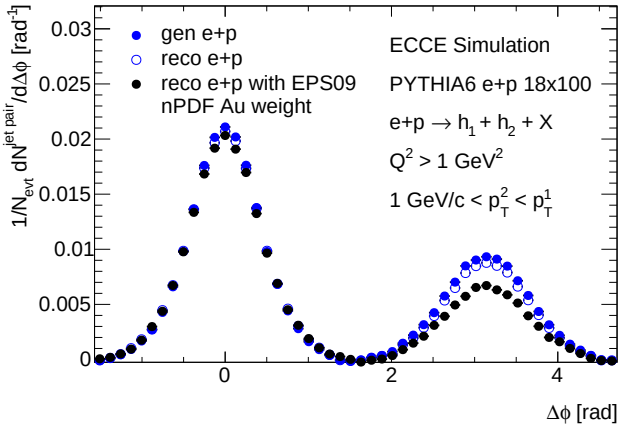

Figure 3.12: Dihadron correlations arising from dijet production in ep collisions for the 18×100 GeV beam configuration [76]. Blue markers compare the generator level (closed circles) with the reconstructed tracks (open circles) in ep while black markers show the eA case obtained from ep through EPS09 weighting procedure. As can be seem, the proton-nucleus difference is far grater than the reconstruction effects.

for this measurement, t cannot be obtained from measuring the nuclear recoil, it is reconstructed from the meson and scattered electron.

The incoherent cross-section dominates over the coherent at all but the smallest t values. We will thus have no problem measuring it to study the gluon density fluctuations. The challenge therefore lies with isolating the coherent contribution. To this end we show that using a set of 'particle veto' cuts that demand minimal-to-no activity in the far-forward detectors allows suppression of the incoherent contributions by several orders of magnitude (reduction from the solid line to closed markers in Fig. 3.11. Therefore, even without the direct detection of the scattered nucleus we can obtain a data sample dominated by coherent production events up to $|t| \sim 0.1$ GeV^2.

With these data one would like to map the positions of the first minima that relate to the spatial extent of the gluon density. While the idealized Sartre calculation predicts very distinct minima, the addition of more realistic nuclear effects is expected to smear them out such that only changes of the distribution shape (t slope) will be visible. As shown, the ECCE t reconstruction resolution is more than sufficient for observing such variations. Last, we note that similar measurements will be done with ρ and ϕ mesons whose comparison with J/ψ data at different x, Q^2 bins is very sensitive to gluon saturation effects. For a study of the ϕ, see Ref. [56].

3.3.4 Azimuthal correlations in dihadron production

Azimuthal distributions in dihadron production processes are sensitive to gluon fields that carry non-vanishing transverse momentum. In the saturation regime we expect the average transverse momenta of the dense gluon fields to be of the order of the saturation scale, $k_T \sim Q_s(x, A)$. Therefore, comparing the angular correlation of hadron production in nuclear and proton targets directly probes the transverse momentum distribution of the gluons and is thus sensitive to saturation effects [77].

At lowest α_s order in QCD, DIS dijet production comes from $\gamma^* q \to qg$ and $\gamma^* g \to q\bar{q}$ processes. The latter virtual photon-gluon fusion process is the one sensitive to the gluon distribution and is of interest for the current analysis. We simulated these processes using PYTHIA6 [76]. The dihadron correlation distributions were created from hadron (i.e. $\pi^{\pm}, K^{\pm}$ and $p/\bar{p}$) pairs with $p_T^{\text{trig}} > p_T^{\text{assoc}} > 1$GeV/c and $|\eta| < 3.5$. Then,

a fit to the dihadron correlation $1/N_{evt}\ dN^{pairs}/d\Delta\phi$ with two Gaussians and a constant was performed. The comparison between the generated and reconstructed distributions for ep is shown in Fig. 3.12. Small differences between the two distributions are observed, which we consider as a contribution to the systematic uncertainty of the measurement.

Figure 3.12 also shows the comparison of the dihadron correlations in ep and eAu scattering. The eAu calculation was done by weighting half of the simulated ep events by the nuclear modification factor $R_i^A(x, Q^2)$ from the EPS09 nuclear parton distribution set (where the struck parton is identified by scanning the PYTHIA6 event record). There is a clear reduction of the away-side peak for the eAu case with respect to the ep case is visible, and it is larger than the systematic uncertainty and is therefore a sensitive probe of saturation effects in ECCE.

3.3.5 Passage of particles through nuclear matter

An important information about the properties of cold nuclear matter can also be provided through studies of the final states in DIS. In DIS on nuclei the virtual photon interacts with the quark from the target which then subsequently travels through the nucleus, and interacts with the color charges inside. The quark will eventually hadronize and form the color neutral hadron. The process of the hadronization can take place inside or outside of the nucleus, which in turn depends on the energy and the mass number of the nucleus. Since the hadronization of quarks involve the color neutralization, it is ultimately linked to the property of confinement in QCD.

Semi-inclusive DIS in eA provides an excellent process to address the questions of hadronization, with well-controlled kinematics of the final state particles. Of particular interest is the heavy quark production which will provide a clean probe of gluon dynamics in the nucleon/nucleus. The EIC has unique potential to measure medium-induced parton energy loss when the quark hadronizes outside the cold nuclear medium and explore the interplay between the hadronization and the medium induce energy loss when the hadronization is inside the nuclear matter. By comparing the heavy quark production in ep and eA the EIC can provide an ideal environment to explore the hadronization process in vacuum and a cold nuclear medium.

In Fig. 3.13 the nuclear modification factor is shown for 10+100 GeV collisions for the $D^0(\bar{D}^0)$ production. Three plots correspond to three pseudorapidity bins $-2 < \eta < 0$, $0 < \eta < 1$, $2 < \eta < 3.5$. The nuclear modification factor is plotted as a function of the hadron momentum fraction $z_h = p_h/p_{\text{jet}}$. The theoretical predictions based on the parton energy loss model [78] are shown in Fig. 3.13 in the respective pseudorapidity bins. Systematical uncertainties in these simulations include reconstructed $D^0(\bar{D}^0)$ yield variations from different detector designs and different magnet options. We see that the projected precision of the experimental data will allow to determine the shape in z_h and η of the nuclear modification factors and thus this process offers a great discriminating power between different model predictions for hadronization. Additional studies on jet propagation through nuclear matter can be found in an ECCE note [79].

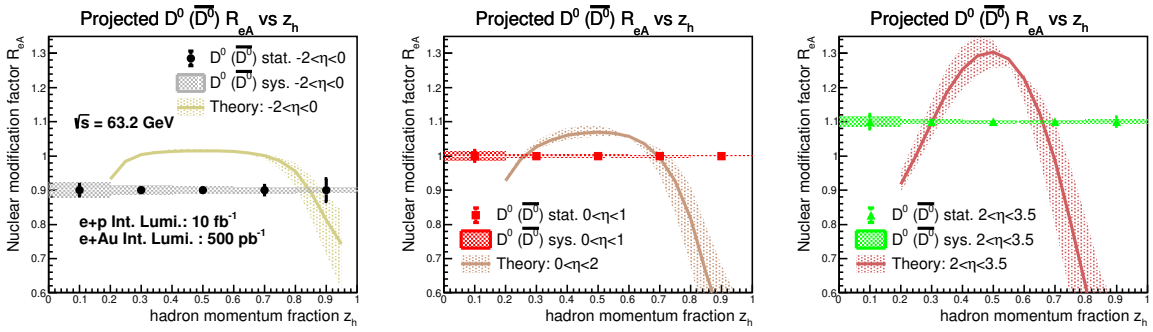

Figure 3.13: Hadron momentum fraction z_h dependent nuclear modification factor R_{eAu} for reconstructed D^0 ($\bar{D^0}$) with the ECCE detector performance in 10+100 GeV ep and eAu collisions [55]. The integrated luminosity for ep (eAu) collisions is 10 fb^{-1} (500 pb^{-1}). The systematical uncertainties come from different detector design and magnet options.

3.4 Origin of hadron mass

The mass of the nucleon dominates the mass of the visible world. Understanding how the nucleon, or more generally the hadron, mass emerges in QCD is therefore a key focus of the EIC science program.

As the total mass of the constituent quarks of gluons (originating from the Higgs mechanism) only account for a small fraction of the nucleon mass, our goal is to determine how the bulk hadron mass is generated from quark and gluon currents. The decomposition of hadron mass into such quark and gluon field operators is not unique, with several decompositions existing in the literature [80–83]. Those decompositions in which each term can be connected to physical observables, within a controlled approximation, can be studied by ECCE.

Such studies will promote our understanding of QCD via attice QCD, mass decomposition approaches, and model calculations. The combination of all three approaches will enhance our understanding of QCD using both fundamental and effective degrees of freedom, as the QCD landscape evolves from a wave-like character at small-x and low-Q^2 to a particle-like character at high-x and higher-Q^2.

3.4.1 Detector requirements for origin of mass measurements

Five key measurements at the EIC were highlighted in Refs. [84, 85] as expected to deliver far-reaching insights into the dynamical generation of mass and two are discussed here. The detector requirements for these measurements are overall similar to those discussed in the 3D tomography section, including the measurements of heavy meson production over a wide range of t and Q^2, as well as excellent detection of far-forward going mesons. Here we show results for two such studies.

3.4.2 Heavy-quark threshold production

Heavy-quark threshold production (e.g. J/ψ, Y) can provide insight into the generation of mass from the vacuum through the trace anomaly. In such measurements one always introduces quarks in the vacuum, one can cleanly relate the measured data to the trace anomaly. Such extraction involve model assumptions that, for the most part, cannot be tested directly using existing data but will be tested by the ECCE data.

By mapping both the t and Q^2 dependence of threshold J/ψ production, ECCE will provide theory with an extended data set that can probe both the trace anomaly contribution to the nucleon mass and its extraction model (using the measured Q^2 dependence to test the assumed production mechanism). The sensitivity of ECCE to the Q^2 dependence of threshold J/ψ production and its impact on our understanding of the 2-gluon mechanism is shown in Fig. 3.14. The projection of the trace anomaly contribution to the proton mass (M_a/M_p) was obtained by assuming the vector meson dominance (VMD) model. Using the ECCE

Q^2-dependence data this assumption will be tested allowing the data to be analyzed in different ways to assess any model dependencies associated with this extraction.

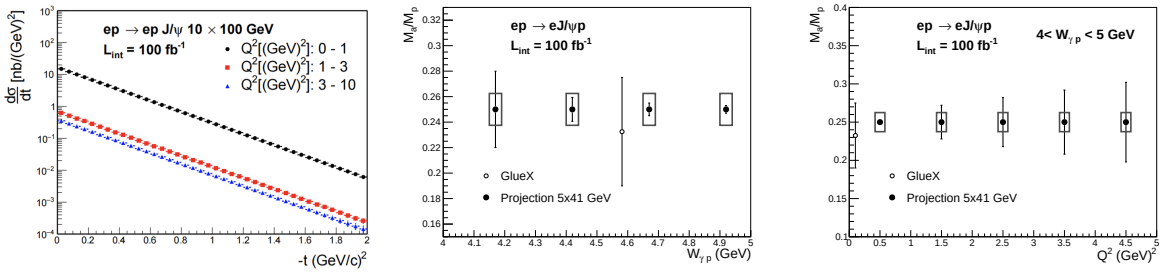

Figure 3.14: Left: ECCE reach for measuring the Q^2 dependence of threshold J/ψ production [86]. Center and Right: $W_{\gamma p}$ (center) and Q^2 (right) dependence of the extracted trace anomaly contribution to the proton mass. statistical and systematic uncertainties and indicated by bars and boxes, respectively. The VMD model used herein does not show any Q^2 dependence, an assumption that the ECCE data will allow to test.

3.4.3 Meson Structure

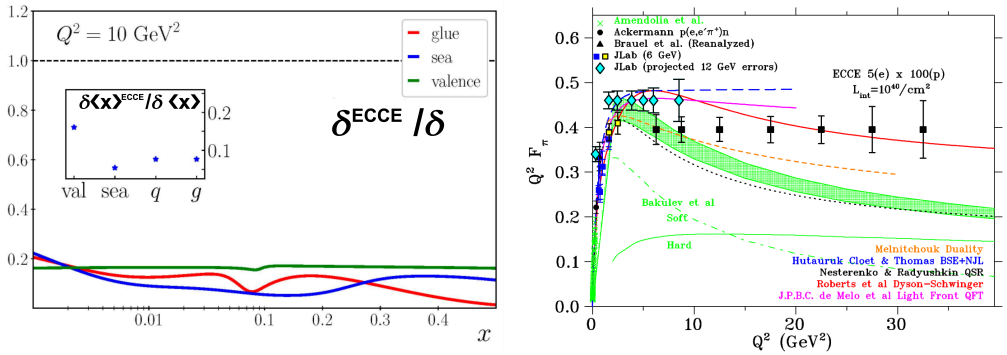

Figure 3.15: Expected ECCE results for the pion structure measurements. Right: form factor results, extend the Q^2 range up to 30 GeV^2. Left: Impact results for the ECCE pion structure function data on the extraction of the pion PDF. The insert shows we expect an average improvement of $\sim \times 10 - \times 20$ in the accuracy of the PDF with the introduction of the ECCE data.

A complete understanding of QCD requires detailed understanding of fundamental building blocks of nuclear matter, such as pions and kaons, alongside protons and neutrons. The substantially different masses of pions and kaons compared with nucleons indicate that the quark and gluon potential energies play a different role in the generation of their masses. Therefore, obtaining a consistent understanding of all four hadrons will allow the different dynamics that contribute to the production of mass in QCD to be disentangled in order to: (i) understand QCD mass generation beyond the nucleon and its interplay with the Goldstone mechanism, and (ii) probe the interplay between mass generation by QCD dynamics and the Higgs interaction.

Within a chiral symmetry approach to QCD, mechanisms that lead to dynamical chiral symmetry breaking (DCSB) are responsible for the emergent hadronic mass and should manifest themselves in observables that probe the shape and size of the hadron wave function. Therefore, considering the chiral limit provides understanding and consistency checks that allow the use of pion structure data to secure key insights into the emergent-mass contributions [84, 85, 87, 88]. For example, any mass decomposition must fulfill the cancellations leading to the small pion mass, where various terms are expected to remain non-zero (trace anomaly, quark/gluon momentum fractions).

Using far-forward tagging, ECCE will measure meson structure functions and form factors over a wide range of Q^2. The structure function measurements provide information about the quark/gluon momentum fractions, while the form factors inform how emergent mass manifests itself in the wave function.

Our studies show the overall ECCE performance for these measurements are comparable to those obtained in the Yellow Report. This is shown in Fig. 3.15 for the ECCE measurements of the pion form-factor (right) and our impact on the extracted PDFs (left). Our expected accuracy are similar to those obtained in the Yellow-Report studies and will have major impact on our understanding of meson structure and the origin of its mass.Similar results are also expected for kaon structure measurements through the Sullivan process (by tagging the Λ decay). Due to the heavier mass of the strange quark, the combination of pion and kaon data will provide information on the interplay between the Higgs mechanism and quark/gluon dynamics in the production of meson mass.

For further details, see the ECCE note, Ref. [75].

3.5 Science beyond the NAS Report

3.5.1 Precision Electroweak and BSM Physics

A combination of higher energy than existing fixed-target facilities and higher luminosity than HERA provides the EIC with a unique role in precision measurements that probe the electroweak sector of the Standard Model (SM) and in searches for beyond-SM (BSM) physics. These include measurements of the weak mixing angle, searches for charged lepton flavor violation (CLFV) and leptoquarks, axion-like particles, tensor charges, general SM Effective Field theory (SMEFT) constraints and more. While going beyond the main scope of the EIC white paper and National Academy of Science report, ECCE collaborators have a keen interest in such studies and find this to be an important research avenue that should be developed further (see ECCE note, Ref. [89] for details).

Detector requirements for precision EW and BSM searches

We start with leptoquark searches which benefit from ECCE's precise vertexing capability, then describe the extraction of the weak mixing angle as presented in the YR, and then extend the discussion to include SMEFT analysis that set constraints on BSM dimension-6 operators.

Leptoquarks

SM rates for charged lepton flavor violating (CLFV) processes are extremely small, many BSM models predict enhanced rates that are within reach of present or future experiments. Here we study ECCE's sensitivity to the CLFV process $e^- + p \to \tau^- + X$ that could be mediated [90–92] by leptoquarks of the SU(5) Grand-Unification Theory (GUT). We simulated 1 M events each of leptoquark signal, DIS NC and CC, and photoproduction background events. The identification of CLFV candidate events focused on a high-p_T quark jet along with an isolated high-p_T τ. The τ identification uses the "3-prong" decay mode containing three charged final state particles with a $\sim$15% branching ratio.

A total of ten selection criteria were used to select $e \to \tau$ events with minimal to no background (within MC statistics). The most significant discrimination comes from the reconstructed τ decay length, owing to the 20–30 μm vertex resolution of the ECCE tracker (Fig. 3.16 (left)). Normalizing all event types by their expected total cross sections, and using a 3σ (99.7% C.L.) criterion, we found our sensitivity to leptoquark cross section to be 11.7 fb if detecting only the 3-prong decay, or 1.8 fb if we assume the same detection efficiency for all decay modes. We note that our selection cuts removed all simulated NC and photoproduction background events, though in reality some background could remain that would impact the ECCE limit.

The exclusion potentials from our analysis, expressed in terms of the four-fermion contact interaction term $\lambda_{1\alpha}\lambda_{3\beta}/M^2_{LQ}$, are shown in Fig. 3.16 for the scalar leptoquark cases. ECCE is expected to provide better limits than HERA and offer sensitivity in channels not accessed by $\tau \to e\gamma$ decay.

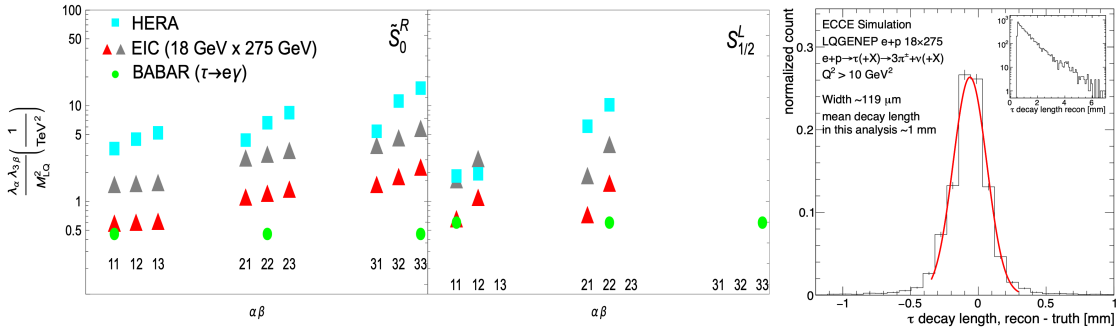

Figure 3.16: (Left) Limits on the leptoquark-mediated four-fermion contact interaction term, for leptoquarks with fermion number $F = 0$ $\tilde{S}^L_{1/2}$ (left) and $|F| = 2$ $\tilde{S}^R_0$ (right) from 100 fb^{-1} of ep 18 × 275 GeV data, based on a sensitivity to leptoquark-mediated $ep \to \tau X$ cross section of size 1.8 fb (red triangles) or 11.7 fb (grey triangles) from ECCE. Also shown are limits from HERA [93–96] (cyan squares) and $\tau \to e\gamma$ decay [90] (green circles). (right) Difference between reconstructed and truth τ decay length for the ECCE detector. The resolution is found to be 119 μm and is sufficient for the τ vertex identification.

Weak Mixing Angle Extraction from Neutral Current DIS

ECCE can extract $\sin^2\theta_W$ from measurements of Parity Violating DIS (PVDIS) asymmetry due to electron spin flip: $A_{PV}^{(e)} \equiv \frac{\sigma_R - \sigma_L}{\sigma_R + \sigma_L}$ (where $\sin^2\theta_W$ enters through the electron and quark NC couplings).

As the statistics required for electroweak studies is high, we used fast simulations with realistic smearing obtained from our full GEANT4 simulations. Data were divided into (x, Q^2) bins, and the statistical precision of the PVDIS asymmetry was calculated assuming 15.4, 100, 44.8, and 36.8 fb^{-1} for beam energies of $18 \times 275(137)$, $10 \times 275(137)$, 10×100, and 5×100 GeV for ep (eD), respectively. The electron beam polarization is assumed to be 80%.

For each $\sqrt{s}$ setting we assumed a conservative uncorrelated relative 1% uncertainty in each bin due to background, and a relative 1% due to electron beam polarimetry (correlated for all (x, Q^2) bins). In addition, we evaluated the PDF systematic uncertainties using the eigensets of CT18NLO.

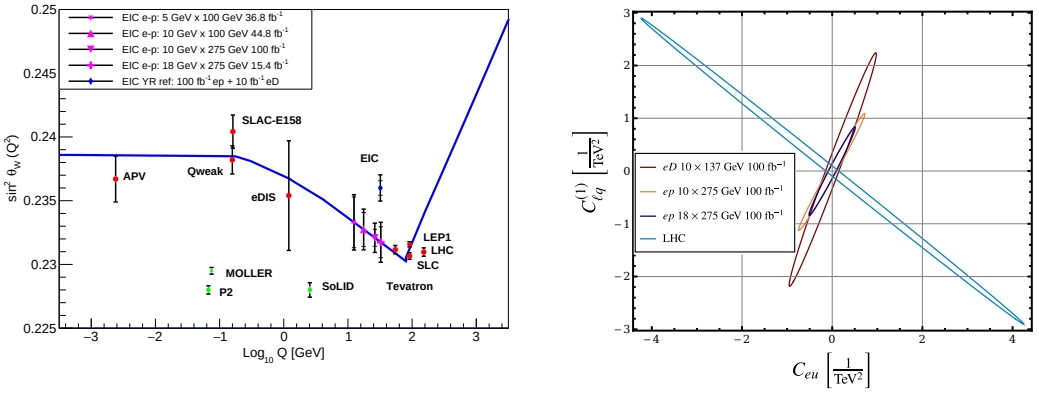

Figure 3.17: LEFT: Projected results for $\sin^2\theta_W$ using ep collision data (magenta) and the "YR reference point" (blue), compare with existing (red) and future [97–100] (green) experiments and SM prediction (blue curve) [101]. The inner and outer error bars differ in the inclusion of the 1% beam polarization uncertainty. RIGHT: The 95% CL ellipses in C_{eu} vs. C_{ed} SMEFT Wilson coefficients from the PVDIS asymmetries of unpolarized deuteron and proton compared with LHC constraints [102].

Figure 3.17 shows the expected accuracy in extracting $\sin^2(\theta_W)$ from ep measurements with four beam

energy settings. For reference we also show a the EIC YR expected accuracy, obtained by combining 100 fb^{-1} of 18×275 GeV ep and 10 fb^{-1} of 18×137 GeV eD data. Performing a similar combination, our expected uncertainties are consistent with the YR expectation.

SMEFT Analysis

The Standard Model Effective Theory (SMEFT) [102–105] framework is a systematic approach to include the effects of BSM degrees of freedom that become active at some energy Λ beyond the electroweak scale. In SMEFT, BSM physics is represented by contact interactions of dimension 6 or higher, and the full Lagrangian is given by $\mathcal{L} = \mathcal{L}_{\text{SM}} + \sum_i C_i \mathcal{O}_i + \cdots$, where $\mathcal{L}_{\text{SM}}$ denotes the SM Lagrangian, $\mathcal{O}_i$ denote dimension-6 contact interaction operators, $C_i \sim 1/\Lambda^2$ denote the corresponding Wilson coefficients, and the ellipses denote operators of even higher dimensions.

An SMEFT analysis was performed with the projected PVDIS asymmetry data, Figure 3.17 (right) shows the expected ECCE limits on two sets of Wilson coefficients obtained with ep and eD collisions at the highest luminosity. The derived limits are complementary to those provided by Drell-Yan data at the LHC.

Tensor Charges

The ECCE extraction of transversity distributions for spin studies can also be used for BSM searches. When integrated over x, the transversity distributions provide the tensor charges of the nucleons. While well predicted in the SM by Lattice QCD calculations, this value can be modified by the existence of BSM tensor interactions [106]. By searching for deviations from the lattice predictions we can test and constrain such BSM contributions. This has not been possible due to the limited x range of existing data and uncertainties due to the related fragmentation functions. However, our studies indicate that ECCE can provide a precise extraction of the tensor charges that are on-par with current Lattice extractions (Fig. 3.5).

3.5.2 XYZ spectroscopy

Spectroscopy of mesons with charmed quarks has provided some of the most surprising recent results and raised many interesting questions. These new "XYZ" meson states have unexpectedly narrow widths and masses that are inconsistent with quark model expectations. Most of these new states have only been seen via single production mechanisms such as B decays or e^+e^- annihilation, making it difficult to resolve the dynamics contributing to their formation. Photoproduction measurements using polarized beams in ECCE offer an alternative production method for probing the underlying dynamics (tetraquark, molecules, hybrids), allows determination of their quantum numbers, and can search for broader overlapping states that have yet to be identified. While heavy quark states have small production cross sections, many are expected to be produced at a sufficiently high rate to be measurable with ECCE [107].

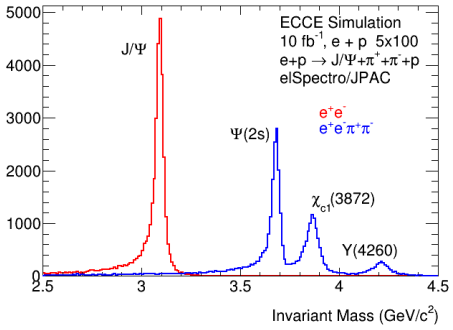

Figure 3.18: Reconstructed invariant masses for meson decay products, with the three states of interest clearly observed. Resolutions for $M(e^+e^-)$ and $M(e^+e^-\pi^+\pi^-)$ are around 30 MeV. The $Y(4260)$ invariant mass is wider due to its decay width (taken as 50 MeV).

A custom developed generator for spectroscopy reactions at EIC was used to estimate ECCE performances. The helicity amplitudes were calculated following Ref. [107]. We study three selected states, $\chi_{c1}(3872)$ (or $X(3872)$), $Y(4260)$ and the well established quark model state $\psi(2s)$. All of these states have decay branches to $J/\psi\pi^+\pi^-$ and so we focus on reconstruction of this final state with the J/ψ decaying to e^+e^-. This allows comparing expected production of exotic states to a regular quark-antiquark meson and check if we can distinguish the invariant mass peaks of these relatively close states. Details on the simulation and analysis are described in ECCE note, Ref. [108].

Figure 3.18 (right) shows the reconstructed invariant mass distributions. The resolutions for $M(e^+e^-)$ and $M(e^+e^-\pi^+\pi^-)$ are approximately 30 MeV — sufficiently narrow to be able to distinguish many of the final state mesons. The good resolution for the J/ψ mass also helps reduce background form events without this meson. The ECCE detector is thus very promising for studies of exotic meson spectroscopy with the EIC. In particular, at mid centre-of-mass energies the meson decay products are nicely distributed throughout the central detector.

The detection of low energy pions in this reaction is particularly important and challenging, suggesting that the use of a lower solenoid field is optimal for measuring such reactions.

3.5.3 u-Channel DVCS

Measurements of u-Channel DVCS ($ep \to e'p'\gamma$) and π^0 DEMP ($ep \to e'p'\pi^0$, with $\pi^0 \to \gamma\gamma$) reactions provide access to the valence quark component of the nucleon wave-function in a particularly clean manner. In analogy to forward-angle GPD factorization, these measurements require the identification of a significant backward-angle cross-section peak in a variety of exclusive channels over a wide range of kinematics, to investigate the kinematic onset of the backward-angle collinear factorization theorem. Compared to its t-Channel counter part, the u-Channel DVCS carries an unique advantage as the competing Bethe-Heitler process is suppressed in the backward kinematics.

Detection of the u-Channel exclusive DVCS and π^0 DEMP reactions include measurement of scattered electrons by the Electron-End-Cap and recoiled protons at high η by the Hadron-End-Cap; At the kinematics of interest ($W = 3.16$ GeV, $u \sim u_{min}$, $6 < Q^2 < 10$ GeV^2) the relevant γ will will have energy of about 40 to 60 GeV and reach both ZDC and B0 calorimeteres. Fro DEMP, all π^0 decays result in at least one γ that is detected by the ZDC with 40% of the events having both detected there. For the remaining 60% using the ZDC alone we will not be able to separate the DVCS and π^0 DEMP reactions. As the u-Channel DVCS cross section is 10-100 times smaller than that of the u-Channel π^0 DEMP, the DVCS measurement can only be done using the B0 to measure photons which allows for a good separation of DVCS (single γ) and π^0 DEMP (two γ) reactions. Furthermore, when $u \sim u_{min}$ measurement, the proton recoil at $\eta \sim 4.1$ and some protons will miss the acceptance of Hadron-End-Cap. In this case, a good γ measurement by the $B0$ Calorimeter is needed to reconstruct the proton using missing mass technique to ensure exclusivity.

This motivated instrumenting the B0 spectrometer with a $PbWO_4$ calorimeter. This leads to an increase in the effective γ coverage from ± 5 mrad (ZDC) to ± 23.7 mrad. The π^0 DEMP two photon detection efficiency will increase from $\sim$40% (at the momentum of 40-60 GeV) to $\sim$90%, which will significantly help in rejecting the π^0 background to the DVCS measurement. Furthermore, once a DVCS like event is measured, the energy resolution provided by the $PbWO_4$ will allow to ensure exclusivity of the $ep\gamma$ final state. See Sec. 2.6.1 and ECCE tech-note [75] for detail.

3.6 Magnetic Field Strength Impact on Physics Performance

The choice of solenoid magnet dimensions and field strength is a key consideration when designing a collider detector. Scaling with the collision energy and depending on the physics program, modern collider magnets vary in strength from 0.5 T (Alice) to 4 T (CMS). While ECCE is using the existing 1.4 T BaBar solenoid, as a comparative study we repeated selected physics simulation studies with a higher (3.0 T) and lower (0.7 T) magnetic field to ensure that our magnet choice does not limit our ability to address the EIC science program.

To this end we performed studies of jet and heavy flavor measurements, di-hadron correlation measurements, XYZ spectroscopy, A_1 SIDIS spin asymmetries and coherent J/ψ production off of nuclei. We note that while the magnetic field strength and bore radius are strongly coupled parameters (and can have compensating effects on tracking resolutions, etc), we tested the magnetic field strength impact on the performance of the ECCE detector by simply changing the magnetic field in the current ECCE design, without optimizing either the magnet or detector configuration.

Considering the general kinematic reconstruction of DIS reactions (i.e. x and Q^2 measurement), we expect for the higher field to improve the scattered electron momentum measurement, especially at large $|\eta|$. Our

simulation studies indeed show that the use of a 3.0 T magnetic field leads to some improvement in the scattered-lepton based reconstruction at lower y. Using the 1.4 T field in this kinematic region, for improved reconstruction one needs to also measure the hadronic final state to use the double angle or Jaquet-Blondel reconstruction methods. For SIDIS reactions the magnetic field seems to have minimal impact to the z reconstruction, except at very high-z where some improvement is observed. The high-field improvement of the high-momentum particle tracking comes at the expense of low-momentum particle acceptance. Our SIDIS studies indeed find a substantial reduction of acceptance for hadron momenta below 1 GeV when using 3.0 T field. Looking at the extraction of physics observables such as the SIDIS A_1 asymmetry, we observe almost identical kinematic reach for the 1.4 T and 3.0 T with a slightly ($< 20\%$) improved uncertainty for the 1.4 T field at low z and an essentially identical uncertainties at high z (see ECCE technical note [109] for details).

Considering jet measurements, the relatively modest center-of-mass energy of the EIC leads to jets with a large fraction of low-p_t particles, espcially at mid-rapidity. Therefore, the measurement of parameters like the Jet Energy Scale (JES) and resolution functions are a delicate balance between low-p_T acceptance that improves at low field and higher-resolution measurement of high-p_T tracks that improves at higher field. Figure 3.19 shows the JES distributions for mid-rapidity SIDIS jets with $Q^2 > 10$ GeV^2 and different field strengths. As can be seen, the 3.0 T field setting leads to an increased low-side tail due to the decreased acceptance for low-p_T charged particles. For higher rapidity the 0.7T performance is becoming lower compared to 1.4T and 3.0T with the latter field showing a very slight improvement. For further details on jet performance in ECCE, see ECCE technical notes Ref. [54] and Ref. [110].

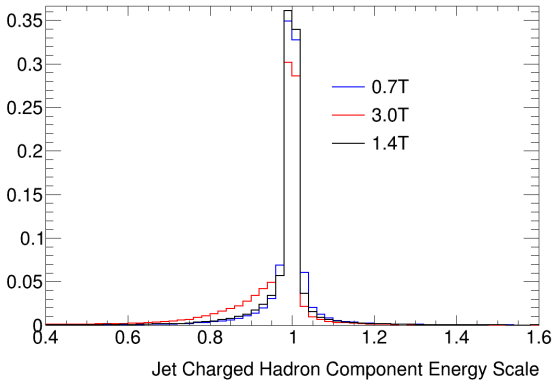

Figure 3.19: Jet Energy Scale (JES) distributions for the charged track component of ECCE Centauro reconstructed track + cluster jets for $\eta_{jet}^{Lab} < 1.0$, with $z_{Jet}^{true} > 0.7$ and $p_{Jet}^{Breit} > 4.0$ GeV/c for different ECCE central magnetic fields. We used Pythia6 SIDIS events with $Q > 10$ and normalized all distributions to unity to facilitate simple shape comparisons.

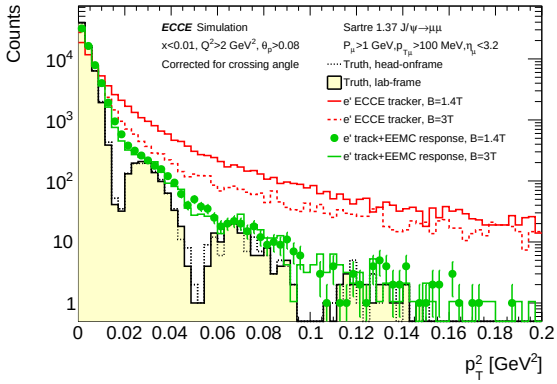

Figure 3.20: Simulation of the t dependence of the elastic diffractive J/ψ production in eA for 1.4 T and 3.0 T field strengths. Results are shown for analyses using information from the tracking (red lines) or tracing + calorimetry (green line and points) systems for the lepton momentum reconstruction. As can be seen, the t reconstruction resolution is dominated by the calorimetry resolution the field strength has small impact on this measurement.

Similar effects are seen in measurements of nuclear modification effects on heavy-flavor production (Fig. 3.21). While the higher magnetic field leads to a narrower D^0 ($\bar{D^0}$) reconstruction peak, improving the overall signal/background ratio of the measurement, it also has lower total signal statistics due to the loss of the soft pion from open heavy-flavor decay. The net result is an overall similar statistical uncertainty for the net background-subtracted signal for the different magnetic field settings.

For di-hadron fragmentation functions measurements, a partial-wave decomposition of the hadron pairs will be needed in order to separate the contribution of different PDFs and higher twist functions inside the nucleon. Performing such partial-wave decomposition require measuring as large as possible fraction of the

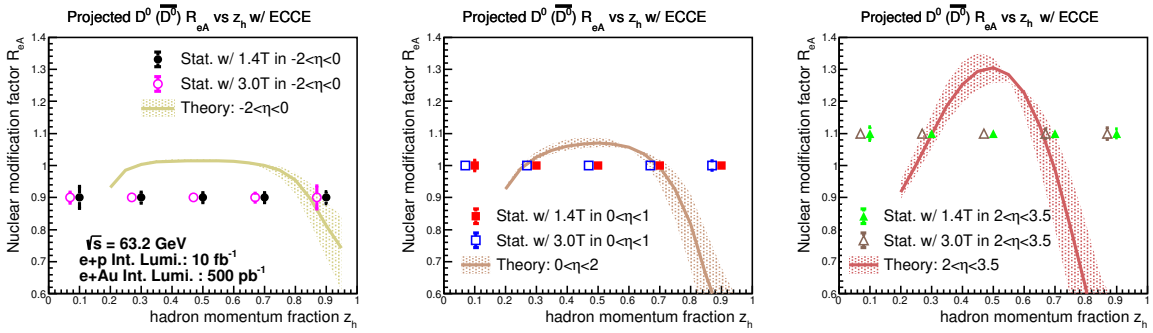

Figure 3.21: Hadron momentum fraction z_h dependent nuclear modification factor R_{eAu} for reconstructed D^0 ($\bar{D}^0$) with the ECCE detector performance in 10+100 GeV ep and eAu collisions. The integrated luminosity for ep (eAu) collisions is 10 fb^{-1} (500 pb^{-1}). The statistical uncertainties of the projected R_{eAu} with the ECCE detector performance using 1.4 T and 3.0 T magnetic fields are shown in closed (open) markers. The theoretical calculations are from [111].

di-hadron phase space, including very asymmetric energy and momentum combinations. Our simulations show that a significant fraction of the di-hadron phase-space is at low-p and will thus benefit from lower magnetic field with improved low-p_T acceptance. Similar effects were also observed in XYZ spectroscopy studies that also improve their statistical reach with improved low-p_T acceptance.

Last, we turn to the $t-$dependence of coherent diffractive J/ψ production. As mentioned previously, the fact that for the relevant low-t kinematics the recoil nucleus cannot be measured means that t is reconstructed using the scattered electron and reconstructed J/ψ; i.e. it is a small quantity obtained by subtracting much larger ones. It is thus highly sensitive to resolution effects and was presented as a driver of the tracking resolution requirements in the Yellow Report. Figure 3.20 compares the simulated t-dependence of coherent diffractive J/ψ production for different magnetic field strengths. As can be seen, the higher field leads to a reduced smearing and thus an improved measurement. However, it is overall a modest improvement and is not a driving consideration for this measurement. In fact, our studies show that the EM calorimetry resolution is the dominant factor for this measurement. For further details, see ECCE note [75].

Based on the selected studies discussed in this chapter of the proposal, and many other detailed studies of physical processes presented in the various ECCE physics technical notes, we conclude that the use of the 1.4 T BaBar solenoid in ECCE does not present any significant impediments to pursuing the full EIC science program, and may indeed offer a benefit for specific measurements.

Chapter 4: ECCE Consortium

4.1 Structure and Management

For the preparation of the detector proposal, the ECCE member institutions chose to assemble as a *consortium* as opposed to a *collaboration*. A decision was taken to organize around a flexible framework that allowed member institutions to focus on the detector design and performance studies with minimal overhead. Following the proposal review process we will evolve the ECCE consortium into a full collaboration. As we expect some realignment of institutional efforts within the EIC community following the selection of the project detector, forming the collaboration at this stage will allow new institutions joining ECCE to participate fully in this process. This section summarizes the consortium structure and outlines the process by which we expect it to evolve into a more traditional collaboration.

The ECCE Consortium: The ECCE consortium consists of 96 member institutions (see Table A.1). Of these, $\sim$ 55% are international and $\sim$ 45% are U.S. based (see Fig. 4.1). The latter include graduate universities ($\sim$ 70%), undergraduate and minority serving institutions ($\sim$ 15%), and national labs ($\sim$ 15%). The groups are approximately evenly distributed between those that have their background in electron scattering and in heavy-ion physics. This gives the consortium a broad scientific foundation to maximize the physics output of the EIC.

The consortium is managed by a Steering Committee (SC), consisting of O. Hen (MIT), T. Horn (CUA), and J. Lajoie (Iowa State). They serve the Institutional Board (IB) and coordinate five 'Teams', each led by two or three co-conveners, that focus on the different areas of study that went into this proposal. These include:

- **Detector Team:** D. Higinbotham (JLab) and K. Read (ORNL),
  Oversees the technology selection studies, including their GEANT4 implementation and performance studies. This team includes seven individual working groups, each focused on different detector elements (Tracking, Calorimetry, PID, Far-forward/Far-backward Magnet, DAQ/Electronics, and Infrastructure reuse).
- **Physics Benchmark Team:** C. Munoz-Camacho (IJCLab-Orsay) and R. Reed (Lehigh U.),
  Using full GEANT4 simulation to study the detector performance in terms of sensitivity of concrete physical observables. This team consists of seven working groups, each focused on different reaction types (Inclusive, Semi-Inclusive, Exclusive, Diffraction and Tagging, Jets and Heavy Flavor, BSM and Precision Electroweak, and Simulation integration and support).
- **Computing Team:** C. Fanelli (MIT) and D. Lawrence (JLab),
  Oversees the ECCE simulation infrastructure and coordinates its running on different clusters. This team supports the use of different event generators and the implementation of analysis tools. Responsible for the use of Artificial Intelligence techniques for detector optimization and the development of the ECCE Software and Computing Plans.
- **Diversity Equity and Inclusion Team:** N. Kalantarians (VUU) and C. Nattrass (UTK),
  Responsible for developing the ECCE code of conduct, advise the SC on convener appointments, and handling misconduct complaints.
- **Project and Editorial Team:** T. Cormier (ORNL), R. Milner (MIT), and P. Steinberg (BNL)
  Leads the detector costing, schedule and risk assessments effort with the help of project management professionals from ORNL. Responsible for the document management system in ECCE.

The Teams work in close collaboration with each other and engage the full consortium via their working groups. These groups are mostly led by a diverse set of postdocs and junior faculty who previously made

significant contributions to the EIC Yellow-Report. This group of young hands-on ECCE leaders are already emerging as clear leaders in the EIC physics community, publishing works on EIC physics and leading global initiative such as AI4EIC and different workshops on EIC physics. Consortia members also worked very closely with relevant theoreticians who help guide our physics studies and incorporate our results into global analyses.

The ECCE Collaboration: The transition of ECCE from a consortium to a collaboration will take place as part of a 'collaboration formation meeting' that we expect to take place soon after the proposal review is completed and span several days. In that meeting the members of the new ECCE collaboration will agree on its final structure, conduct spokesperson and IB chair election, and initiate the collaboration bylaws formulation process. We emphasize that the decision to defer this process until after the proposal review is motivated by the expectation that the outcome of the review process will lead to changes in how the EIC physics community arranges itself around the different efforts. Specifically, we expect new groups will join ECCE and ensure they are integrated into our structure in a way that allows ECCE to make the most of their expertise. To this end we believe it is important for new groups to take an active part in the collaboration formation process and not be tied down by existing bylaws and an already appointed leadership team. Therefore, while discussions at the 'collaboration formation meeting' will be initiated based on the structure described below (that is endorsed by the ECCE consortia IB), we will have the ability to refine and modify it to best fit the outcome of the proposal review process. The needs and views of the new collaborating institutions will be incorporated to further strengthen our ability to deliver an on-time and on-budget project detector. While the final structure of the ECCE collaboration will ultimately be determined by the collaborating institutions after the proposal review is complete, we describe below the starting point for discussions of this structure.

The proposed ECCE collaboration structure was developed by the ECCE consortium IB. It emphasizes key leadership positions, and their areas of responsibility, that are necessary to allow the ECCE *collaboration* to deliver on three main objectives:

- Work with the EIC project to deliver an on-time and on-budget project detector
- Develop monitoring tools required to support EIC commissioning using the ECCE detector
- Develop the data processing and analysis tools required to produce physics results very soon after data are starting to be collected.

To meet these goals the proposed collaboration leadership structure consists of a collaboration elected IB chair and Spokesperson, and a spokesperson appointed leadership team with two Deputy Spokespersons and a series of Coordinators (technical, detector resources, physics, run, diversity equity and inclusion, and software and computing). Below we detail the expected responsibilities of each position in the leadership team:

- **Spokesperson and Deputies** are expected to manage and coordinate the collaboration activities and scientific output. This includes, for example, arrangement of regular collaboration meetings, oversight of scientific priorities, assessment of run plans and needs, coordination of communication with the EIC project, and solicitation and integration of new groups. We envision for the Spokesperson to be elected by the collaboration for a two year term and for a significant onsite presence to be required of either the Spokesperson or one of their appointed deputies.
- **Institutional Board (IB) Chairperson** is expected to set the agenda for IB meetings, handle any issues raised by collaboration members, appoint selected standing committees (e.g. talks committee) and ad-hoc committees when the need arises by the IB, setup IB votes, and manage the spokesperson election. In contrast to the Deputy Spokespersons and Technical Coordinators, who are appointed by the Spokespersons, the IB chair is envisioned to be elected by the IB for a two year term. We expect that, in the first election, the IB chair will be appointed for three years such that future IB Chairperson and Spokesperson elections are offset by a year.
- **Technical Coordinator** is expected to oversee and coordinate the day-to-day technical aspects of the experimental equipment and any upgrades the collaboration is planning. The Technical Coordinator

position is expected to be filled by a highly experienced scientist with 100% on-site residency. The Technical Coordinator will work closely with the local EIC project teams at both BNL and JLab and with the ECCE Detector Resource Coordinator.

As JLab and BNL are full partners in the EIC project, and significant part of the detector development leadership is foreseen to be taken by JLab, we expect to also appoint a deputy Technical Coordinator with significant on-site presence at JLab. This appointment will allow to best capitalize on the specific strength of each lab in detector construction and development, computing, electronics etc.

- **Detector Resource Coordinator** is expected to oversee and coordinate the user-provided in-kind contributions to the ECCE detector. The detector resource coordinator works hand-in-hand with the collaboration and the EIC Project to help ensure the user commitments stay on track, and to help resolve potential issues. With time, as the detector construction progresses, we expect for the Detector Resource Coordinator role to evolve in a Detector Upgrade Coordinator role. The Detector Resource Coordinator will work in close coordination with the Technical Coordinator at all times.
- **Software and Computing Coordinator** is expected to oversee and manage development and implementation of software tools for the processing of acquired data for physics analysis, and coordinate the detector calibration and physics simulation tasks. The Software and Computing Coordinator will also oversees and coordinates the distributed computing tasks to various clusters available at BNL, JLab and key user institutions.
- **Physics Coordinator** is expected to oversee and manage the physics analysis tasks between the various physics working groups. Their goal is to ensure that physics production data, as well as results from relevant technical studies, are analyzed and published in a timely fashion. The Physics Coordinator is expected to work closely with the theory community to maximize the impact of EIC data.
- **Diversity Equity and Inclusion (DEI) Coordinator** is expected to oversee the general collaboration conduct to ensure ECCE is a welcoming environment were everyone can excel to the best of their abilities, independently of their origin or background. The DEI coordinator will work closely with the collaboration leadership team to help minimize bias (conscious or otherwise) in personnel appointments. They will serve as ex-officio member on all internal committees making personnel decisions (e.g. talks committee) and will be in charge of ensuring the ECCE code-of-conduct and bylaws are upheld. The will also form review committees when complaints of violations come up.
- **Run Coordinator** will be responsible for overseeing real-time data taking and coordinate between the technical teams operating the ECCE detector and the EIC accelerator group. The run coordinator position usually rotates more often than the other coordinator positions, up to several times within a given run period. While in place, the run coordinator is expected to have 100% on-site residency and devote their full attention to this position. We expect this position will be filled as ECCE moves from a construction project into the integration and commissioning phase.

This leadership structure is a direct evolution of the consortium structure that successfully produced this proposal. The steering committee structure will evolve into an elected Spokesperson and the team convener positions will evolve into technical coordinator roles. Each coordinator will be expected to further establish, in consultation with the Spokesperson and Deputies, focused working groups in a manner similar to what was done for the proposal development.

4.2 Diversity, Equity and Inclusion (DE&I)

The ECCE consortium is taking active action to become an inclusive and diverse international scientific collaboration, committed to sustaining a welcoming scientific environment free from all forms of prejudice, discrimination, and harassment. As such, one of our key guiding principles is to conduct ourselves in a way that allows all collaborators to do their job and perform to the best of their abilities, independently of their gender, origin, or background. We thus take active measures to ensure that all physicists, particularly those from historically or currently marginalized or underrepresented backgrounds or identities, are fully

included and have the opportunity to thrive within the ECCE community. This in turn helps maintain our high productivity and scientific integrity.

To that end, the ECCE consortium has a standing Diversity, Equity, and Inclusion Team that worked with the SC and IB to develop a code of conduct with a clear procedure for addressing behaviors that can heart the ability of ECCE collaborators to contribute to the best of their ability. Our code of conduct is flexible so that conduct which interferes with someone's ability to work warrants consideration and likely a response. We do not require a finding that conduct is unambiguously discriminatory, as evidence of discrimination can be difficult or impossible to compile and behavior which would result in sanctions is usually unacceptable even if it is not discriminatory. Sanctions will only be imposed after an investigation by a 3-person committee and can also be flexible to suit the needs of the situation. This is done in response to past experiences with disruptive behaviors within the community, which may not always be predictable. The lowest tier of response can include a discussion about why the behavior was problematic or made someone uncomfortable. The three-person committee is a check to ensure that either a reasonable person would find the conduct to be inappropriate, if no warning is given, or that people are given an adequate warning and a chance to change their behavior before any sanctions which could hurt someone's career. The appropriate sanctions may also depend on the situation. For people in leadership positions, the failure to respond to complaints or incidents may also potentially be a violation of the code of conduct. This ensures that it is in the best interest of all collaborators to ensure that ECCE maintains a positive and productive working environment.

The ECCE approach is different because there is an explicit procedure for dealing with problems, and that this procedure does not require that conduct must be discriminatory, or even that it is misconduct, before being addressed. The threshold for addressing issues is that they interfere with someone's ability to perform their work. With that, responses are not necessarily punitive but emphasize creating a productive working environment that enables open discussion and provides people with room to learn from their mistakes and improve on their conduct moving forward.

We find this to be all the most important here as many ECCE collaborators are early career scientists and ECCE plays a central role in their education of how to interact with colleagues productively. We anticipate that our code of conduct will be in place until a full set of bylaws is approved, and we intend for its features to help guide and shape our collaboration bylaws. Since bylaws which address misconduct are still relatively new, members of the ECCE DE&I committee and SC are also actively engaged in efforts within the APS DNP to develop best practices and working with BNL management to address logistical issues, such as secure record keeping and training for the investigatory committees.

We plan to use the ECCE consortium Code of Conduct as a guide to inform the formation of bylaws, policies, and procedures as we evolve into the ECCE collaboration.

4.3 Consortium Roster, Expertise and Responsibilities

The ECCE consortium consists of 96 institutions whose expertise in nuclear physics research include work at all JLab Halls, the STAR, PHENIX, and sPHENIX experiments at BNL, the LHC experiments and more. A full list of consortium member institutions is given in Table A.1, alongside the detector sub-systems each institution expects to be working on for the development and construction of ECCE. The composition of our member institutions in terms of country of origin is given in Fig. 4.1. For U.S. based institutions we also show breakdown in terms of graduate awarding institutions, undergraduate and minority serving institutions (MSIs), and national labs and for non-U.S. institutions highlight the specific detector sub-systems they expressed interest working on as in-kind support for the project (see section 5.3 for details).

As can be seen, the consortium is large, diverse, and encompasses a wide range of expertise from electronics engineering and mechanical design, to detector R&D, to setup of detector production, assembly, and test lines. It is thus highly qualified to build the ECCE detector. The way the consortium expertise is expected to be put to use for the construction of the different ECCE subsystems is shown in Fig. 4.2. Additional details are given in the project plan discussed in Section 5.

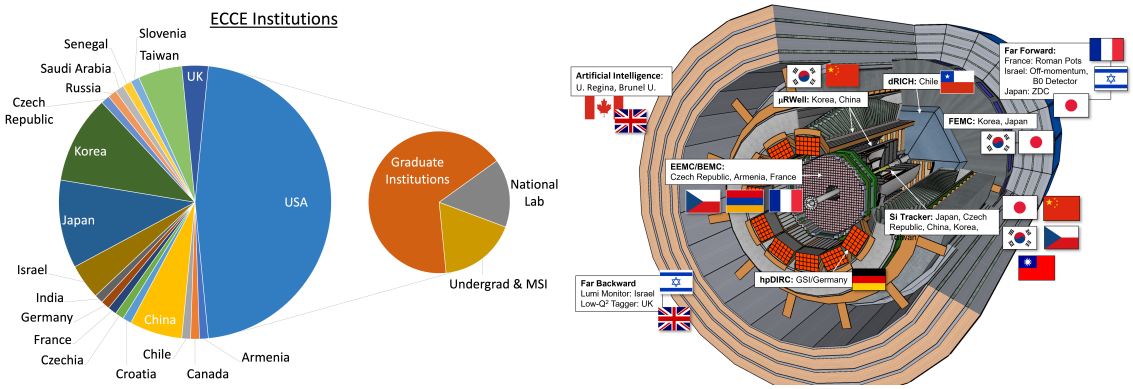

Figure 4.1: Origin distribution of ECCE consortium member institutions.

Region	System	Technology	Institutions	Experience / Comments
Forward Endcap (Hadron direction)	Tracking	ITS-3 Si Disks	LANL, LBL, ORNL, MIT/BATES, EIC-China, EIC-Taiwan, EIC-Korea, Brunel (UK), Regina (Canada), Czech. Tech. Univ., BNL	Experience constructing previous Si trackers, most recently for sPhenix.
	PID	AC-LGAD	RICE, ORNL, BNL, UTSM	Experience in CMS
		dRICH	UConn, Duquesne, Duke, JLab, Tsinghua/China	E&D (strong engineering) Simulations (Hall B RICH, Hall A/SBS RICH), HERMES RICH refurbishment
	EM Calorimetry	Longitudinally segmented, scintillating tile	ORNL, ISU, Ohio U., EIC-Japan, EIC-Korea, EIC-China, BNL	Experience with calorimeters in sPHENIX and ALICE
	Hadron Calorimetry			
Barrel	Tracking	ITS-3 Si (vertex & sagitta)	LANL, LBL, ORNL, MIT/BATES, EIC-China, EIC-Taiwan, EIC-Korea, Brunel (UK), Regina (Canada), Czech. Tech. Univ., BNL	Experience constructing previous Si trackers, most recently for sPhenix.
		µRWell	UVA, GWU, MIT, EIC-China, EIC-Korea, BNL	GEM construction for SBS; µRWell prototyping and testing at Fermilab
		AC-LGAD	RICE, ORNL, BNL, UTSM	Experience in CMS
	PID	hpDIRC	CUA, GSI, ODU, W&M, MIT/BATES	Design and construction (PANDA, GlueX), simulations
	EM Calorimetry	SciGlass	CUA, MIT, KU, Augustana, Ohio U., UC Boulder, UIUC, U. Regina	Glass fabrication and characterization, detector design and construction, technical support, simulations
	Hadron Calorimetry	Scintillating tiles (sPHENIX Reuse)	ISU, GSU	sPHENIX Construction

Region	System	Technology	Institutions	Experience / Comments
Backward Endcap (e⁻ direction)	Tracking	ITS-3 Si Disks	LANL, LBL, ORNL, MIT/BATES, EIC-China, EIC-Taiwan, EIC-Korea, Brunel (UK), Regina (Canada), Czech. Tech. Univ., BNL	Experience constructing previous Si trackers, most recently for sPhenix.
	PID	AC-LGAD	RICE, ORNL, BNL, UTSM	Experience in CMS
		mRICH	GSU, JLab	GSU originated mRICH concept and led its design
	EM Calorimetry	PbWO4	AANL/Armenia, CUA, Charles U./Prague, FIU, IJCLab-Orsay/France, JLab, JMU, MIT, Lehigh U., UKY, Ohio U.	Experience with crystal fabrication and characterization, detector design and construction, technical support and infrastructure, readout electronics, simulations (Hall C EMCal & NPS, STAR ECAL)
Far-Forward	B0	AC-LGAD Tracking	UH, U. Kansas	ZDC at LHC, Roman Pots, fast timing
		PWO4 Calorimeter	EIC-Israel	EM calorimetry, ZDC at LHC
	Off-momentum Detectors	AC-LGAD Tracking	UH, U. Kansas	Fast timing, tracking experience at RHIC, LHC
	Roman Pots	AC-LGAD Tracking	IJCLab-Orsay/France, BNL, UH, U. Kansas, BNL	ASIC readout of AC-LGAD (OMEGA, ATLAS)
	ZDC	PWO, W/Si, Pb/Si, Pb/Sci	EIC-Japan, KU	Experience with LHCf, RHICf development of FOCAL
Far-Backward	Low-Q^2 Detector	AC-LGAD Tracking	York U. Glasgow U.	Experience from CLAS12 tagger
		PWO4 Calorimeter	EIC-Israel	EM calorimetry, ZDC at LHC
	Luminosity Monitor	AC-LGAD Tracking	York U. Glasgow U.	Experience from CLAS12 tagger
		PWO4 Calorimeter	EIC-Israel	EM calorimetry, ZDC at LHC
Electronics	Streaming readout electronics, Data Aggregation Modules		Columbia, ISU, UC Boulder, OU, ORNL, LLNL, UNH	Electronics expertise at RHIC, JLab
DAQ / Computing	Streaming DAQ, Online Event Filter		CNU, ISU, MIT, LLNL, Morehead state, ORNL, PNNL, SBU, UC Boulder, UConn	Experience with sPHENIX streaming DAQ; CMS and GlueX computing

Figure 4.2: Planed responsibilities of the ECCE institutions for the production of different detector sub-systems.

Chapter 5: Cost and Schedule

5.1 Cost Estimate

The combined ECCE cost estimate is summarized in Table 5.1. This cost estimate is based on a bottom-up estimate from the scientists and engineers collaborating in the ECCE consortium. The methodology used in generating the cost estimate follows the best practices for a DOE 413.3b project. In conjunction with project management professionals from Oak Ridge National Laboratory (ORNL), cost and schedule estimates were developed based on expert input for each subsystem and used as input to a Work Breakdown Structure (WBS) in Primavera P6. We used the same labor categories and cost rates in P6 as was requested by the project. All costs are calculated in 2021 dollars, and no escalation or overhead factors were applied. A fully-loaded WBS structure was developed for each costed category, along with documentation on the basis of estimate, project narratives, and risk and opportunity logs. Advice from project professionals and experienced scientists and engineers was used to inform all aspects of the WBS. The project input and documentation was reviewed regularly with the subsystem experts, project professionals, and Steering Committee as it was developed. A full cost and schedule review was held with external input from outside project professionals at ORNL that were not involved in the development of the ECCE project plan. By using P6 we were able to export the Excel spreadsheets for each costed category in the format requested by the EIC project as direct outputs from the P6 project plan. In this way we were able to develop the ECCE project plan making use of modern planning tools in a way that still allowed us to produce cost and schedule information in the format requested in the call for proposals. The complete project estimate documentation, including the full WBS, WBS dictionary, subsystem narratives, and risk registry are available as part of the ECCE supplementary material [42]. The full ECCE project plan is logically tied and driven, and it contains over 1250 discrete activities and over 250 milestones.

As can be seen in Table 5.1, the on-project cost is estimated to be \$162.0M for materials and labor combined, while the total estimated cost of ECCE is \$220.1M. The total in-kind contribution (including reuse) to the ECCE project total is \$58.1M, materials and labor combined. We detail the breakdown between equipment reuse and new in-kind contributions in Section 5.3 below. If ECCE is selected as the project detector by the proposal review process, there will be substantial opportunities to recruit additional in-kind contributions to ECCE as the community re-aligns, further lowering the on-project cost of ECCE. More detailed information on the costs included in each category are provided below.

Tracking: This category incorporates the charged particle tracking detectors in the central barrel and forward/backward directions. The estimate for the Si tracker was completed by fully utilizing the cost and schedule data provided by the EIC Silicon Consortium (EICSC). The detector geometry of the ECCE design is the same as the EICSC hybrid design in the barrel with five layers (three vertex and two sagitta). The disc location and design is similar between the ECCE and EICSC designs, and there is a less than 10% variation of the silicon disc costs between the two designs. The only significant change in the ECCE design is in the electron going direction, which consists of four discs in ECCE instead of five discs as proposed by the EICSC. In our estimate we use the same cost and schedule provided by the EICSC for the five-disc electron endcap, as removing one endcap is not a simple scaling of the EICSC-provided data. For in-kind contributions, we have engaged three module assembly and testing sites in China, South Korea and Taiwan and two chip probe stations in Korea, which helps mitigate the on-project costs. We have also added the cost of CMM machines for all US sites responsible for the production of staves and discs.

The estimate for the μRWELL inner and outer barrel trackers was developed by subsystem experts. Seoul National University has extensive expertise in the production of large-area MPGD foils and will partner with institutions in China (CIAE, IMP and USTC) with expertise in the required DLC coating to produce the μRWELL foils, which will be provided as an in-kind contribution.

Table 5.1: Summary of the ECCE detector cost estimate in 2021 USD at Level-3 for detector categories, and Level-2 for all other categories. Entries are rounded to the nearest $0.1M separately. For Detector Infrastructure, only the in-kind contributions for re-use were costed in detail, including the on-project costs for refurbishment. The remaining costs were calculated assuming the EIC project estimate for the total cost in this category (a total of $26.4M for this category).

Category	In-Kind ($M)	On-Project ($M)	Total ($M)
Tracking	**6.7**	**20.2**	**26.8**
Inner Barrel μRWELL	0.5	1.5	2.0
Outer Barrel μRWELL	0.5	2.0	2.4
Si Tracker	5.7	16.7	22.4
Particle ID	**6.1**	**28.1**	**34.2**
hpDIRC	5.5	8.2	13.7
mRICH	0.1	3.0	3.1
dRICH	0.2	7.0	7.2
AC-LGAD TOF	0.3	9.9	10.1
EM Calorimetry	**7.4**	**21.0**	**28.4**
Barrel	1.5	15.1	16.6
Electron Endcap	3.7	5.2	8.8
Hadron Endcap	2.2	0.7	2.9
Hadronic Calorimetry	**10.0**	**13.3**	**23.3**
Barrel	10.0	3.5	13.5
Hadron Endcap	0.0	9.8	9.8
Magnet	**9.0**	**3.4**	**12.4**
BaBar Solenoid	9.0	0.9	9.9
Replacement Magnet Design	0.0	1.3	1.3
Valve Box	0.0	0.4	0.4
Cryo Line	0.0	0.8	0.8
Electronics	**2.7**	**18.9**	**21.6**
DAQ/Computing	**1.2**	**6.0**	**7.2**
Detector Infrastructure (reuse only)	**3.9**	**1.1**	**5.0**
Auxiliary Detectors	**10.3**	**0.4**	**10.8**
Roman Pots	0.0	0.4	0.4
Off-Momentum Detector	1.2	0.0	1.2
B0 Detector	1.1	0.0	1.1
ZDC	7.0	0.0	7.0
Low-Q^2 Tagger	1.1	0.0	1.1
Luminosity Monitor	**0.8**	**0.0**	**0.8**
Subtotal for Costed Categories	**58.1**	**112.4**	**170.5**
Detector Management	0.0	7.4	7.4
Detector R&D	0.0	12.1	12.1
Detector Infrastructure (remainder not costed)	0.0	21.4	21.4
Pre-Ops and Commissioning	0.0	8.7	8.7
TOTAL	**58.1**	**162.0**	**220.1**

Particle ID: The Particle Identification category incorporates all particle ID detectors. In the central barrel this includes the high-performance DIRC (hpDIRC) and the AC-LGAD TOF barrel layer, while the backwards direction includes the modular RICH and the forward direction includes the dual-radiator RICH. AC-LGAD TOF layers in the forward and backwards direction were also included. These estimates were developed by subsystem experts. The hpDIRC will reuse the BaBar DIRC quartz bars, resulting in a significant reduction of on-project cost.

EM Calorimetry: This category includes all electromagnetic calorimetry in the ECCE detectors. This includes electromagnetic calorimetry in the forward and backwards directions as well as the central barrel. The backwards electromagnetic calorimetry estimate was developed by the Electron Encdcap Electromagnetic Calorimetry (EEEMCal) consortium. The estimate for the barrel for forward electromagnetic calorimetry was developed by ECCE subsystem experts. The forward electromagnetic calorimeter is a substantial in-kind contribution from our Korean collaborators. The PWO crystals for the electron endcap electromagnetic calorimeter and the scintillating glass for the barrel electromagnetic calorimeter are both long lead time procurement items; see Section 5.5.

Hadronic Calorimetry: A major component of the Hadronic Calorimetry category includes the reuse of the sPHENIX outer hadronic calorimeter, which also serves as the magnet flux return for the experiment. The estimate for the in-kind value of the sPHENIX hadronic calorimeter was developed based on the actual costs from the sPHENIX project. This category also includes the longitudinally-segmented forward hadronic calorimeter, the estimate for which was developed by subsystem experts. The scintillating tiles for the longitudinally segmented hadronic calorimeter is a long lead time procurement item; see Section 5.5.

Magnet: As noted in Section 2.10, in addition to refurbishing the existing BaBar solenoid for use in ECCE, we mitigate potential schedule risk by including the cost for a replacement magnet design that will be developed in parallel with evaluation of the BaBar solenoid during sPHENIX operations. This category was developed in conjunction with magnet engineers and physicists at JLAB. The in-kind value resulting from the re-use of the BaBar magnet was developed by using the data available in literature for the cost of a magnet with similar specifications [112] (see also the supplemental documentation [42]).

Electronics: As requested by the project, the detector costing category ends at the photon sensors for the detectors. All readout electronics, power supplies, and Data Aggregation Modules (DAM) are included in the electronics category. Each subsystem is costed based on a conceptual design of a readout compatible with a fully streaming readout architecture. For calorimetry systems, we plan to develop a common digitizer based on the sPHENIX design. For digital detector systems, like AC-LGAD based detectors and the Si tracker, the readout systems are included in the detector subsystems and this category only includes the required DAM boards. The PID detectors take advantage of either existing ASICs or designs that are currently being developed for other experiments. There are currently no ECCE-specific ASICS in our project plan, although we note that several systems (such as AC-LGADs) require substantial further development. This category was developed by electronics experts in conjunction with detector subsystem experts. The in-kind contributions in Electronics includes the contribution from Korean institutions for the electronics to support the hadron endcap electromagnetic calorimeter.

DAQ/Computing: This category includes costs for a fully streaming readout architecture planned for ECCE, as described in Section 2.7. This includes the Event Buffer and Data Compression (EBDC) interface machines, Online Event Filter hardware, network switch, and timing system. The DAM boards, which reside in the EBDC machines and receive data from the front-end systems are costed in the Electronics category (see Section 2.7 for an overview). This category was developed based by DAQ experts based on similar costs in the sPHENIX data acquisition system.

Detector Infrastructure: For the Detector Infrastructure category we provide detailed costing on the in-kind contributions from reuse of existing experimental equipment, including on-project costs associated with reuse, but do not provide detailed costing for all items in this category, following guidance from the EIC project. Significant reuse of sPHENIX infrastructure, including the magnet pedestal base, flux return plug door in the backwards direction, and gas mixing house are anticipated. In Table 5.1 we tabulate this category in two rows. The first row, as part of the costed categories, tabulates the in-kind and on-project costs associated with reuse *only*. The second row in the uncosted expenses lists the remaining on-project

expenditures, assuming the EIC project estimate for the total value of both rows of $26.4M.

Auxiliary Detectors: The auxiliary detectors category includes all instrumentation in the forward and backward beamlines, including the roman pot and off-momentum detectors, the B0 magnet spectrometer, the zero-degree calorimeter, and the low-Q^2 tagger. The cost estimate for the section was developed by subsystem experts, with substantial international contributions from Israel and Japan.

Luminosity Monitor: This category includes the luminosity monitor in the backwards direction. The cost estimate for the section was developed by subsystem experts, with substantial contributions from international collaborators. The luminosity monitor is an in-kind contribution from the United Kingdom.

Detector Management: The Detector Management category incorporates the level-of-effort engineering and travel support for oversight, systems integration, and quality assurance. Detailed cost estimates were not requested for Detector Management, and in calculating the total cost we use the EIC project estimate. However, we felt that quantifying this category was necessary to ensure proper level-of-effort engineering support, management and travel when developing the detailed subsystem estimates and a bottom-up estimate for the Detector Management category is included in the supplementary material [42]. Our independent estimate for the Detector Management category is consistent with the estimate provided by the EIC project.

Detector R&D: Detector R&D incorporates the R&D efforts specific to the ECCE detector that will be required required prior to construction of the ECCE detector subsystems. This incorporates significant R&D for development of the Si tracker, cylindrical μRWELL detectors, PID detector sensor selection, and AC-LGAD sensor characterization and readout. The charge by the project was to evaluate the EIC R&D plan [113] and determine if the resources provided in that plan were sufficient. A detailed breakdown of the ECCE R&D needs are discussed in Section 5.2. In Table 5.1 we list total amount allocated in the EIC R&D plan for detector R&D.

Pre-Ops and Commissioning: The Pre-Operations and Commissioning category includes the activities necessary to test and integrate the full detector prior to data-taking operations. A detailed cost breakdown was not requested for this category. We assume the estimate from the EIC project for this category in calculating the total cost in Table 5.1.

For all of the detector categories, the cost and schedule estimates cover the production of the detector subsystems, from pre-production prototypes through production of the detector assemblies. They do not include installation of the subsystem in the full ECCE detector, but do include any specialized fixtures or tooling that would be required for assembly and installation, with the exception of the BaBar solenoid and the oHCAL for which such tooling already exists.

The source of the basis of estimate for the full project is shown in Figure 5.1 (left). The relatively high fraction in the category of Historical Costs is driven by the extensive reuse of existing equipment in the ECCE proposal, while expert opinions and engineering estimates account for the majority of the remainder. In some cases, vendor quotes were solicited when appropriate preliminary designs were available.

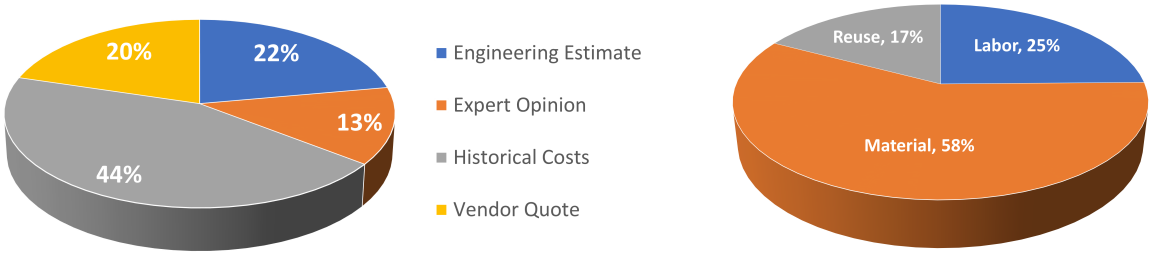

Figure 5.1: LEFT: A breakdown of the overall basis of estimate for the ECCE proposal, excluding reuse. RIGHT: A breakdown of the ECCE project cost by reuse, labor and materials.

A breakdown of materials versus labor on the overall ECCE project is shown in Figure 5.1 (right). In this figure the reuse contribution been separated to allow a more accurate comparison between the ratio of labor to new materials on the project. reuse of existing experimental equipment accounts for a significant fraction of the overall ECCE cost (17%), while labor and materials account for 25% and 58% of the total cost, respectively. It should be noted that the costed categories do not include either the level-of-effort engineering and oversight required for each of the detector subsystems (this is in the Detector Management category), nor does it include the labor associated with the assembly and integration of the full ECCE detector, which is a substantial amount of labor that is not included in this breakdown. The materials costs in the detector categories skew towards a larger fraction of the total cost due to the selection of detector technologies for calorimetry and PID that require relatively large investments in their active elements relative to the labor required to assemble them. The combination of these two factors results in the relatively high materials costs relative to labor in Figure 5.1. The reuse, labor and materials breakdown for each of the costed categories individually is shown in Figure 5.2.

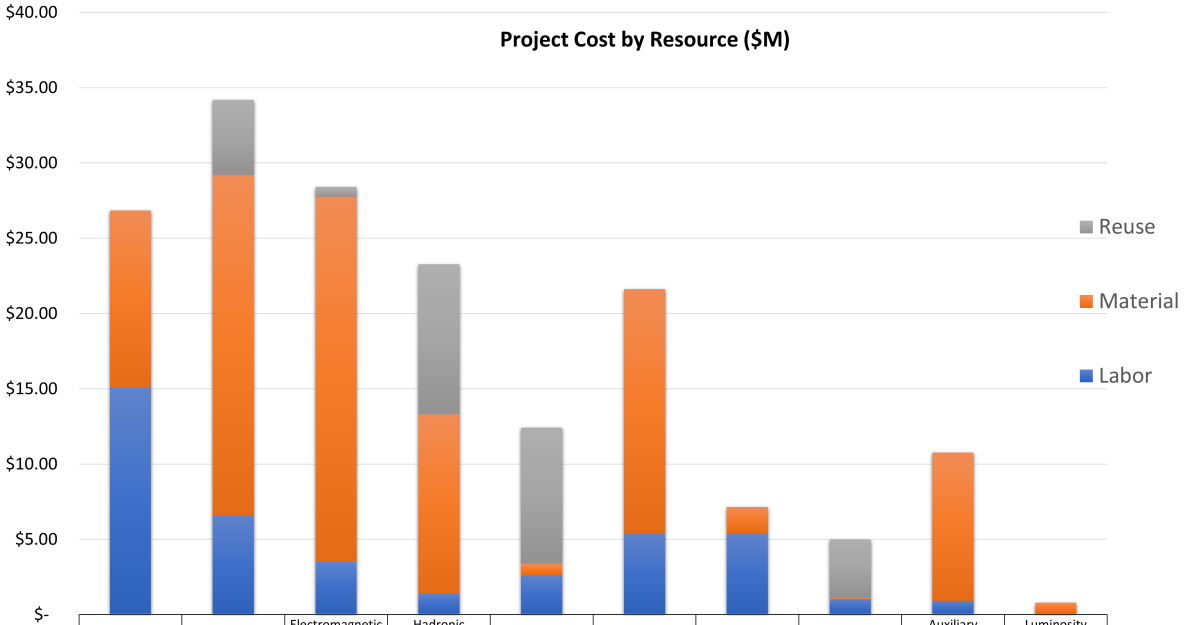

	Tracking	PID	Electromagnetic Calorimetry	Hadronic Calorimetry	Magnet	DAQ/Computing	Electronics	Infrastructure	Auxiliary Detectors	Luminosity Monitor
Reuse	$-	$5.0	$0.7	$10.0	$9.0	$-	$-	$3.9	$-	$-
Material	$11.8	$22.6	$24.2	$11.9	$0.8	$16.3	$1.8	$0.1	$9.9	$0.7
Labor	$15.1	$6.6	$3.5	$1.4	$2.6	$5.4	$5.4	$1.0	$0.9	$0.1

Figure 5.2: Labor, materials and reuse breakdown by costed categories. The Detector Infrastructure category only includes reuse items, along with the labor and materials required to refurbish them for use in ECCE.

5.2 Detector R&D Needs

The project charged the detector proposals with evaluating the EIC Detector R&D plan [113] to determine if the resources in the plan were sufficient for the needs of the ECCE detector. To accomplish this, the ECCE subsystem experts enumerated their R&D requirements in a detailed list of resource-loaded activities that have been added to the ECCE project plan. Consistent with the EIC R&D plan these activities are only broken out with FY granularity (from FY22-26), but still provide guidance to the overall needs of ECCE. In many cases, these activities are consistent with the input provided to the EIC project in the development of the R&D plan. In some cases, there was additional input beyond the EIC R&D plan based on changing priorities since the R&D plan was developed. The timing of the completion of these activities is also used to inform the schedule planning in Section 5.5 as the starting milestones for detector prototyping and construction

Table 5.2: Detector R&D costs evaluated specifically for the ECCE detector.

Equipment	In-Kind Value ($M)	On-Project Costs ($M)	Notes:
Cylindrical μRWELL	0.0	0.7	per ECCE experts
Si Sensor Development	6.0	3.9	per EICSC consortium
Si Additional R&D (Targeted)	1.0	1.8	per EICSC consortium
AC-LGADs	0.0	1.2	consistent with EIC R&D plan
PID	0.2	1.9	consistent with EIC R&D plan
EM Calorimetry (SciGlass and crystals)	0.2	0.2	consistent with EIC R&D plan in-kind from EEEMCal consortium
EM Calorimetry (Shashlik)	0.0	0.2	consistent with EIC R&D plan
Hadronic Calorimetry (forward)	0.0	0.4	consistent with EIC R&D plan
Electronics/ASICS	0.0	1.7	consistent with EIC R&D plan
Aux. Detectors	0.0	0.4	consistent with EIC R&D plan
TOTAL	**7.4**	**12.4**	

activities in the subsystem WBS categories.

In evaluating R&D costs for the Si tracker, we rely on input from the EICSC that provided tasks, materials costs, and labor hours by resource type. To maintain consistency with project guidance, we cost labor hours at the rates provided by the project for each labor category. Following EICSC guidance, we assume a 50/50 split for in-kind versus on-project labor for silicon designer, electrical engineer, mechanical engineer for sensor development, and 100% on-project for non-sensor activities. Staff labor and postdoc labor associated the Lawrence Berkeley National Laboratory are costed as on-project, consistent with project guidance, while student labor is assumed to come from EICSC collaborating universities and therefore is costed as an in-kind contribution.

It is important to note that as little as a year ago it was not clear to the EIC community that MAPS/ITS3 at 64 nm was sufficiently mature for an EIC detector. The EIC R&D plan did not include Si sensor development. The information received from the EICSC is a clear indication that additional resources for Si tracking are required beyond those allocated in the EIC R&D plan to make ITS3 technology viable for an EIC detector.

A summary of the specific ECCE R&D needs is contained in Table 5.2. The total of on-project R&D costs is $12.4M, consistent with the $12.1M allocated in the EIC R&D plan. In addition, there are substantial in-kind contributions of $7.4M, mostly associated with the Si sensor development, that offset the higher total R&D costs ($19.8M) than assumed in Table 5.1.

5.3 Equipment Reuse and In-Kind Contributions

A breakdown of the in-kind contributions to the ECCE detector is shown in Figure 5.3. Half of the ECCE in-kind contribution in Table 5.1 can be seen to come from the reuse of existing experimental equipment, followed by in-kind contributions of material and labor from the ECCE consortium institutions. In Table 5.3 we list the major items of experimental equipment planned for reuse in the ECCE detector and their source,

Table 5.3: Major items of experimental equipment to be reused in the ECCE detector along with their source, in-kind value in 2021 USD, and the on-project costs associated with refurbishment and preparation for reuse. In the case of the PWO crystals, the labor required to refurbish the material is also an in-kind contribution.

Equipment	Source	In-Kind Value ($M)	On-Project Costs ($M)
BaBar Solenoid	BNL	9.0	2.9
sPHENIX Experiment Pedestal, Backwards Flux Return, Gas Mixing House	BNL	3.9	1.0
sPHENIX Outer Hadronic Calorimeter	BNL	10.0	0.3
PWO Crystals	JLab	0.7	0.0
BaBar DIRC quartz bars	SLAC	5.0	0.3
TOTAL		**28.6**	**4.5**

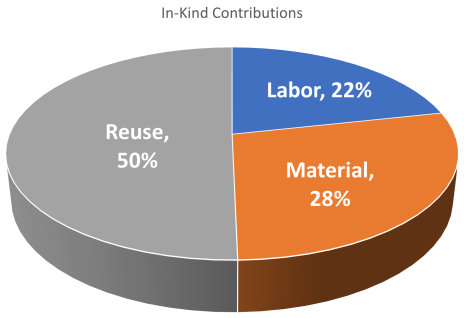

Figure 5.3: The breakdown of in-kind contributions between reuse, in-kind materials, and in-kind labor.

along with their in-kind value and the associated on-project costs for refurbishment and reuse. The total in-kind value associated with the reuse of experimental equipment is $28.6M in 2021 USD, while the *net* value (contribution minus on-project costs for refurbishment, etc.) is $24.1M.

Table 5.4 lists the in-kind contributions from international collaborators. All of these contributions are formalized in Expression of Intent memoranda negotiated with the ECCE Steering Committee. These letters are available in the supplemental project material [42] provided to the committee. In-kind contributions represent a significant commitment to the ECCE detector and the EIC science program by our international partners, totaling $18.2M in 2021 USD. Significant international commitments include:

- Substantial contributions to the electron endcap calorimeter materials and construction have been made available by the EEEMCal consortium
- The Si Tracker includes substantial in-kind labor contributions from the EICSC consortium ($3.1M). There is no guidance from the EICSC on what fraction of these contributions could come from international collaborators, but we anticipate it could be substantial. We do **not** include this in-kind labor in Table 5.4.
- International collaborators will provide sensor module assembly sites in Korea, China and Taiwan. Korea will also provide sensor probe capabilities.
- The forward electromagnetic calorimeter and electronics are a contribution from the EIC-Korea institutions, in collaboration with RIKEN (Japan)
- Foils for the the μRWELL detectors will be provided by Seoul National University, in collaboration

with institutions in China (CIAE, IMP and USTC) which will provide the technology for the DLC resistive coating

- The Zero Degree Calorimeter (ZDC), along with associated electronics, are an in-kind contribution of the EIC-Japan institutions
- Much of the far-forward instrumentation, including the off-momentum detector, B0 spectrometer, and luminosity monitor will be provided by a consortium of Israeli institutions
- The low-Q^2 tagger is an in-kind contribution from the University of Glasgow and the University of York in the United Kingdom

Table 5.4: International in-kind contributions to the ECCE detector.

Contribution	**International Partners**	**In-Kind Value ($M)**
FEMC Detector and Electronics	Korea, Japan	2.7
μRWELL foils/boards	Korea, China	0.4
Si Tracker Module Assembly Sites (probe test, tooling, labor)	Korea, China, Taiwan	2.6
ZDC Detector and Electronics	Japan	7.0
Off-Momentum Detector B0 Spectrometer Luminosity Monitor	Israel	3.2
PWO Crystals (EEEMCal Consortium)	Czech. Republic (Charles U./Prague)	0.6
EEEMC Materials, Construction and Mechanical Design (EEEMCal Consortium)	Armenia, IN2P3/France	1.0
dRICH Mechanical Engineering	UTSFM (Chile)	0.2
Low-Q^2 Tagger	UK (Glasgow/York)	1.1
TOTAL		**18.8**

A breakdown of the in-kind labor by costed category and labor resource is shown in Figure 5.4 as Full Time Equivalents (FTE). This labor is contributed by ECCE consortium members, integrated over the lifetime of the ECCE project. The total value of in-kind labor contributed to the ECCE project is $19.8M in 2021 USD (note that some of this in-kind labor overlaps with the international in-kind contributions in Table 5.4). The largest contribution of in-kind FTE's in ECCE are for the Si Tracker and the electron endcap electromagnetic calorimeter, both of which are supported by large multi-institution consortia that support the respective detector subsystems. The contributed in-kind labor on the ECCE project is well within the capabilities of the ECCE consortium based on the original Expression of Intent letter from November 2020, as well as updated information from gathered from collaborators who have joined after the letter of intent. For example, integrated over five years more than 125 postdoc FTE's have been pledged by ECCE consortium members, well in excess of the postdoc in-kind FTE's incorporated in the the project plan.

In-Kind FTEs by Subsystem

Subsystem	Electrical Designer	Electrical Engineer	Electrical Tech	Mechanical Designer	Mechanical Engineer	Mechanical Tech	PhD Student	PostDoc	Other	Scientist	Undergrad	Software Expert	Total FTE's
ECE06.10.03 Tracking	0.0	0.9	2.6	0.0	0.6	2.4	8.0	11.6	0.0	5.1	0.0	0.0	**31.1**
ECE06.10.04 PID	0.0	0.0	0.0	0.9	0.0	0.3	6.2	0.2	0.0	1.8	1.3	0.0	**10.6**
ECE06.10.05 Electromagnetic Calorimetry	0.0	0.4	0.0	1.0	0.6	1.3	9.8	13.3	0.0	0.0	6.9	0.0	**33.2**
ECE06.10.08 Electronics	1.0	2.3	1.7	0.0	0.0	0.0	0.0	0.0	0.3	3.8	0.0	0.0	**9.0**
ECE06.10.09 DAQ/Computing	0.0	0.0	0.2	0.0	0.0	0.0	0.2	0.1	0.0	1.8	0.0	1.9	**4.2**
ECE06.10.11 Auxiliary Detectors	0.3	1.2	0.3	0.1	0.2	0.2	0.7	0.3	0.0	0.3	0.3	0.0	**4.0**
ECE06.10.14 Luminosity Monitor	0.0	0.1	0.0	0.0	0.3	0.0	0.0	0.0	0.0	0.0	0.0	0.0	**0.4**
Totals	**1.3**	**4.9**	**4.8**	**2.0**	**1.7**	**4.1**	**24.9**	**25.6**	**0.3**	**12.8**	**8.5**	**1.9**	**92.6**

Figure 5.4: In-kind labor contributions to ECCE in FTE's for various labor categories, integrated over the project lifetime. An FTE is assumed to correspond to 1760 labor hours. Unlisted WBS categories have no in-kind labor contributions.

5.4 Risk

While the ECCE detector design seeks to minimize risk through strategic re-use and the selection of mature detector technologies, there are nevertheless risks associated with some ECCE detector technology choices, as well risks associated with cost and schedule performance. Our approach has been to clearly identify these risks and develop an appropriate mitigation strategy, either through developing alternatives should the risks be realized or eliminating risk through an aggressive R&D program. We have developed an extensive risk registry for the ECCE proposal that includes risk impact, likelihood and mitigation strategy for a wide array of technical and cost & schedule risks. A detailed discussion of the risks and opportunities associated with the selected detector technologies is available in Section 2.10. The full risk and opportunity registry is available as part of the ECCE supplemental material [42].

5.5 Schedule

The ECCE schedule is entirely logic-driven based on the activities, resources, duration and relationships within the Primavera P6 project plan. Project dependencies are informed by the EIC project CD milestones as well as the relevant R&D milestones for each detector subsystem. The start of detector prototyping is keyed to the completion of the relevant detector R&D and the project CD-3 milestone, which was taken to be March 1, 2024. The schedule for each detector subsystem then proceeds based on the internal relationships between detector activities. For each subsystem category this results in a technically-driven completion date for the subsystem activity, as shown in Figure 5.5 and Figure 5.6. The technically driven milestones for the completion of subsystems production range between Q2FY26 and Q2FY29, with the last subsystem completed 17 calendar months prior to the anticipated EIC early CD-4A date. While a full detector assembly schedule is beyond the scope of this proposal, we believe that that it is a reasonable expectation that the current ECCE project plan is compatible with the EIC early CD-4A date.

The ECCE project schedule informs and identifies the need for long lead-time procurements at CD-3A, as listed in Table 5.5. At the present time, we anticipate the need for only three long-lead procurement items, all associated with the ECCE calorimetry systems. The Scintillating Glass (SciGlass) for the barrel electromagnetic calorimeter, PWO crystals for the backward electromagnetic calorimeter, and the scintillating tiles for the forward hadronic calorimeter are large orders with long lead times for delivery.

In Figure 5.7 we present a technically-driven cost profile for the overall ECCE project, based on the activity costs and schedule information in the ECCE project plan. This does not include Detector Management, Detector R&D, or Pre-Operations and Commissioning categories, as complete cost and schedule data was

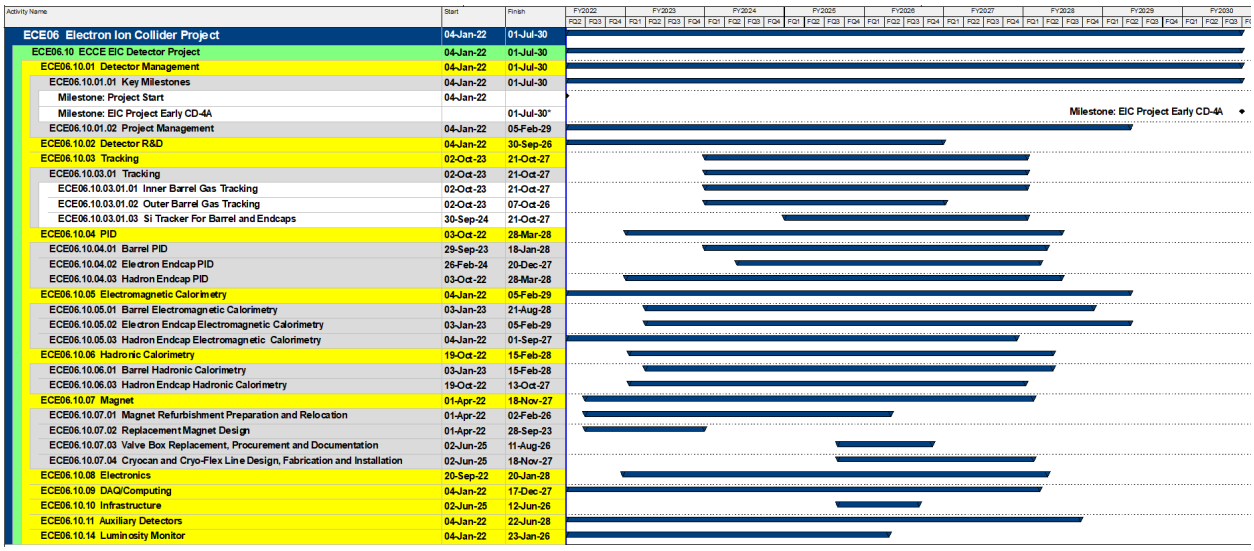

Figure 5.5: GANTT chart for the ECCE subsystem schedule from Primavera P6.

Table 5.5: Long-lead procurements identified by the ECCE project plan and schedule. We anticipate that these procurements will be required to complete the ECCE detector scope by the EIC early CD-4a milestone.

CD-3A Long-Lead Item:	Cost ($M)
Forward Hadronic Calorimetry Scintillating Tiles	2.7
Backward EMCal PWO Crystals	4.7
Barrel EMCal SciGlass	12.3
TOTAL	**19.7**

not generated for these categories. For the Detector Infrastructure category, only the reuse contributions (in-kind and associated on-project expenses) are included.

In Figure 5.8 we present an FTE profile for in-kind and on-project labor resources. A breakdown of both in-kind and on-project labor by resource type is shown in Figure 5.9. In-kind labor contributions are drawn from the members of the ECCE consortium, and were developed from consortium input based on the interests and commitments of ECCE members. In particular, the ECCE in-kind labor contribution does *not* assume an increase in funding from the DOE or NSF University programs, but assumes a constant level of effort based on current levels. These commitments represent a redirection of existing effort as the field moves to the EIC. Labor contributed from national laboratories to the ECCE proposal (exclusive of LDRD contributions) is counted as on-project for this costing exercise, consistent with guidance from the EIC project. More information on the in-kind labor contribution to ECCE is available in Section 5.3, and detailed breakdowns of the in-kind and on-project labor by subsystem are available in the ECCE supplemental material [42].

Technically-driven cost profiles broken down by subsystem categories are available in the supplemental documentation.

WBS	Projected Completion	Months Prior to Early CD-4A
ECE06.10.03 Tracking	**Q1FY28**	**32.8**
ECE06.10.03.01.01 Inner Barrel Gas Tracking	Q1FY28	32.8
ECE06.10.03.01.02 Outer Barrel Gas Tracking	Q1FY27	45.4
ECE06.10.03.01.03 Si Tracker For Barrel and Endcaps	Q4FY27	32.8
ECE06.10.04 PID	**Q2FY28**	**27.5**
ECE06.10.04.01 Barrel PID	Q2FY28	29.8
ECE06.10.04.02 Electron Endcap PID	Q1FY28	30.8
ECE06.10.04.03 Hadron Endcap PID	Q2FY28	27.5
ECE06.10.05 Electromagnetic Calorimetry	**Q2FY29**	**17.0**
ECE06.10.05.01 Barrel Electromagnetic Calorimetry	Q4FY28	22.6
ECE06.10.05.02 Electron Endcap Electromagnetic Calorimetry	Q2FY29	17.0
ECE06.10.05.03 Hadron Endcap Electromagnetic Calorimetry	Q4FY27	34.5
ECE06.10.06 Hadronic Calorimetry	**Q2FY28**	**28.9**
ECE06.10.06.01 Barrel Hadronic Calorimetry	Q2FY28	28.9
ECE06.10.06.03 Hadron Endcap Hadronic Calorimetry	Q1FY28	33.1
ECE06.10.07 Magnet	**Q1FY28**	**31.9**
ECE06.10.08 Electronics	**Q2FY28**	**29.8**
ECE06.10.09 DAQ/Computing	**Q1FY28**	**30.9**
ECE06.10.10 Infrastructure	**Q3FY26**	**49.3**
ECE06.10.11 Auxiliary Detectors	**Q3FY28**	**24.6**
ECE06.10.11.01 Roman Pots	Q4FY26	45.7
ECE06.10.11.02 Off Momentum detectors (OMD)	Q3FY27	37.1
ECE06.10.11.03 B0 Detector	Q3FY26	51.6
ECE06.10.11.04 Zero Degree Calorimeter (ZDC)	Q3FY28	24.6
ECE06.10.11.05 Low Q2 Tagger	Q2FY26	52.0
ECE06.10.14 Luminosity Monitor	**Q2FY26**	**54.0**

Figure 5.6: Estimated subsystem completion dates assuming a technically-driven schedule, based on the ECCE schedule input data. These dates mark the completion of subsystem construction and readiness for installation in the full ECCE detector.

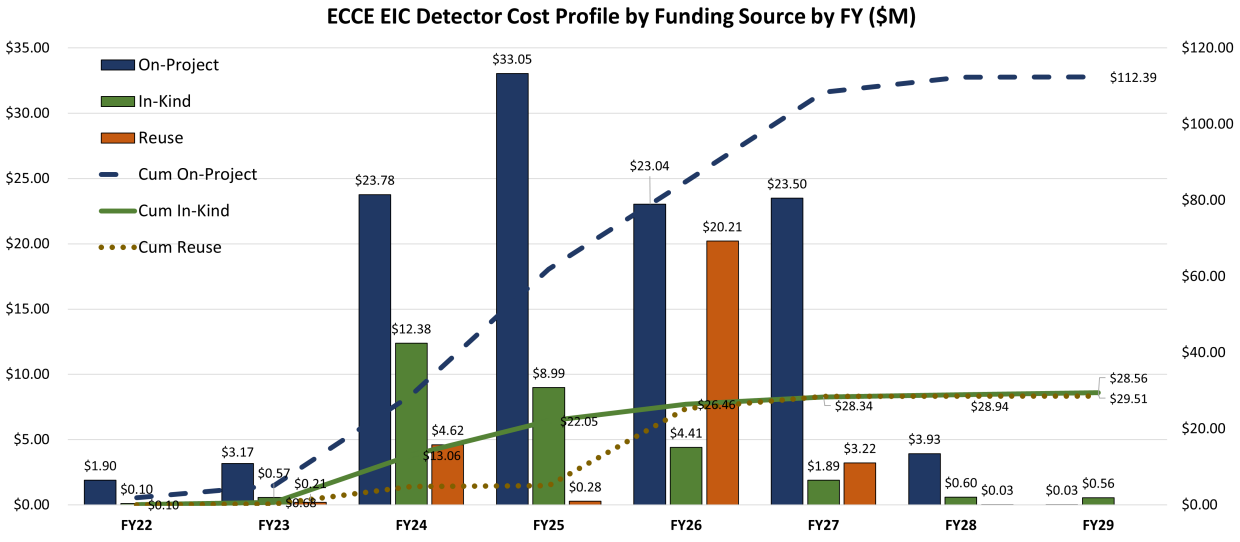

Figure 5.7: Technically-driven cost profile for all costed categories. In this profile the reuse contributions are shown separately from the remainder of the in-kind contributions.

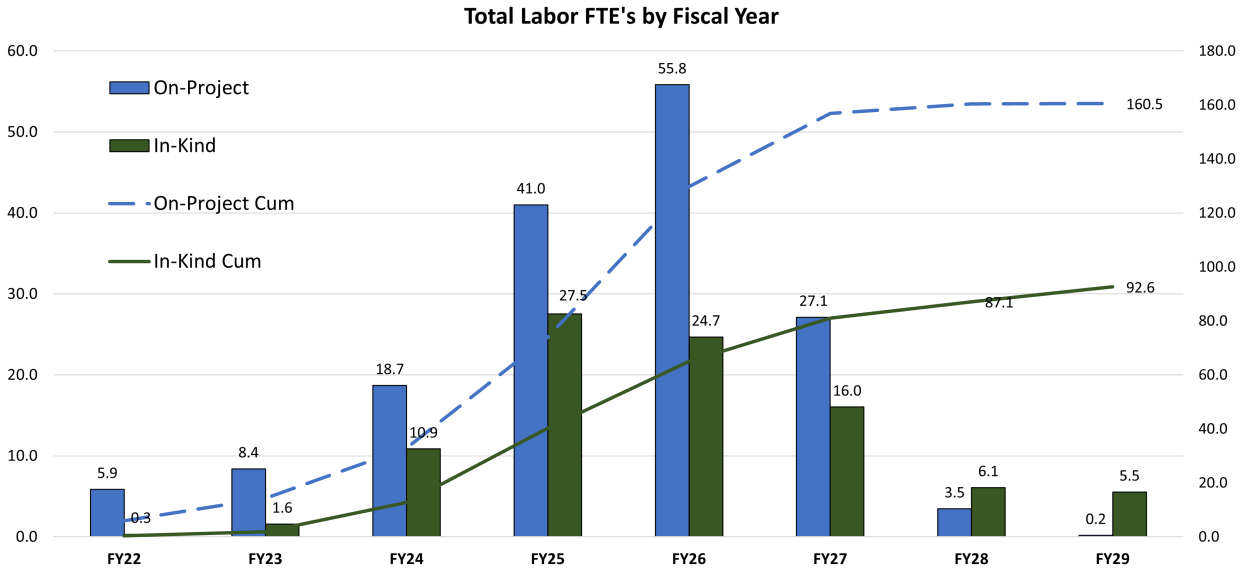

Figure 5.8: Technically-driven FTE profile broken out by in-kind and on-project resources, for all costed categories.

In-Kind Labor FTE's									
Labor Group	**FY22**	**FY23**	**FY24**	**FY25**	**FY26**	**FY27**	**FY28**	**FY29**	**Total FTE's**
Electrical Designer	0.00	0.12	0.56	0.43	0.20	0.00	0.00	0.00	1.3
Electrical Engineer	0.00	0.90	2.11	1.23	0.16	0.47	0.06	0.00	4.9
Electrical Tech	0.20	0.00	0.23	2.58	0.97	0.83	0.00	0.00	4.8
Mechanical Designer	0.00	0.09	0.05	0.96	0.91	0.00	0.00	0.00	2.0
Mechanical Engineer	0.09	0.10	0.23	1.16	0.07	0.00	0.00	0.00	1.7
Mechanical Tech	0.00	0.00	0.04	2.39	0.71	0.26	0.00	0.73	4.1
Other	0.00	0.00	0.25	0.00	0.00	0.00	0.00	0.00	0.3
PhD Student	0.03	0.22	1.78	4.63	8.74	5.89	1.92	1.65	24.9
PostDoc	0.00	0.14	1.80	5.95	7.20	4.77	3.20	2.51	25.6
Scientist	0.00	0.00	3.02	3.93	4.07	1.69	0.05	0.00	12.8
Software Expert	0.00	0.00	0.44	0.98	0.45	0.00	0.00	0.00	1.9
Undergrad	0.00	0.00	0.35	3.31	1.20	2.11	0.86	0.65	8.5
Grand Totals	**0.3**	**1.6**	**10.9**	**27.5**	**24.7**	**16.0**	**6.1**	**5.5**	**92.6**

On-Project Labor FTE's									
Labor Group	**FY22**	**FY23**	**FY24**	**FY25**	**FY26**	**FY27**	**FY28**	**FY29**	**Total FTE's**
Electrical Designer	0.00	0.05	0.95	2.02	1.32	0.14	0.00	0.00	4.5
Electrical Engineer	0.86	1.05	2.94	4.10	5.65	1.27	0.11	0.00	16.0
Electrical Tech	0.21	0.01	0.02	3.36	4.88	1.70	0.00	0.00	10.2
Mechanical Designer	0.45	0.16	0.79	1.54	0.19	0.03	0.00	0.00	3.2
Mechanical Engineer	1.39	2.34	2.16	3.92	5.48	1.00	0.00	0.00	16.3
Mechanical Tech	0.36	0.06	0.63	5.14	13.68	5.10	1.67	0.18	26.8
Other	0.00	0.03	0.30	0.05	0.00	0.00	0.00	0.00	0.4
PhD Student	0.01	0.08	0.09	5.36	5.99	4.81	0.61	0.00	17.0
PostDoc	0.03	1.28	8.63	6.12	6.87	4.64	0.10	0.00	27.7
Scientist	2.19	2.49	1.16	4.70	7.42	3.37	0.66	0.00	22.0
Software Expert	0.36	0.85	1.01	1.61	1.45	1.45	0.30	0.00	7.0
Undergrad	0.00	0.00	0.00	3.08	2.89	3.60	0.00	0.00	9.6
Grand Totals	**5.9**	**8.4**	**18.7**	**41.0**	**55.8**	**27.1**	**3.5**	**0.2**	**160.5**

Figure 5.9: FTE resources in the ECCE project plan by resources type, by FY for both in-kind and on-project, for all costed categories.

Chapter A: ECCE Consortium Roster

The ECCE detector concept is the product of the ECCE consortium, formed in 2020 and comprising 96 institutions from around the world. The institutions bring to the consortium world-class capabilities in the science of the EIC; in the technologies needed to design, engineer, and build the ECCE detector; and in the extensive project management experience needed to realize the detector by EIC CD-4A within the cost and schedule guidance provided by the EIC project. Table A.1 lists the institutions of the ECCE consortium, along with a sampling of their hardware interests. We note here the ECCE groups also contribute to software development, including data processing tools, simulations, and analysis tools. While being the main focus of various groups, software interested are not listed in Table A.1.

Table A.1: The institutions of the ECCE consortium.

Institution	Interests
AANL /Armenia	Backward EM Cal (PbWO4)
AUGIE	SiPMs and EMCalorimeterty
BGU /Israel	EM Calorimetry (B0, low-Q2 Tagger, Luminosity monitor)
BNL	Far-forward/backward detectors; Calorimetry; AC-LGAD TOF, Si Tracker; DAQ; Installation
Brunel University /UK	Si Tracker
Canisius College	TBD
CCNU /China	Si Tracker; DAQ
Charles U. /Prague	Backward EM Cal (PbWO4)
CIAE /China	Si Tracker
CNU	DAQ & Computing
Columbia	Electronic
CUA	Backward EM Cal (PbWO4); Barrel EM Cal (SciGlass); hpDIRC;
Czech. Tech. U. /Czechia	Si Tracker
Duquesne U.	dRICH
Duke	dRICH
FIU	Backward EM Cal (PbWO4)
Georgia State	mRICH; Barrel HCal
Glasgow /Scotland	Low-Q2 Tagger; Luminosity Monitor

Table A.1 – continued from previous page

Institution	Interests
GSI /Germany	hpDIRC
GWU	uRWELL
Hampton	TBD
HEARO KEK /Japan	For-forward ZDC; Forward EM & Hadron Cal (log. seg.)
HUJI /Israel	EM Calorimetry (B0, low-Q2 Tagger, Luminosity monitor)
IJCLab-Orsay /France	Backward EM Cal (PbWO4); Far-Forward Roman Pots
IMP /China	Si Tracker
Inha U. /Korea	Forward EM Cal (log. seg.)
Iowa State	Barrel Hadron Cal; Forward EM & Hadron Cal (log. seg.); DAQ & Computing
IPAS /Taiwan	Si Tracker Assembly
JAEA /Japan	For-forward ZDC; Forward EM & Hadron Cal (log. seg.)
Jazan University /Saudi Arabia	TBD
Jeonbuk National U. /Korea	Forward EM Cal (log. seg.)
JLab	Backward EM Cal (PbWO4); dRICH; mRICH
JMU	TBD
Kobe U. /Japan	For-forward ZDC; Forward EM & Hadron Cal (log. seg.)
Korea U. /Korea	Forward EM Cal (log. seg.)
Kyungpook Natl. Univ. /Korea	Forward EM Cal (log. seg.)
LANL	Si Tracking
LBNL/Berkeley	Si Tracking
Lehigh University	Backward EM Cal (PbWO4)
LLNL	DAQ & Computing
Morehead State	Calorimetry; Computing

Table A.1 – continued from previous page

Institution	Interests
MIT	Backward EM Cal (PbWO4); Barrel EM Cal (SciGlass); uRWELL; DAQ & Computing; Si Tracking (mechanical support)
MS State U (MSU)	TBD
NCKU /Taiwan	Si Tracker; AC-LGAD
NCU /Taiwan	Si Tracker
Nihon U. /Japan	For-forward ZDC; Forward EM & Hadron Cal (log. seg.)
NMSU	TBD
NRNU MEPhI /Russia	Hadronic Calorimetry
NTHU /Taiwan	Si Tracker Assembly
NTU /Taiwan	Si Tracker Assembly
ODU	hpDIRC
Ohio U	Barrel EM Cal (SciGlass); Forward EM & Hadron Cal (log. seg.)
ORNL	Si Tracking; AC-LGAD TOF; Forward EM & Hadron Cal (log. seg.); DAQ & Computing
PNNL	DAQ & Computing
Pusan Natl. U. /Korea	Si Tracker; Forward EM Cal (log. seg.)
Rice	AC-LGAD TOF
RIKEN /Japan	For-forward ZDC; Forward EM & Hadron Cal (log. seg.)
Rutgers	Hadron Calorimetry
Saha /India	TBD
SBU/CFNF	DAQ & Computing
SCNU /China	Forward EM Cal (log. seg.)
Seoul Nat. U. /Korea	μRwell foils

Table A.1 – continued from previous page

Institution	Interests
Sejong U. /Korea	Forward EM Cal (log. seg.)
Shinshu U. /Japan	For-forward ZDC; Forward EM & Hadron Cal (log. seg.)
Sungkyunkwan U. /Korea	Forward EM Cal (log. seg.)
TAU/Israel	EM Calorimetry (B0, low-Q2 Tagger, Luminosity monitor)
Tokyo Metropolitan /Japan	For-forward ZDC; Forward EM & Hadron Cal (log. seg.)
Tsinghua U. /China	EM Calorimetry; dRICH
Tsukuba U. /Japan	For-forward ZDC; Forward EM & Hadron Cal (log. seg.);
CU Boulder	DAQ & Computing; Calorimetry
UCAD /senegal	TBD
UConn	dRICH; DAQ & Computing
UH	FF Roman Pot; B0; off-momentum trackers
UIUC	EM Cal
U. Kansas	ZDC; Far-forward/back tracking
UKY	Backward EM Cal (PbWO4)
U. Ljubljana /Slovenia	TBD
UNH	Electronics
U. Regina /Canada	Calorimetry, Tracking
U. Seoul /Korea	Forward EM Cal (log. seg.)
USTC /China	μRwell Detectors
UT Austin	TBD
U. Tsukuba /Japan	For-forward ZDC; Forward EM & Hadron Cal (log. seg.)
UTK	Collaborate with ORNL
UTSM /Chile	AC-LGAD
UVA	μRwell
Vanderbilt	μRwell

Table A.1 – continued from previous page

Institution	Interests
Virginia Tech	TBD
Virginia Union	Slow controls
Wayne State	uRWELL
WI/Israel	EM Calorimetry (B0, low-Q2 Tagger, Luminosity monitor); Muon chambers
W&M	DIRC; Low-Q2 Tagger
Yamagata U. /Japan	For-forward ZDC Forward EM & Hadron Cal (log. seg.)
Yonsei U. /Korea	Forward EM Cal (log. seg.)
York /UK	Low Q^2 Tagger; Luminosity Monitors
Zagreb U. /Croatia	TBD

Bibliography

[1] R. Abdul Khalek et al. Science Requirements and Detector Concepts for the Electron-Ion Collider: EIC Yellow Report, 2021. arXiv:2103.05419. (document), 1, 2.7, 3.2.2

[2] A. Accardi et al. Electron Ion Collider: The Next QCD Frontier: Understanding the glue that binds us all. *Eur. Phys. J. A*, 52(9):268, 2016. arXiv:1212.1701, doi:10.1140/epja/i2016-16268-9. (document), 1

[3] National Academies of Sciences, Engineering, and Medicine. *An Assessment of U.S.-Based Electron-Ion Collider Science*. The National Academies Press, Washington, DC, 2018. URL: https://www.nap.edu/catalog/25171/an-assessment-of-us-based-electron-ion-collider-science, doi:10.17226/25171. (document), 1

[4] R. Fair. EIC Technical Note EICTJ-O-DE-PLT-TD-0017-R00, 2021. URL: https://jlabdoc.jlab.org/docushare/dsweb/Get/Document-250033/21-045.pdf. 2.1, 2.2

[5] J. Anderson, K. Bauer, A. Borga, H. Boterenbrood, H. Chen, K. Chen, G. Drake, M. Dönszelmann, D. Francis, D. Guest, B. Gorini, M. Joos, F. Lanni, G. Lehmann Miotto, L. Levinson, J. Narevicius, W. Panduro Vazquez, A. Roich, S. Ryu, F. Schreuder, J. Schumacher, W. Vandelli, J. Vermeulen, D. Whiteson, W. Wu, and J. Zhang. FELIX: A PCIe based high-throughput approach for interfacing front-end and trigger electronics in the ATLAS upgrade framework. *Journal of Instrumentation*, 11(12):C12023–C12023, dec 2016. URL: https://doi.org/10.1088%2F1748-0221%2F11%2F12%2Fc12023, doi:10.1088/1748-0221/11/12/c12023. 2.1, 2.7

[6] ECCE Consortium. Notes on the use of the BaBar solenoid in ECCE, 2021. ecce-note-det-2021-01. URL: https://www.ecce-eic.org/ecce-internal-notes. 2.2

[7] ECCE Consortium. ECCE Tracking, 2021. ecce-note-det-2021-03. URL: https://www.ecce-eic.org/ecce-internal-notes. 2.3, 2.3.3, 2.3.6

[8] R. Abdul Khalek et al. Science Requirements and Detector Concepts for the Electron-Ion Collider: EIC Yellow Report, 3 2021. arXiv:2103.05419. 2.3, 2.4, 2.5.1, 2.5

[9] G. Aglieri Rinella et al. First demonstration of in-beam performance of bent Monolithic Active Pixel Sensors, 5 2021. arXiv:2105.13000. 2.3.1

[10] Domenico Colella. ALICE ITS 3: the first truly cylindrical inner tracker, 2021. arXiv:2111.09689. 2.3.1

[11] X. Li, M. Brooks, M. Durham, Y. Corrales Morales, A. Morreale, C. Prokop, E. Renner, and W. Sondheim. Forward silicon vertex/tracking detector design and R&D for the future Electron-Ion Collider. In *Particles and Nuclei International Conference* , 11 2021. arXiv:2111.03182. 2.3.1

[12] J. Blank and K. Deb. pymoo: Multi-objective optimization in python. *IEEE Access*, 8:89497–89509, 2020. 2.3.3

[13] H. Ishibuchi, R. Imada, Y. Setoguchi, and Y. Nojima. Performance comparison of NSGA-II and NSGA-III on various many-objective test problems. In *2016 IEEE Congress on Evolutionary Computation (CEC)*, pages 3045–3052. IEEE, 2016. 2.3.3

[14] M. Rocklin. Dask: Parallel computation with blocked algorithms and task scheduling. In *Proceedings of the 14th python in science conference*, volume 130, page 136. Citeseer, 2015. 2.3.3

[15] ECCE Consortium. AI-assisted design of the ECCE detector: the ECCE Tracker Example, 2021. ecce-note-comp-2021-03. URL: https://www.ecce-eic.org/ecce-internal-notes. 2.3.3, 2.3.6, 2.8

[16] ECCE Consortium. Selected topics in ECCE software and simulation, 2021. ecce-note-comp-2021-02. URL: https://www.ecce-eic.org/ecce-internal-notes. 2.3.4, 2.8, 3.1

[17] Ferdinand Willeke. Electron Ion Collider Conceptual Design Report 2021, 2 2021. URL: https://www.osti.gov/biblio/1765663, doi:10.2172/1765663. 2.3.4

[18] ECCE Consortium. ECCE Particle Identification, 2021. ecce-note-det-2021-04. URL: https://www.ecce-eic.org/ecce-internal-notes. 2.4

[19] U. Buchner, J. P. Donker, B. Spaan, J. Spengler, G. Schweda, D. Wegener, and W. Schmidt-Parzefall. PERFORMANCE OF A SCINTILLATING GLASS CALORIMETER FOR ELECTROMAGNETIC SHOWERS. *Nucl. Instrum. Meth. A*, 272:695, 1988. doi:10.1016/0168-9002(88)90750-4. 2.5, 2.5.2

[20] P. Ioannou et al. The Experiment 705 electromagnetic shower calorimeter. *Nucl. Instrum. Meth. A*, 332:57–77, 1993. doi:10.1016/0168-9002(93)90741-Y. 2.5, 2.5.2

[21] C. A. Aidala, V. Bailey, S. Beckman, R. Belmont, C. Biggs, J. Blackburn, S. Boose, M. Chiu, M. Connors, E. Desmond, A. Franz, J. S. Haggerty, X. He, M. M. Higdon, J. Huang, K. Kauder, E. Kistenev, J. LaBounty, J. G. Lajoie, M. Lenz, W. Lenz, S. Li, V. R.Loggins, E. J. Mannel, T. Majoros, M. P. McCumber, J. L. Nagle, M. Phipps, C. Pinkenburg, S. Polizzo, C. Pontieri, M. L. Purschke, J. Putschke, M. Sarsour, T. Rinn, R. Ruggiero, A. Sen, A. M. Sickles, M. J. Skoby, J. Smiga, P. Sobel, P. W. Stankus, S. Stoll, A. Sukhanov, E. Thorsland, F. Toldo, R. S. Towell, B. Ujvari, S. Vazquez-Carson, and C. L. Woody. Design and beam test results for the sPHENIX electromagnetic and hadronic calorimeter prototypes. *IEEE Transactions on Nuclear Science*, 65(12):2901–2919, December 2018. URL: https://doi.org/10.1109/tns.2018.2879047, doi:10.1109/tns.2018.2879047. 2.5

[22] ECCE Consortium. ECCE Calorimetry, 2021. ecce-note-det-2021-02. URL: https://www.ecce-eic.org/ecce-internal-notes. 2.5

[23] T. Horn et al. Scintillating crystals for the Neutral Particle Spectrometer in Hall C at JLab. *Nucl. Instrum. Meth. A*, 956:163375, 2020. arXiv:1911.11577, doi:10.1016/j.nima.2019.163375. 2.5.1

[24] T. Horn. A $PbWO_4$-based Neutral Particle Spectrometer in Hall C at 12 GeV JLab. *J. Phys. Conf. Ser.*, 587(1):012048, 2015. doi:10.1088/1742-6596/587/1/012048. 2.5.1

[25] Expression of Interest for the Electron Endcap Electromagnetic Calorimeter, 2020. https://indico.bnl.gov/event/8552/contributions/43186/attachments/31241/49300/EIC.EoI-EEEmCal-10312020.docx. 2.5.1

[26] J. Bettane et al. EEEMCal mechanical design and integration, 2020. https://wiki.jlab.org/cuawiki/index.php/EEEMCDocuments. 2.5.1

[27] T. Horn et al. eRD1: EIC Detector R& D Progress Reports 2017-2021, 2021. 2.5.2

[28] W. Erni et al. Technical Design Report for PANDA Electromagnetic Calorimeter (EMC), 10 2008. arXiv:0810.1216. 2.5.2

[29] Fedor Guber and Ilya Selyuzhenkov, editors. *Technical Design Report for the CBM Projectile Spectator Detector (PSD)*. GSI, Darmstadt, 2015. URL: https://repository.gsi.de/record/109059. 2.5.4

[30] ECCE Consortium. ECCE Electronics and Readout/DAQ, 2021. ecce-note-det-2021-05. URL: https://www.ecce-eic.org/ecce-internal-notes. 2.6, 2.7

[31] J. Shiers. The Worldwide LHC Computing Grid (worldwide LCG). *Computer Physics Communications*, 177(1):219–223, 2007. Proceedings of the Conference on Computational Physics 2006. URL: https://www.sciencedirect.com/science/article/pii/S001046550700077X, doi:https://doi.org/10.1016/j.cpc.2007.02.021. 2.8

[32] ECCE Consortium. ECCE Computing Plan, 2021. ecce-note-comp-2021-01. URL: https://www.ecce-eic.org/ecce-internal-notes. 2.8, 2.27, 2.8

[33] E Cisbani, A Del Dotto, C Fanelli, Williams, et al. AI-optimized detector design for the future Electron-Ion Collider: the dual-radiator RICH case. *Journal of Instrumentation*, 15(05):P05009, 2020. doi:https://doi.org/10.1088/1748-0221/15/05/P05009. 2.8

[34] C. Fanelli and J. Pomponi. DeepRICH: learning deeply Cherenkov detectors. *Machine Learning: Science and Technology*, 1(1):015010, Apr 2020. URL: http://dx.doi.org/10.1088/2632-2153/ab845a, doi:10.1088/2632-2153/ab845a. 2.8

[35] F. Ameli, M. Battaglieri, M. Bondí, A. Celentano, S. Boyarinov, N. Brei, T. Chiarusi, R. De Vita, C. Fanelli, V.-d. Gyurjyan, et al. Streaming Readout of the CLAS12 Forward Tagger Using TriDAS and JANA2. *arXiv preprint arXiv:2104.11388*, 2021. 2.8

[36] Intelligent experiments through real-time ai: Fast data processing and autonomous detector control for sphenix and future eic detectors, 2021. DOE-FOA-0002490. 2.8

[37] Y. Huang, Y. Ren, S. Yoo, and J. Huang. Efficient data compression for 3d sparse tpc via bicephalous convolutional autoencoder. In *IEEE 2021 International Conference on Machine Learning and Applications*, IEEE ICMLA", 2021. arXiv:2111.05423. 2.8

[38] S. Miryala et al. Waveform processing using neural network algorithms on the front-end electronics. In *22nd International Workshop on Radiation Imaging Detectors*, 2021. 2.8

[39] The sPHENIX collaboration. sPHENIX software repository. https://github.com/sPHENIX-Collaboration, 2015. 2.8

[40] X. Ai et al. A Common Tracking Software Project, June 2021. arXiv:2106.13593. 2.8

[41] J. D. Osborn, A. D. Frawley, J. Huang, S. Lee, H. Pereira Da Costa, M. Peters, C. Pinkenburg, C. Roland, and H. Yu. Implementation of ACTS into sPHENIX Track Reconstruction. *Comput. Softw. Big Sci.*, 5(1):23, 2021. arXiv:2103.06703, doi:10.1007/s41781-021-00068-w. 2.8

[42] ECCE Consortium. ECCE Cost and Schedule, 2021. ecce-note-det-2021-07. URL: https://www.ecce-eic.org/ecce-internal-notes. 2.10, 5.1, 5.1, 5.3, 5.4, 5.5

[43] ECCE Consortium. ECCE resolution studies of DIS and semi-inclusive DIS kinematic variables, 2021. ecce-note-phys-2021-05. URL: https://www.ecce-eic.org/ecce-internal-notes. 3.1.1, 3.2.1

[44] ECCE Consortium. Inclusive reactions with ECCE, 2021. ecce-note-phys-2021-09. URL: https://www.ecce-eic.org/ecce-internal-notes. 3.1.2, 3.3.2

[45] E. C. Aschenauer, S. Fazio, J. H. Lee, H. Mantysaari, B. S. Page, B. Schenke, T. Ullrich, R. Venugopalan, and P. Zurita. The electron–ion collider: assessing the energy dependence of key measurements. *Rept. Prog. Phys.*, 82(2):024301, 2019. arXiv:1708.01527, doi:10.1088/1361-6633/aaf216. 3.1.2

[46] I. Friscic et al. Neutron spin structure from e-3He scattering with double spectator tagging at the electron-ion collider. *Phys. Lett. B*, 823:136726, 2021. arXiv:2106.08805, doi:10.1016/j.physletb.2021.136726. 3.1.2

[47] X.-D. Ji. Gauge-Invariant Decomposition of Nucleon Spin. *Phys. Rev. Lett.*, 78:610–613, 1997. arXiv:hep-ph/9603249, doi:10.1103/PhysRevLett.78.610. 3.1.4

[48] D. W. Sivers. Single Spin Production Asymmetries from the Hard Scattering of Point-Like Constituents. *Phys. Rev. D*, 41:83, 1990. doi:10.1103/PhysRevD.41.83. 3.1.5

[49] J. C. Collins. Fragmentation of transversely polarized quarks probed in transverse momentum distributions. *Nucl. Phys. B*, 396:161–182, 1993. arXiv:hep-ph/9208213, doi:10.1016/0550-3213(93)90262-N. 3.1.5

[50] J. Cammarota, L. Gamberg, Z.-B. Kang, J. A. Miller, D. Pitonyak, A. Prokudin, T. C. Rogers, and N. Sato. Origin of single transverse-spin asymmetries in high-energy collisions. *Phys. Rev. D*, 102(5):054002, 2020. arXiv:2002.08384, doi:10.1103/PhysRevD.102.054002. 3.5

[51] R. Gupta, Y.-C. Jang, B. Yoon, H.-W. Lin, V. Cirigliano, and T. Bhattacharya. Isovector Charges of the Nucleon from 2+1+1-flavor Lattice QCD. *Phys. Rev. D*, 98:034503, 2018. arXiv:1806.09006, doi:10.1103/PhysRevD.98.034503. 3.5

[52] C. Alexandrou, S. Bacchio, M. Constantinou, J. Finkenrath, K. Hadjiyiannakou, K. Jansen, G. Koutsou, and A. Vaquero Aviles-Casco. Nucleon axial, tensor, and scalar charges and σ-terms in lattice QCD. *Phys. Rev. D*, 102(5):054517, 2020. arXiv:1909.00485, doi:10.1103/PhysRevD.102.054517. 3.5

[53] ECCE Consortium. ECCE sensitivity studies for single hadron transverse single spin asymmetry measurements from the proton, 2021. ecce-note-phys-2021-06. URL: https://www.ecce-eic.org/ecce-internal-notes. 3.1.5

[54] ECCE Consortium. Jet Reconstruction in the Breit Frame using the Centauro Algorithm with the ECCE Detector, 2021. ecce-note-phys-2021-10. URL: https://www.ecce-eic.org/ecce-internal-notes. 3.2.2, 3.6

[55] ECCE Consortium. ECCE Open Heavy Flavor Nuclear Modification Factor, 2021. ecce-note-phys-2021-04. URL: https://www.ecce-eic.org/ecce-internal-notes. 3.2.2, 3.13

[56] ECCE Consortium. ECCE Exclusive Reactions, 2021. ecce-note-phys-2021-03. URL: https://www.ecce-eic.org/ecce-internal-notes. 3.2.3, 3.3.3

[57] L. V. Gribov, E. M. Levin, and M. G. Ryskin. Semihard Processes in QCD. *Phys. Rept.*, 100:1–150, 1983. doi:10.1016/0370-1573(83)90022-4. 3.3

[58] J. Jalilian-Marian, A. Kovner, L. D. McLerran, and H. Weigert. The Intrinsic glue distribution at very small x. *Phys. Rev. D*, 55:5414–5428, 1997. arXiv:hep-ph/9606337, doi:10.1103/PhysRevD.55.5414. 3.3

[59] J. Jalilian-Marian, A. Kovner, and H. Weigert. The Wilson renormalization group for low x physics: Gluon evolution at finite parton density. *Phys. Rev. D*, 59:014015, 1998. arXiv:hep-ph/9709432, doi:10.1103/PhysRevD.59.014015. 3.3

[60] J. Jalilian-Marian, A. Kovner, A. Leonidov, and H. Weigert. The Wilson renormalization group for low x physics: Towards the high density regime. *Phys. Rev. D*, 59:014014, 1998. arXiv:hep-ph/9706377, doi:10.1103/PhysRevD.59.014014. 3.3

[61] J. Jalilian-Marian, A. Kovner, A. Leonidov, and H. Weigert. The BFKL equation from the Wilson renormalization group. *Nucl. Phys. B*, 504:415–431, 1997. arXiv:hep-ph/9701284, doi:10.1016/S0550-3213(97)00440-9. 3.3

[62] E. Iancu, A. Leonidov, and L. D. McLerran. Nonlinear gluon evolution in the color glass condensate. 1. *Nucl. Phys. A*, 692:583–645, 2001. arXiv:hep-ph/0011241, doi:10.1016/S0375-9474(01)00642-X. 3.3

[63] E. Iancu, A. Leonidov, and L. D. McLerran. The Renormalization group equation for the color glass condensate. *Phys. Lett. B*, 510:133–144, 2001. arXiv:hep-ph/0102009, doi:10.1016/S0370-2693(01)00524-X. 3.3

[64] I. Balitsky. Operator expansion for high-energy scattering. *Nucl. Phys. B*, 463:99–160, 1996. arXiv:hep-ph/9509348, doi:10.1016/0550-3213(95)00638-9. 3.3

[65] I. Balitsky. Factorization and high-energy effective action. *Phys. Rev. D*, 60:014020, 1999. arXiv:hep-ph/9812311, doi:10.1103/PhysRevD.60.014020. 3.3

[66] Y. V. Kovchegov. Unitarization of the BFKL pomeron on a nucleus. *Phys. Rev. D*, 61:074018, 2000. arXiv:hep-ph/9905214, doi:10.1103/PhysRevD.61.074018. 3.3

[67] Y. V. Kovchegov. Small x F(2) structure function of a nucleus including multiple pomeron exchanges. *Phys. Rev. D*, 60:034008, 1999. arXiv:hep-ph/9901281, doi:10.1103/PhysRevD.60.034008. 3.3

[68] L. D. McLerran and R. Venugopalan. Gluon distribution functions for very large nuclei at small transverse momentum. *Phys. Rev. D*, 49:3352–3355, 1994. arXiv:hep-ph/9311205, doi:10.1103/PhysRevD.49.3352. 3.3

[69] L. D. McLerran and R. Venugopalan. Computing quark and gluon distribution functions for very large nuclei. *Phys. Rev. D*, 49:2233–2241, 1994. arXiv:hep-ph/9309289, doi:10.1103/PhysRevD.49.2233. 3.3

[70] L. D. McLerran and R. Venugopalan. Green's functions in the color field of a large nucleus. *Phys. Rev. D*, 50:2225–2233, 1994. arXiv:hep-ph/9402335, doi:10.1103/PhysRevD.50.2225. 3.3

[71] S. Munier, A. M. Stasto, and Alfred H. Mueller. Impact parameter dependent S matrix for dipole proton scattering from diffractive meson electroproduction. *Nucl. Phys. B*, 603:427–445, 2001. arXiv:hep-ph/0102291, doi:10.1016/S0550-3213(01)00168-7. 3.3.3

[72] H. Kowalski, L. Motyka, and G. Watt. Exclusive diffractive processes at HERA within the dipole picture. *Phys. Rev. D*, 74:074016, 2006. arXiv:hep-ph/0606272, doi:10.1103/PhysRevD.74.074016. 3.3.3

[73] H. Mäntysaari and B. Schenke. Evidence of strong proton shape fluctuations from incoherent diffraction. *Phys. Rev. Lett.*, 117(5):052301, 2016. arXiv:1603.04349, doi:10.1103/PhysRevLett.117.052301. 3.3.3

[74] T. Lappi and H. Mantysaari. Incoherent diffractive J/Psi-production in high energy nuclear DIS. *Phys. Rev. C*, 83:065202, 2011. arXiv:1011.1988, doi:10.1103/PhysRevC.83.065202. 3.3.3

[75] ECCE Consortium. ECCE Diffractive and Tagging Processes, 2021. ecce-note-phys-2021-02. URL: https://www.ecce-eic.org/ecce-internal-notes. 3.11, 3.4.3, 3.5.3, 3.6

[76] ECCE Consortium. ECCE Dihadron Azimuthal Correlations, 2021. ecce-note-phys-2021-13. URL: https://www.ecce-eic.org/ecce-internal-notes. 3.12, 3.3.4

[77] L. Zheng, E. C. Aschenauer, J. H. Lee, and B.-W. Xiao. Probing Gluon Saturation through Dihadron Correlations at an Electron-Ion Collider. *Phys. Rev. D*, 89(7):074037, 2014. arXiv:1403.2413, doi:10.1103/PhysRevD.89.074037. 3.3.4

[78] X. Li et al. A New Heavy Flavor Program for the Future Electron-Ion Collider. *EPJ Web Conf.*, 235:04002, 2020. arXiv:2002.05880, doi:10.1051/epjconf/202023504002. 3.3.5

[79] ECCE Consortium. Modification of the jet yield due to nuclear matter effects with ECCE, 2021. ecce-note-phys-2021-08. URL: https://www.ecce-eic.org/ecce-internal-notes. 3.3.5

[80] X.-D. Ji. A QCD analysis of the mass structure of the nucleon. *Phys. Rev. Lett.*, 74:1071–1074, 1995. arXiv:hep-ph/9410274, doi:10.1103/PhysRevLett.74.1071. 3.4

[81] C. Lorcé. On the hadron mass decomposition. *Eur. Phys. J. C*, 78(2):120, 2018. arXiv:1706.05853, doi:10.1140/epjc/s10052-018-5561-2. 3.4

[82] A. Metz, B. Pasquini, and S. Rodini. Revisiting the proton mass decomposition. *Phys. Rev. D*, 102:114042, 2020. arXiv:2006.11171, doi:10.1103/PhysRevD.102.114042. 3.4

[83] C. Lorcé, A. Metz, B. Pasquini, and S. Rodini. Energy-momentum tensor in QCD: nucleon mass decomposition and mechanical equilibrium. *JHEP*, 11:121, 2021. arXiv:2109.11785, doi:10.1007/JHEP11(2021)121. 3.4

[84] J. Arrington et al. Revealing the structure of light pseudoscalar mesons at the electron–ion collider. *J. Phys. G*, 48(7):075106, 2021. arXiv:2102.11788, doi:10.1088/1361-6471/abf5c3. 3.4.1, 3.4.3

[85] A. C. Aguilar et al. Pion and Kaon Structure at the Electron-Ion Collider. *Eur. Phys. J. A*, 55(10):190, 2019. arXiv:1907.08218, doi:10.1140/epja/i2019-12885-0. 3.4.1, 3.4.3

[86] ECCE Consortium. Exclusive J/ψ detection and physics with ECCE, 2021. ecce-note-phys-2021-15. URL: https://www.ecce-eic.org/ecce-internal-notes. 3.14

[87] C. D. Roberts, D. G. Richards, T. Horn, and L. Chang. Insights into the emergence of mass from studies of pion and kaon structure. *Prog. Part. Nucl. Phys.*, 120:103883, 2021. arXiv:2102.01765, doi:10.1016/j.ppnp.2021.103883. 3.4.3

[88] T. Horn and C. D. Roberts. The pion: an enigma within the Standard Model. *J. Phys. G*, 43(7):073001, 2016. arXiv:1602.04016, doi:10.1088/0954-3899/43/7/073001. 3.4.3

[89] ECCE Consortium. Electroweak and BSM Physics with ECCE, 2021. ecce-note-phys-2021-14. URL: https://www.ecce-eic.org/ecce-internal-notes. 3.5.1

[90] M. Gonderinger and M. J. Ramsey-Musolf. Electron-to-Tau Lepton Flavor Violation at the Electron-Ion Collider. *JHEP*, 11:045, 2010. [Erratum: JHEP 05, 047 (2012)]. arXiv:1006.5063, doi:10.1007/JHEP11(2010)045. 3.5.1, 3.16

[91] Vincenzo Cirigliano, Kaori Fuyuto, Christopher Lee, Emanuele Mereghetti, and Bin Yan. Charged Lepton Flavor Violation at the EIC. *JHEP*, 03:256, 2021. arXiv:2102.06176, doi:10.1007/JHEP03(2021)256. 3.5.1

[92] W. Buchmuller, R. Ruckl, and D. Wyler. Leptoquarks in Lepton - Quark Collisions. *Phys. Lett. B*, 191:442–448, 1987. [Erratum: Phys.Lett.B 448, 320–320 (1999)]. doi:10.1016/0370-2693(87)90637-X. 3.5.1

[93] S. Chekanov et al. Search for lepton flavor violation in e^+p collisions at HERA. *Phys. Rev. D*, 65:092004, 2002. arXiv:hep-ex/0201003, doi:10.1103/PhysRevD.65.092004. 3.16

[94] S. Chekanov et al. Search for lepton-flavor violation at HERA. *Eur. Phys. J. C*, 44:463–479, 2005. arXiv:hep-ex/0501070, doi:10.1140/epjc/s2005-02399-1. 3.16

[95] C. Adloff et al. A Search for leptoquark bosons and lepton flavor violation in e^+p collisions at HERA. *Eur. Phys. J. C*, 11:447–471, 1999. [Erratum: Eur.Phys.J.C 14, 553–554 (2000)]. arXiv:hep-ex/9907002, doi:10.1007/s100520050646. 3.16

[96] A. Aktas et al. Search for lepton flavour violation in ep collisions at HERA. *Eur. Phys. J. C*, 52:833–847, 2007. arXiv:hep-ex/0703004, doi:10.1140/epjc/s10052-007-0440-2. 3.16

[97] D. Becker et al. The P2 experiment. *Eur. Phys. J. A*, 54(11):208, 2018. arXiv:1802.04759, doi:10.1140/epja/i2018-12611-6. 3.17

[98] The MOLLER Project, Measurement Of a Lepton Lepton Electroweak Reaction An Ultra-precise Measurement of the Weak Mixing Angle using Møller Scattering, Conceptual Design Report, 2020. 3.17

[99] P. Souder et al. Precision Measurement of Parity-violation in Deep Inelastic Scattering Over a Broad Kinematic Range, 2010. URL: https://hallaweb.jlab.org/collab/PAC/PAC34/PR-09-012-pvdis.pdf. 3.17

[100] J. Erler, C. J. Horowitz, S. Mantry, and P. A. Souder. Weak Polarized Electron Scattering. *Ann. Rev. Nucl. Part. Sci.*, 64:269–298, 2014. arXiv:1401.6199, doi:10.1146/annurev-nucl-102313-025520. 3.17

[101] J. Erler and M. J. Ramsey-Musolf. The Weak mixing angle at low energies. *Phys. Rev. D*, 72:073003, 2005. arXiv:hep-ph/0409169, doi:10.1103/PhysRevD.72.073003. 3.17

[102] R. Boughezal, F. Petriello, and D. Wiegand. Removing flat directions in standard model EFT fits: How polarized electron-ion collider data can complement the LHC. *Phys. Rev. D*, 101(11):116002, 2020. arXiv:2004.00748, doi:10.1103/PhysRevD.101.116002. 3.17, 3.5.1

[103] W. Buchmuller and D. Wyler. Effective Lagrangian Analysis of New Interactions and Flavor Conservation. *Nucl. Phys. B*, 268:621–653, 1986. doi:10.1016/0550-3213(86)90262-2. 3.5.1

[104] B. Grzadkowski, M. Iskrzynski, M. Misiak, and J. Rosiek. Dimension-Six Terms in the Standard Model Lagrangian. *JHEP*, 10:085, 2010. arXiv:1008.4884, doi:10.1007/JHEP10(2010)085. 3.5.1

[105] G. Passarino and M. Trott. The Standard Model Effective Field Theory and Next to Leading Order, 10 2016. arXiv:1610.08356. 3.5.1

[106] A. Courtoy, S. Baeßler, M. González-Alonso, and S. Liuti. Beyond-Standard-Model Tensor Interaction and Hadron Phenomenology. *Phys. Rev. Lett.*, 115:162001, 2015. arXiv:1503.06814, doi:10.1103/PhysRevLett.115.162001. 3.5.1

[107] M. Albaladejo, A. N. Hiller Blin, A. Pilloni, D. Winney, C. Fernández-Ramírez, V. Mathieu, and A. Szczepaniak. XYZ spectroscopy at electron-hadron facilities: Exclusive processes. *Phys. Rev. D*, 102:114010, 2020. arXiv:2008.01001, doi:10.1103/PhysRevD.102.114010. 3.5.2

[108] ECCE Consortium. ECCE Spectroscopy, 2021. ecce-note-phys-2021-12. URL: https://www.ecce-eic.org/ecce-internal-notes. 3.5.2

[109] ECCE Consortium. Evaluation of longitudinal double-spin asymmetry measurements in semi-inclusive deep-inelastic scattering from the proton for the ECCE design, 2021. ecce-note-phys-2021-11. URL: https://www.ecce-eic.org/ecce-internal-notes. 3.6

[110] ECCE Consortium. ECCE Jet Resolution, 2021. ecce-note-phys-2021-01. URL: https://www.ecce-eic.org/ecce-internal-notes. 3.6

[111] H. T. Li, Z. L. Liu, and I. Vitev. Heavy meson tomography of cold nuclear matter at the electron-ion collider. *Phys. Lett. B*, 816:136261, 2021. arXiv:2007.10994, doi:10.1016/j.physletb.2021.136261. 3.21

[112] M.A. Green and B.P. Strauss. The cost of superconducting magnets as a function of stored energy and design magnetic induction times the field volume. *IEEE Transactions on Applied Superconductivity*, 18(2):248–251, June 2008. URL: https://doi.org/10.1109/tasc.2008.921279, doi:10.1109/tasc.2008.921279. 5.1

[113] P. Rossi and T. Ullrich. Assessment of R&D need for an EIC detector, 2021. URL: https://indico.bnl.gov/event/10974/contributions/53172/attachments/36485/59965/Detector_RD_Plan_Aug10.2021.pdf. 5.1, 5.2